

Submillimeter Star Formation Rates in Interacting Pairs

by

Aaron James Ronald Klopp
B.Sc. Queen's University, 2001


A Thesis Submitted in Partial Fulfillment of the
Requirements for the Degree of

M.Sc.


in the Department of Physics and Astronomy
University of Victoria

We accept this thesis as conforming
to the required standard.


Dr. C. J. Pritchett, Supervisor (Department of Physics & Astronomy)


Dr. F. D. A. Hartwick, Departmental Member (Department of Physics & Astronomy)


Dr. R. Illner, Outside Member (Department of Mathematics and Statistics)


Dr. D. Schade, External Examiner (Herzberg Institute of Astrophysics)

© Aaron Klopp, 2003
University of Victoria.

*All rights reserved. This thesis may not be reproduced in whole or in part,
by photocopying or other means, without the permission of the author.*

Supervisor: Dr. C J. Pritchett

Abstract

We have completed a program of observing interacting pairs and field galaxies selected from the CNOC2 survey. Observations were made with the Submillimeter Common User Bolometer Array (SCUBA) at the James Clerk Maxwell Telescope (JCMT). The goal was to use SCUBA fluxes (850/450 μm) to determine star formation rates (SFR's) for 20 interacting pairs (mean redshift of 0.36), and 7 field galaxies chosen on the basis of their large optically-inferred star formation rate. After reducing the data the 850 μm fluxes were used to calculate star formation rates for 18 of those pairs that constituted the best data of the sample. These SFR's were also used to measure the star formation rate per unit blue luminosity of the ensemble of pairs. The data from the 450 μm receivers was insufficiently stable to give reliable fluxes.


Two objects were detected at 850 μm above the critical 3σ threshold. Another three were detected above 2.5σ . The significance of these detections is evident from χ^2_ν and Monte Carlo tests, as well as by examining the optical/UV SFR's of CNOC2 galaxies. By inferring a 850 μm flux from an optical/UV SFR we have determined that the chance of obtaining 5 detections ($> 2.5\sigma$) is exceedingly small unless the dust absorbs an average of $\sim 97\%$ of the bolometric UV energy in a typical CNOC2 galaxy. Given what we know of dust emission at low and moderate redshifts we believe this scenario to be very unlikely, suggesting our pairs constitute a unique ensemble of star formers in their environment.


The ensemble average star formation rate per pair was found to be $5.5 \pm 2.4 h \text{ M}_\odot \text{ yr}^{-1}$, an average determined by weighting individual SFR's according to flux error. This value of SFR was used to calculate the SFR per unit blue luminosity (SFR/ L_B), which was found to range between $(4 - 10) \times 10^{-10} \text{ M}_\odot \text{ yr}^{-1} L_{B,\odot}$ depending on the subset of the sample used. Using values from the literature we

determined the $\langle \text{SFR}/L_B \rangle$ for field galaxies at moderate redshift. We found that our pairs produced an excess of SFR/L_B over a comparable sample of field galaxies at the same redshift. The most conservative estimate of this excess is $\sim 2\times$, but a more consistent value is likely $6 - 9\times$. These results provide tantalizing evidence for enhanced star formation in interacting pairs at moderate redshift.

Examiners:


Dr. C. J. Pritchett, Supervisor (Department of Physics & Astronomy)


Dr. F. D. A. Hartwick, Departmental Member (Department of Physics & Astronomy)


Dr. R. Illner, Outside Member (Department of Mathematics and Statistics)

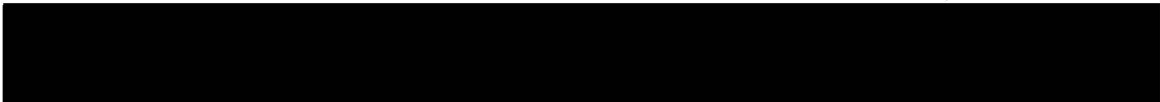

Dr. D. Schade, External Examiner (Herzberg Institute of Astrophysics)

Table of Contents

Abstract	ii
Table of Contents	iv
List of Figures	vii
List of Tables	viii
Acknowledgments	ix
Glossary of Acronyms	xi
1 Introduction	1
1.1 Preamble	1
1.2 Submillimeter Astronomy	2
1.2.1 Instruments and Observing parameters	2
1.3 The Physics of Dust	11
1.3.1 Dust Absorption	11
1.3.2 Dust Emission	14
1.3.3 Power Sources for Dust Emission	16
1.3.4 Submillimeter Emission	17
1.4 Star Formation Rate Indicators	17
1.4.1 Modeling Star Formation	17
1.4.2 Ultraviolet Continuum Indicators	19
1.4.3 Emission Line Indicators: [O II] and H α	20
1.4.4 FIR Continuum Indicators	20
1.4.5 Radio Luminosity	22
1.4.6 Comparing Star Formation Indicators	23
1.4.7 Total Star Formation Rate	24
1.5 Mergers and Induced Star Formation	25
1.5.1 Mergers and Interactions	25

1.5.2	Ultra-Luminous Infrared Galaxies (ULIRG's)	31
1.5.3	Star Formation in Interacting Pairs	32
1.6	The Star Formation History of the Universe	32
1.7	The Astronomical Samples	34
1.7.1	The surveys: SSRS2, CNOC1, CNOC2 and SLUGS	35
1.7.2	Properties of the Sample	36
1.8	The Program of Research	41
2	Observations and Data Reduction	44
2.1	The Detector	44
2.1.1	Instrument Design and Parameters	44
2.1.2	Telescope Detector and Design	45
2.1.3	Observing Modes	45
2.1.4	Observing in Photometry Mode	46
2.1.5	Observing at the JCMT	47
2.1.6	Selection of Targets	49
2.2	Data Reduction	53
2.2.1	The Reduction Scheme	53
2.3	Observations of Pairs	63
2.4	Reduction and Observations of Serendipitous Sources	66
2.4.1	Finding CNOC2 Galaxies	66
2.4.2	Bolometer Positions	68
2.4.3	“Capturing” Serendipitous Sources	69
2.4.4	Eliminating Bad Bolometers	70
2.4.5	Noise Analysis	70
2.4.6	Observations of Serendipitous Sources	70
3	Results and Analysis	80
3.1	Analysis of the Data	80
3.1.1	The Original Targets	80
3.1.2	The Serendipitous Sources	82
3.1.3	Expected Flux	85
3.2	Construction of Star Formation Rates	87
3.2.1	The Grey Body Spectrum	87
3.2.2	Determination of Dust Temperature and β	88
3.2.3	Physical Principles	90
3.2.4	Star Formation Rates for Pairs	92
3.2.5	Optical Properties of Detected Galaxies	98
3.2.6	Star Formation Rate Density—Preliminaries	100
3.2.7	Star Formation Rate Density—Details	103
3.2.8	Star Formation Rate Density—A Useful Comparison	105

4	Discussion	109
4.1	Lensing Effects on SCUBA surveys	109
4.2	Detections	111
4.2.1	Confirmation of Detections	111
4.2.2	Other Sources of Error	113
4.3	Significance of Detections	114
4.3.1	Inferring sub-mm flux from SFR's	114
4.3.2	Monte Carlo Tests	124
4.4	Dust Obscuration	124
4.5	Significance of the Star Formation Rate	129
5	Conclusions	132
5.1	Summary	132
5.2	Future Work	136
A	Parametrization of Dust Extinction in Optical, UV and Infrared	146
A.1	The Infrared	146
A.2	Optical/NIR	147
A.3	UV and Far UV	147

List of Figures

1.1	Transmission windows in the sub-mm	4
1.2	SCUBA array diagram, showing deadspace	5
1.3	SED for a dusty galaxy with CO lines	8
1.4	Predicted flux density with redshift: The negative k-correction	9
1.5	Dust absorption from the UV to optical	13
1.6	Dust absorption in the UV for varying absorption	26
1.7	Total SFR measured at different UV wavelength	27
1.8	FIR, UV and total SFR, as a function of τ_V	28
1.9	Pictures of interacting pairs	42
2.1	Comparison of dissimilar reduction techniques.	56
2.2	Comparison of two similar reduction techniques.	57
2.3	Analysis of noise as a function of time for pairs in the 850 μm band	61
2.4	Analysis of noise as a function of time for pairs in the 450 μm band	62
2.5	Field Rotation of Bolometers	67
2.6	Bolometer noise distribution.	71
2.7	Noise analysis for serendipitous sources.	72
2.8	Distribution of the number of integrations for serendipitous sources	74
3.1	Flux distribution for serendipitous sources	83
3.2	Flux distribution for sky-pointing bolometers	84
3.3	Comparison of Opt/UV and Sub-mm SFR's for field galaxies	96
3.4	Comparison of Opt/UV and Sub-mm SFR's for interacting pairs	97
4.1	Inferred S/N for 5404 CNOC2 galaxies	117
4.2	Inferred S/N for serendipitous galaxies	118
4.3	η as a function of absorption	120
4.4	The number detections plotted with η	121
4.5	Comparison of two inferred-flux distributions.	123
4.6	Illustration of two-regime model for dusty galaxies	128

List of Tables

1.1	Atmospheric Transmission Windows in the sub-mm	3
1.2	CNO2 properties of our 27 targets	39
1.2	CNO2 properties of our 27 targets	40
2.1	Observing conditions for 19 pairs	51
2.2	Observing conditions for 1 pair and 7 field galaxies selected with high SFR	52
2.3	Order of data reduction operations for the seven reduction attempts.	58
2.4	Flux data for 19 pairs	64
2.5	Flux data for 1 pair and field galaxies	65
2.6	Data for 108 serendipitous sources	75
2.6	Data for 108 serendipitous sources	76
2.6	Data for 108 serendipitous sources	77
2.6	Data for 108 serendipitous sources	78
2.6	Data for 108 serendipitous sources	79
3.1	Probabilities of detections	82
3.2	Expected sub-mm flux from a galaxy with a given SFR.	86
3.3	Star formation rates for all 20 pairs and 7 field galaxies using various cosmological models.	93
3.4	Fluxes and S/N of detected sources	94
3.5	Star formation of Arp 220 calculated with flux from various IR wavebands	95
3.6	Optical and physical properties of detections	99
3.7	Restframe <i>B</i> band luminosity density in the moderate <i>z</i> Universe . .	101
3.8	Star formation per unit luminosity	107
3.9	Star formation per unit luminosity for pairs with lower optical/UV SFR	107

Acknowledgements

There are many people I would like to thank for their support and collaboration. First, this research has been made possible, in part, by a fellowship from the University of Victoria, and through the NRC, which funded my observing run in Hawaii. This research would not have been possible, let alone successful, had it not been for the support of my adviser, Dr. Chris Pritchett. Even during the times when neither of us understood what was going on I could always count on his insightful intuition about astronomical research to make sense of my results. Further, his sense of humour and good nature helped make the most difficult times bearable and even interesting. He has been both cooperative and understanding in more ways than I can mention. I don't think I can thank him enough.

I would like to thank Dr. Dave Patton, of Trent University, without whose advice and data I wouldn't have appreciated the intricacies of pair statistics. Along with Dave, I would like to thank Dr. Simon Morris of Durham University for letting me use his optical star formation rates for our target galaxies. Simon was always quick to respond to my requests and questions and deserves much thanks for his help.

There are the people of the 4th floor Elliott Bldg. I want to thank for their friendship and support these past two years. In particular, I would like to thank Dr. Kathleen Labrie, who was never too tired to hear me gripe about the difficulties of data reduction, and who always seemed to have the answer to the problems bugging my code.

From a personal standpoint, some of my biggest thanks goes to my wonderful girlfriend Melanie Orfus. She has supported me this whole time in spite of our separation. And although the past two years have been difficult being apart, we can take great comfort in the fact that this separation has made us much stronger.

I would like to thank my parents for their support, especially for instilling me

with the values of patience and perseverance which have been vital to completing this thesis. I wouldn't have gotten this far without their love.

Lastly, I would like to thank the late Dr. John Wilson. John, former neighbour, amateur astronomer and law professor at the University of Windsor, was the first person to reveal to me the marvels of astronomy when he gave me his copy of Stephen Hawking's *Black Holes and Baby Universes*. His fascination with the sky kindled in me the desire to understand the mysteries of the heavens. He is remembered fondly for his encouragement and his good advice, even when I was too young to understand it. It is to him that this thesis is dedicated.

Acronyms

ALMA Atacama Large Millimeter Array

AGN Active galactic nucleus

CFRS Canada-France Redshift Survey

CMB Cosmic microwave background

CNOC Canadian Network for Observational Cosmology

CO Carbon-monoxide (especially in reference to the rotational transition lines of the carbon-monoxide molecule)

COBE Cosmic Background Explorer

CSO Caltech Submillimeter Observatory

DIRBE Diffuse Infrared Background Experiment

FIR Far-infrared

HDF Hubble Deep Field

IMF Initial Mass Function

IRAS Infrared Astronomical Satellite

ISOCAM Infrared Space Observatory Camera

ISRF Interstellar Radiation Field

JCMT James Clerk Maxwell Telescope

LF Luminosity function

ORAC-DR Observatory Reduction And Control - Data Reduction

S/N Signal-to-Noise ratio

SCUBA Submillimeter Common User Bolometer Array

SED Spectral energy distribution

SFR Star formation rate

SIRTF Space Infrared Telescope Facility

SLUGS SCUBA Local Universe Galaxy Survey

SSRS Southern Sky Redshift Survey

SURF SCUBA User Reduction Facility

ULIRG Ultra-Luminous Infrared Galaxy

UV Ultraviolet

Chapter 1

Introduction

1.1 Preamble

The past ten years of astronomy have led to some of the most stunning breakthroughs in observational cosmology and extragalactic astronomy. Using a wide array of large, ground-based observatories and multi-wavelength space telescopes, the human eye has seen deeper into space and further back in time than ever before. Among other things, these contemporary observations have revealed that the global star formation rate—the rate at which galaxies form stars—was greater in the past. Furthermore, the rate at which galaxies undergo interactions was also greater in the past. This empirical evidence has led astronomers to study if a correlation exists between the two events: star formation and galaxy interaction. Such research is motivated by the physical consideration that when galaxies merge, cataclysmic amounts of energy can be released from collisions in the interstellar gas. As the gas radiates its energy it cools and condenses, forming regions of new stars. This thesis is concerned with how interactions among pairs of galaxies affect their star formation behaviours. Observations in the submillimeter part of the electromagnetic spectrum are used to determine star formation rates—the rate at which galaxies form stars out of interstel-

lar gas. These rates can then be compared to values from the literature; furthermore, star formation rates are a useful tool in confirming our understanding of the evolution of galaxies in the Universe. More will be said about the specific goals of this research in section 1.8.

1.2 Submillimeter Astronomy

1.2.1 Instruments and Observing parameters

Observations at submillimeter wavelengths (hereafter sub-mm; approximately defined as $100\ \mu\text{m}$ to $1\ \text{mm}$) are relatively new. In fact one of the reasons for the late flowering of sub-mm astronomy is the technical challenge of building receivers. Sub-mm wavelengths are too short for radio-like coherent detections (ie. arrays of receivers) and far too long for optical/infrared techniques. Compounding this technological problem are the effects of atmospheric absorption from water, which make the sky mostly opaque in the far infrared (FIR). There do exist, however, windows of varying degrees of transparency for which, if situated above most the Earth's water vapour, receivers can detect coherent radiation. These windows occur most prominently at wavelengths described in Table 1.1 and Figure 1.1.

Although the James Clerk Maxwell Telescope (hereafter JCMT) became operational in 1987, the only instruments available for continuum observing at sub-mm wavelengths were single-channel (i.e. single-element) bolometers like the UKT14 (which operated at JCMT between 1988 and 1996). With only one channel (i.e. one "pixel"), projects such as sky mapping were extremely slow, especially since the instrumental sensitivity was limited by detector noise. In the mid 1990s the Submillimeter Common User Bolometer Array (hereafter SCUBA) went into operation; it remains the most sensitive imaging device available to date in sub-mm astronomy. SCUBA has two major advantages over other previous sub-mm detectors. It is the first detector designed to have its sensitivity limited by photon noise (as opposed to

Table 1.1: Atmospheric transmission windows in the sub-mm band. Each window is denoted by a frequency of peak transmission.

Frequency	Wavelength	Beamwidth	Trans. ^a	Nights ^b
GHz	μm	arcsec		%
150	2000	28	0.97	90
230	1300	21	0.96	90
345	870	14	0.88	70
492	610	12	0.43	20
690	435	8	0.44	25
870	345	6	0.53	30

^a Zenith atmospheric transmission as a fraction of perfect transmission.
^b Percentage of nights with reported atmospheric transmission.

systematic detector noise). In principle, this allows it to have its performance limited by noise from the background radiation. It is also the first detector to consist of a large-scale array of bolometers (or pixels)—this is of exceptional value in mapping large areas of the sky. In fact there are two arrays: a short wavelength array, detecting radiation at $450\mu\text{m}$, with 91 bolometers; and a long wavelength array, sensitive to radiation at $850\mu\text{m}$, with 37 bolometers. (See Table 1.1 for beamwidth and transmission data. Note that the transmission in the $870\mu\text{m}$ window is twice as good, and useful on three times as many nights, as for the $435\mu\text{m}$ window. This will become very important later.)

Figure 1.2 shows the exact configuration of the bolometers in the long wavelength array. The circles drawn about the centres of each bolometer show the extent of the $13''$ beamwidth (half-max) to scale. Figure 1.2 illustrates the extent of deadspace in the array.

Both arrays form a “tightly” packed, nearly hexagonal shape with a field of view of ~ 2.3 arcmin. There are also three single bolometers for observations at 1.1mm, 1.35mm and 2.0mm respectively.

At a height of 4092m the JCMT is located far from most sources of atmospheric

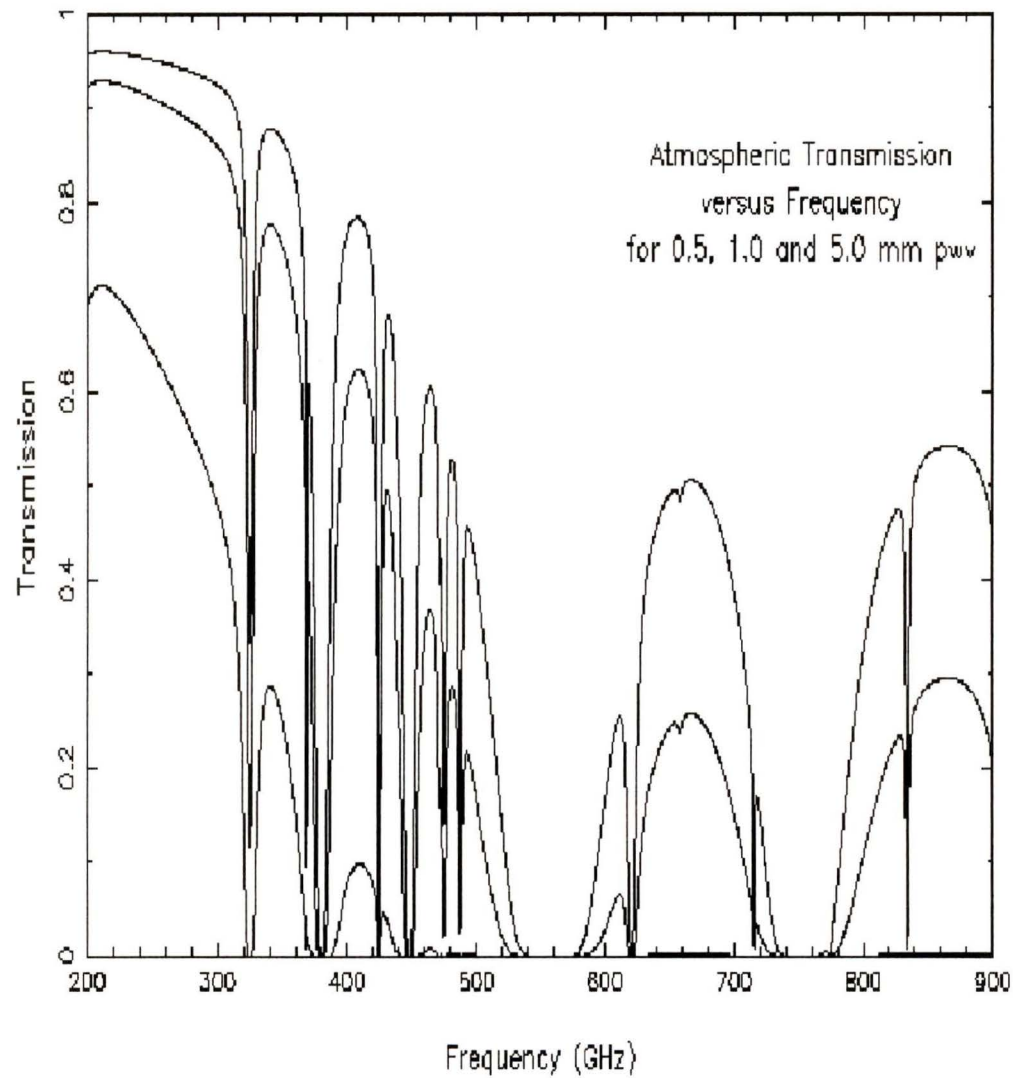


Figure 1.1: Windows of atmospheric transmission at sub-mm wavelengths. The three curves represent different amounts of water vapour in the atmosphere. The top curve shows transmission for 0.5 mm, followed by 1.0 mm and 5.0 mm.

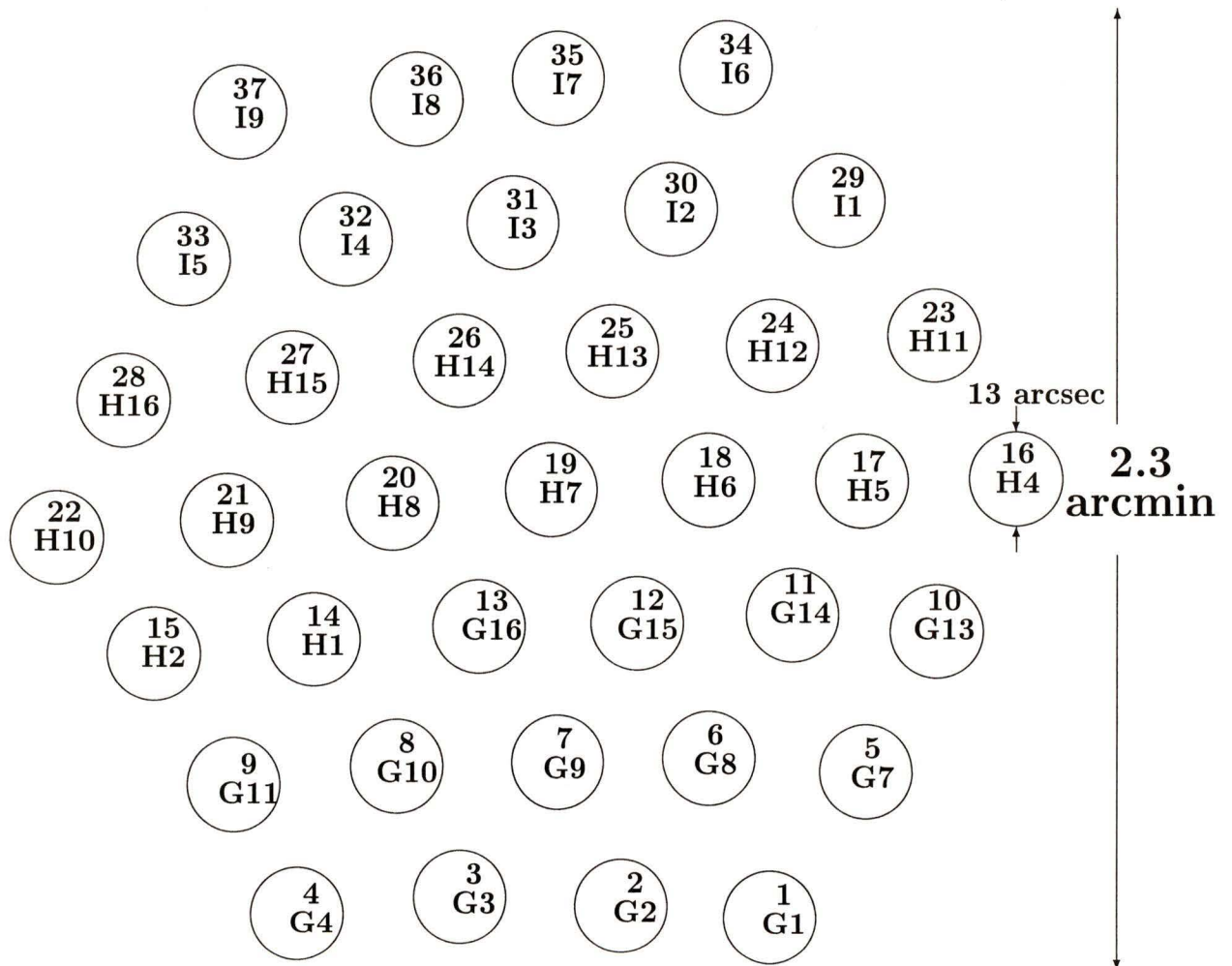


Figure 1.2: The SCUBA 850 μm array, showing 37 bolometers and their respective beamwidths. The beamwidths *are* to scale, all space in between beams is deadspace. Each beamwidth is 13'' (to half-maximum sensitivity).

and light pollution, and is above approximately 97% of the water vapour in the Earth's atmosphere—the main source of opacity. The telescope is mounted on an altitude-azimuth mount that results in field rotation about the central pixel. More will be said on this subject later.

Why Observe in the Submillimeter Band?

Given the technological and atmospheric challenges involved in observing at sub-mm wavelengths, one could be forgiven for asking the question “why build sub-mm detectors?” First, high redshift galaxies, which contain large amounts of dust, are actually predicted to become brighter with increasing distance at sub-mm wavelengths; this will be explained shortly. Second, until the inception of SCUBA the sub-mm band remained a poorly studied part of the spectrum. Given that sub-mm wavelengths provide a sensitive probe to the (dust obscured) star formation history of the Universe, building sub-mm detectors is a vital step to improve our understanding of such evolution.

In the far-infrared (FIR) we expect the spectral energy distribution (SED) of dusty galaxies to be a strongly increasing function of frequency (see Figure 1.3). As such galaxies are progressively redshifted, the portion of the SED observed by our sub-mm detectors “climbs” the dust peak, and so becomes brighter relative to what would be expected for a flat SED at the same distance. This increase in spectral brightness counteracts the decrease in flux density with distance, $S \propto \frac{1}{D_L^2}$, (where D_L is the luminosity distance) resulting in a strong, negative k-correction.¹ This effect applies to wavelengths $250 \mu\text{m} \leq \lambda \leq 1000 \mu\text{m}$, for which the flux density for galaxies $z > 1$ ceases to decline and remains about constant, or increases slightly (see Figure 1.4). This fortuitous astronomical effect opens up a window in the sub-mm for redshifts ranging from $z \simeq 1 - 8$, as similar galaxies in that range will have roughly

¹At cosmological distances a given spectral energy distribution is redshifted. The k-correction accounts for this effect by correcting the observed change in intensity to what would be expected if the source were not redshifted.

the same observed flux.

The negative k-correction has proven a boon to SCUBA surveys of high redshift galaxies. The first such survey detected a population of very luminous high redshift galaxies which were responsible for releasing a significant fraction of all energy generated by galaxies in the Universe (Blain et al., 1999). Strong evidence suggests that the mean redshift of this population is likely $z \simeq 2 - 3$ (Smail et al., 2000). Regrettably only a small portion of this sample has well determined redshifts—a problem that will be discussed shortly.

Selection Effects of Submillimeter Observations

Due to the strong negative k-correction, surveys in sub-mm bands will favour bright galaxies in the FIR at high redshifts. This well known effect was responsible for the aforementioned discoveries by Blain et al. (1999). However, another selection effect creates additional bias in SCUBA surveys: dust temperature. Given a fixed sub-mm flux density, a doubling of the dust temperature will result in an increase of inferred luminosity in the SED by a factor of $10\times$. This effect will occur at all but the very highest redshifts. This will bias observations in favour of detecting galaxies with hotter dust temperatures and omitting, or under-detecting, those with lower dust temperatures (Eales et al., 1999). Until a large sample of sub-mm galaxies with identified redshifts and multi-waveband SEDs are available a significant population of cold sub-mm galaxies could be missing or be misidentified (Blain and Phillips, 2002). The terms “warm” and “cold” to describe the temperatures of galactic dust are relative. (Much more on this will be said later, but, roughly speaking, “warm” refers to dust with a temperature of $\sim 40-60\text{K}$, while “cold” refers to temperatures of $\sim 20\text{K}$.) It is interesting to note that the detection rate of galaxies using SCUBA has declined since 1998. This is due in part to the disappearance of exceptionally dry atmospheric conditions induced by the El Niño effect in 1997-98.

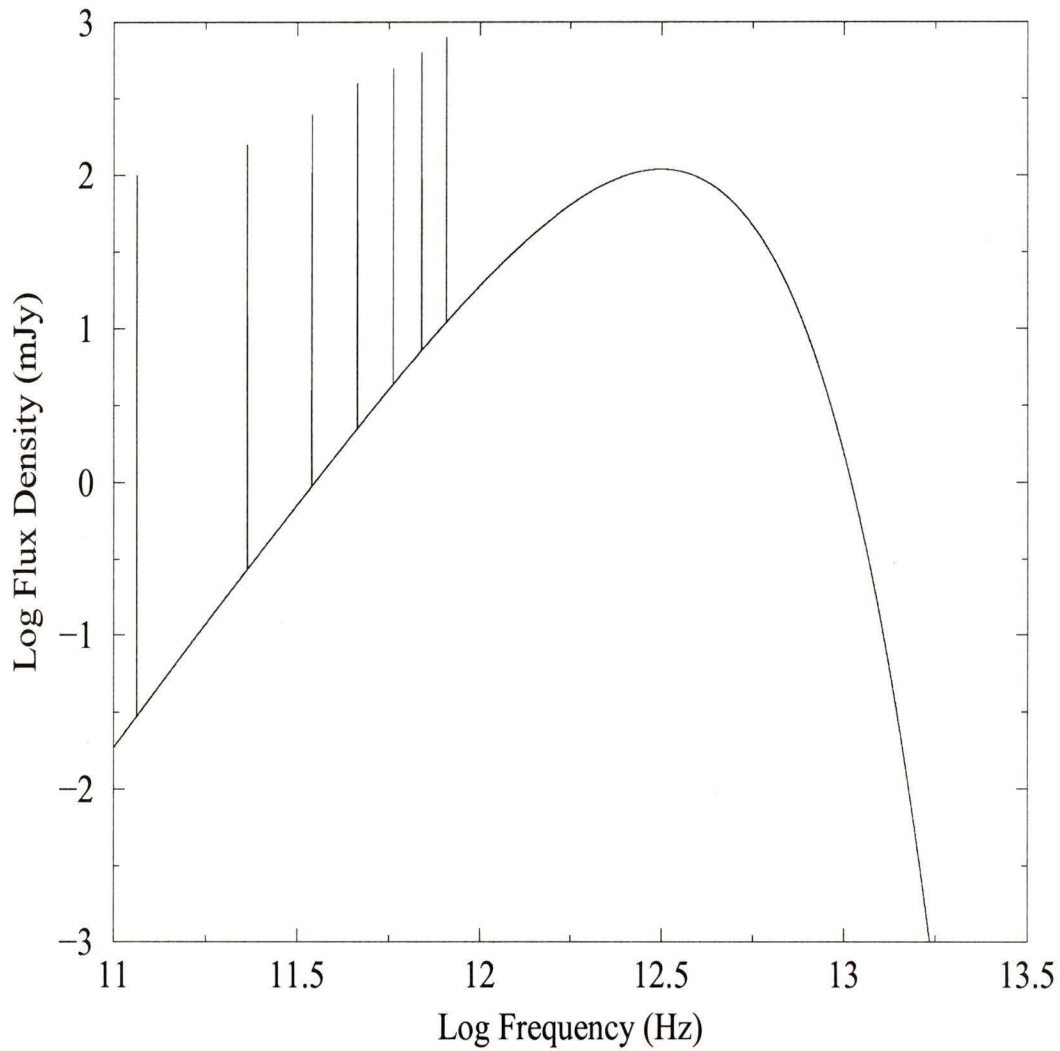


Figure 1.3: The spectral energy distribution for a galaxy with dust emission, normalized to unity at $850 \mu\text{m}$. The first 7 CO rotational emission lines have been included. There are 46 CO lines that have been calculated and observed.

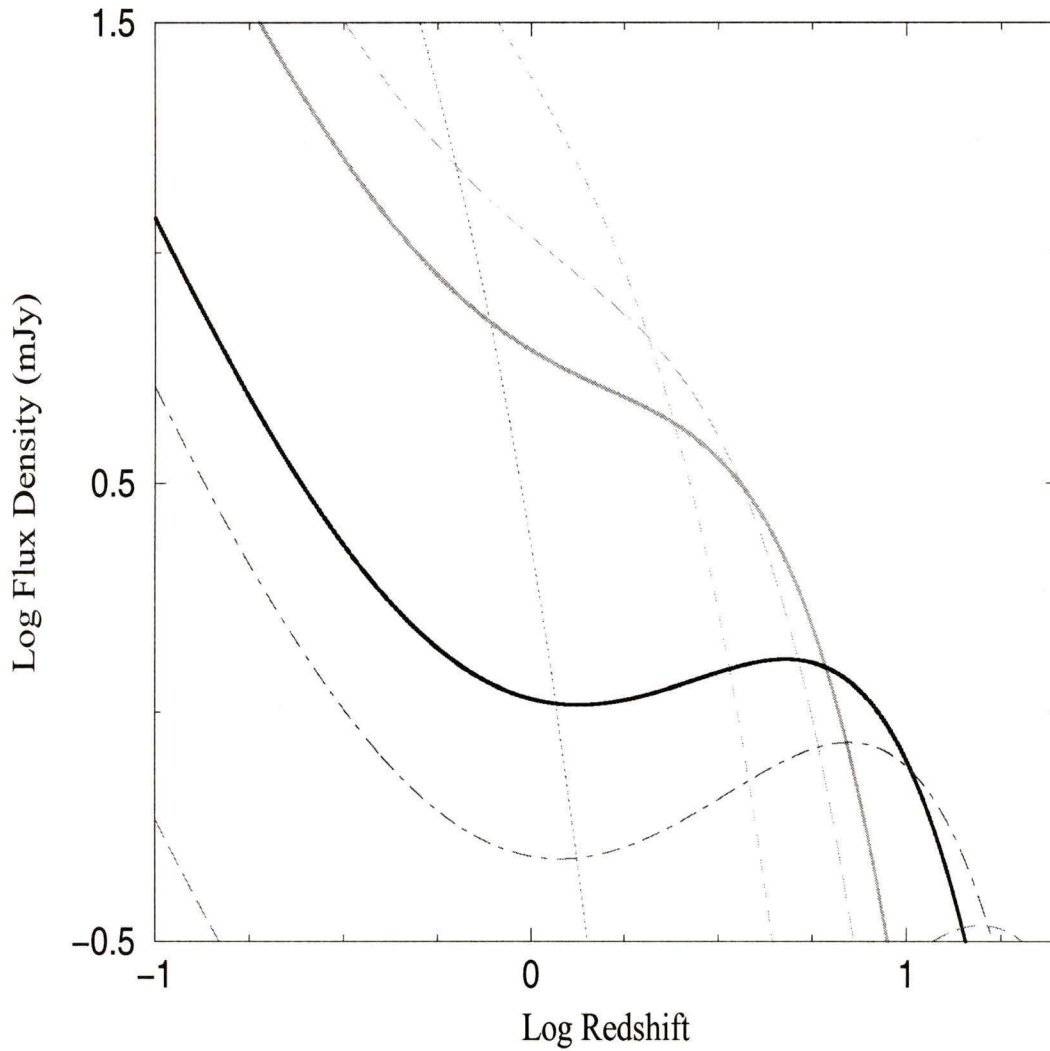


Figure 1.4: Flux density for a galaxy with $L_{FIR} = 5 \times 10^{12} L_{\odot}$, $T = 35\text{K}$, $H_0 = 65 \text{ km s}^{-1} \text{ Mpc}^{-1}$ and $\Omega = 1$. The upper solid line is $450 \mu\text{m}$ and the lower solid is $850 \mu\text{m}$. The others are as follows, starting from the top center to bottom left: $70 \mu\text{m}$, $200 \mu\text{m}$, $350 \mu\text{m}$, $1100 \mu\text{m}$ and $2200 \mu\text{m}$.

Determining Redshifts

One of the most vexing and persistent problems in sub-mm astronomy is identifying galaxies, i.e. finding their counterparts in other wavebands. The surest way of doing this is through the discovery of consistent sub-mm and optical/IR redshifts. This is straightforward in the optical/IR bands using standard spectroscopic techniques. However, in the sub-mm spectral region, only three galaxies have been identified this way (Frayser et al., 1998; Frayer et al., 1999). The difficulty originates from the narrow fractional bandwidth of receivers. Even for a relatively low frequency of 90GHz (3.3 mm) the target redshift must already be known to better than 0.5% to ensure that a typical linewidth of 300 km s^{-1} falls within a 1 GHz band (Blain et al., 2002). The main spectroscopic lines used for identifying SCUBA galaxies are the CO(3 \rightarrow 2) with rest frequency of 345 GHz ($867 \mu\text{m}$), which is detectable in SCUBA's long waveband; and CO(2 \rightarrow 1), with rest frequency of 691 GHz ($434\mu\text{m}$), detectable in the short waveband. (In the future, it may be possible to use [C II], $158 \mu\text{m}$ which emits $\sim 0.5\%$ of the luminosity of a starburst galaxy—e.g. Nikola et al. (1998).)

Since obtaining sub-mm spectroscopic measurements is exceedingly time consuming, other methods of determining sub-mm redshifts have been used. The most obvious alternative is the photometric redshift, whereby multi-waveband measurements are used to construct a low-resolution SED, which is then compared to template SEDs of various redshifts. Unfortunately this technique suffers from a critical degeneracy in the sub-mm which limits its effectiveness. Since the sub-mm SED is essentially a reflection of the presence of thermal dust emission, redshifting a template SED affects the observed colours in the same way as changing the dust temperature. Thus, even when multi-waveband FIR data is available, the redshift is indeterminate unless an intrinsic dust temperature is known. The SED of a galaxy may be plotted with respect to the parameter $(1+z)/T_d$, instead of just redshift or temperature. If either of the two are known (usually knowledge of T_d is more common than z) then the other can be interpolated from this relation. But in many cases dust temperatures

vary widely or are altogether uncertain and this method fails.

Fortunately there is another way of inferring redshifts from sub-mm galaxies that takes advantage of the radio/sub-mm relation. Excellent correlation has been found between flux densities in the FIR (60 μm and 100 μm) and radio (1.4GHz) for low redshift galaxies with a range of 4 orders of magnitude in luminosity (Condon, 1992). The correlation is thought to originate in star forming regions, in which the SFR—inferred by FIR dust emission—is proportional to the rate of supernovae. The supernovae in turn produce shock waves that accelerate electrons and induce synchrotron emission; this emission is observable at radio frequencies.

The ratio of flux density at 1.4GHz (radio) and 350GHz ($\sim 850 \mu\text{m}$) also yields redshift information (Carilli and Yun, 1999). Some degeneracy still exists for dust temperatures $< 60\text{K}$, but this relation is thought to be especially useful for observing optically faint sub-mm galaxies. One difficulty results at high redshift, where the CMB contribution to dust heating is no longer negligible. For Milky Way type SED's this is expected to happen around $z \simeq 5$. The increase in CMB temperature shifts the peak of the dust SED and actually counteracts the negative k-correction; the usefulness of the radio-sub-mm correlation is therefore limited to $z \lesssim 5$.

1.3 The Physics of Dust

Since sub-mm observations trace dust emission in the Universe, a discussion of the physics of dust is warranted.

1.3.1 Dust Absorption

The conventional way of quantifying dust absorption in observations is by use of $A(\lambda)$, the absolute extinction at any wavelength, expressed in magnitudes relative to some reference extinction $A(\lambda_{\text{ref}})$. By convention the reference wavelength is taken

to be V , the visual band centred at 5500\AA .

$$A_X = (m - m_0)_X, \quad (1.1)$$

where X is some band, m the observed magnitude and m_0 the hypothetical apparent magnitude without dust. Reddening is defined as the difference between observed and intrinsic extinction at two different wavebands.

$$\begin{aligned} E(X - Y) &= (m(X) - m(Y)) - (m_0(X) - m_0(Y)), \\ &= A_X - A_Y, \end{aligned} \quad (1.2)$$

A more useful measure of dust absorption is the fractional extinction at arbitrary λ relative to extinction in V : $A(\lambda)/A(V)$ (Cardelli et al., 1989). The quantity $A(\lambda)/A(V)$ has been parametrized for UV, optical and near infrared wavelengths in the following form:

$$\mathcal{A}(\lambda) = A(\lambda)/A(V) = \left(a(x) + \frac{b(x)}{R_V} \right), \quad (1.3)$$

where the quantity R_V is just the parameter:

$$R_V = \frac{A(V)}{E(B - V)}, \quad (1.4)$$

and is taken to be $\simeq 3.1$ (Mathis, 1990).

The functions $a(x)$ and $b(x)$ are defined for different ranges of wavelength in Cardelli et al. (1989). Note that the argument x of the functions $a(x)$ and $b(x)$ is just $1/\lambda$ in units of cm^{-1} . See Appendix A for functional forms of $a(x)$ and $b(x)$ at various wavelength ranges.

Together, these functions parametrize the shape of dust absorption, relative to the V band, over a range of wavelength of $0.125 \mu\text{m} \leq \lambda \leq 3.3 \mu\text{m}$. Note that this characterization is an attempt to fit absorption to empirical evidence and is not based on some a priori physical model of dust grains.

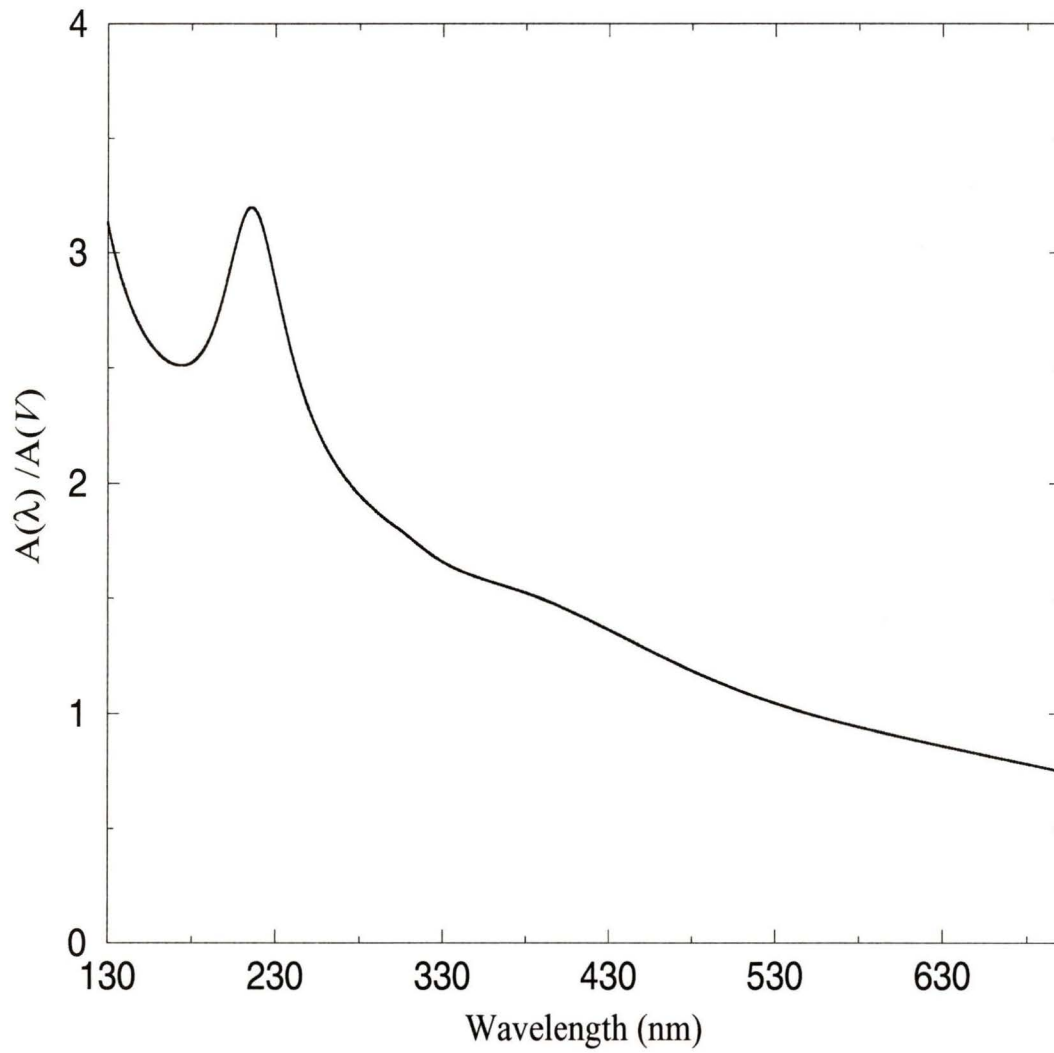


Figure 1.5: Dust absorption from ultraviolet to red wavelengths. The curve is normalized to unity for the V band (5500\AA).

As illustrated in Figure 1.5 the dust absorption spectrum peaks at 2175\AA , demonstrated by the “bump.” The cause for this feature is generally believed to be high abundance of carbon in graphite form (Mathis, 1990). Since dust absorption is peaked in the UV, sub-mm emission is an excellent tracer of young, hot stars that emit the bulk of their radiation in that regime. In effect, dust selects the radiation of hot OB stars preferentially and is heated up in the process. The energy absorbed is then re-emitted in a near blackbody spectrum at wavelengths in the FIR. Dust emission is thus a sensitive tracer of the presence of hot, young stars, which are in turn indicative of recent star formation. Depending on the intensity of the interstellar radiation field (ISRF) generated by starbursts, the dust grains can be heated to between 20K and 200K.

1.3.2 Dust Emission

Having explained the process of energy absorption by dust, with its sensitivity to young, hot stars, it is now left to explain how the dust re-emits that energy.

The spectrum of dust emission resembles a blackbody but with an important modification at long wavelengths:

$$f_\nu \propto \epsilon_\nu B_\nu, \quad (1.5)$$

where ϵ_ν is the frequency dependent emissivity given by:

$$\epsilon_\nu \propto \nu^\beta, \quad (1.6)$$

and β is the emissivity index². Scattering theory predicts that $\beta \rightarrow 2$ at low frequencies, while $\beta \simeq 1$ at high frequencies is consistent with observations of the ISM extinction curve at optical/UV wavelengths (Calzetti et al., 2000). Deriving β from

²Note: the true form is $f_\nu \propto [1 - \exp(-\tau_\nu)]B_\nu$, where τ_ν is the optical depth and is proportional to ϵ_ν .

general considerations would be difficult, and would require mixing different sizes and shapes of dust grains, each with their own characteristic index. β is often estimated by fitting SED's to multi-waveband observations of galaxies in the FIR and minimizing χ^2_ν to obtain the most reliable values of T and β . The exact form of ϵ_ν is difficult to obtain since it depends on a standard emissivity and mean grain size, both of which depend on β (Hildebrand, 1983).

The form of the spectral emission of dust also relies on the temperature (or temperatures) of the dust itself. The temperatures of dust responsible for sub-mm emission have typically ranged from $\sim 30\text{K}$ (Chini et al., 1989) to $\sim 60\text{K}$ (Hughes et al., 1993). However, for the purposes of this research the most definitive measurement of dust temperatures comes from the invaluable "SLUGS" survey of Dunne et al. (2000; see also Dunne & Eales, 2001).

The SCUBA Local Universe Survey (SLUGS) undertook a survey at $850\ \mu\text{m}$ and $450\ \mu\text{m}$ of 104 galaxies selected from the IRAS³ bright galaxy survey (BGS). These were galaxies with $S_{60\ \mu\text{m}} > 5.4\text{Jy}$, and a measured IRAS $100\ \mu\text{m}$ flux. The purpose was to sample the local Universe ($0.006 \leq z \leq 0.07$) and fit SED's using four flux measurements ($60\ \mu\text{m}$, $100\ \mu\text{m}$, $450\ \mu\text{m}$ and $850\ \mu\text{m}$). The fitting yields values of T_d and β for individual galaxies and a mean dust temperature for the local Universe. The first paper (Dunne et al., 2000) used only the long wavelength SCUBA data (along with both IRAS bands), and determined a mean dust temperature of $35.6 \pm 4.9\text{K}$ and $\beta = 1.3 \pm 0.2$, where the errors quoted are $\pm 1\sigma$. However, Dunne and Eales (2001) showed that when the $450\ \mu\text{m}$ data were also included, it was necessary to use two dust temperatures to fit the SED to the measurements properly. Thus, in addition to a body of dust at mean temperature 35.6K , another, colder dust component was needed, with temperature $\sim 20\text{K}$. The need for different temperature components was not new. Sodroski et al. (1994) reported that the bulk of the Galactic dust emission was associated with HI regions and cold molecular gas at a temperature range of

³IRAS is the Infrared Astronomical Satellite, launched in January 1983. It performed the first IR all-sky survey at wavelengths of $12\ \mu\text{m}$, $25\ \mu\text{m}$, $60\ \mu\text{m}$ and $100\ \mu\text{m}$.

17–22K, while a minority was associated with warm HII regions of ~ 29 K. That study used 140 μm and 240 μm data from the COBE Diffuse Infrared Background Experiment (DIRBE). The SLUGS results are directly comparable to other such studies, and represent the first systematic attempt to calculate dust temperatures in the local Universe using sub-mm wavebands. More will be said about SLUGS later.

1.3.3 Power Sources for Dust Emission

Until now the absorption and emission properties of dust have been discussed without reference to the energy sources that power that emission. Ultimately we are seeking to discover the nature of what lies behind the dust—i.e. what warms it, as opposed to the properties of the dust itself.

As was shown in section 1.3.1, the peak sensitivity of dust absorption is in the UV. Therefore, an intense source of UV photons would easily heat dust and produce the continuous spectrum just described. It is generally believed that hot, young OB stars are the power sources behind this heating, though radiation from AGN accretion disks would also heat dust in a similar way. Since it is star formation we wish to trace, we must assure ourselves that AGN's do not contribute significantly to the heating of dust. In typical spiral galaxies the dust emission is significantly extended, and associated with molecular gas-rich star forming regions (Regan et al., 2001). In galaxies of intermediate luminosity, the most intense knots of star formation are found in extra-nuclear regions (Wilson et al., 2000). This provides evidence that much of the dust energy is caused by star formation outside the nucleus where it cannot be attributed to AGN-heated dust emission. In more luminous galaxies, so-called Ultra Luminous Infrared Galaxies (ULIRG's) that are at sufficiently low redshift to resolve their internal structure, dust emission is concentrated in small, circumnuclear, disk-like regions of intense star formation (Downes and Solomon, 1998). While it is possible that dust emission is powered by an AGN, this would impose a very high column density on the dust and an extinction of many tens of magnitudes in the

optical/UV bands. Finally, recent studies of the cosmic extragalactic background light, measured by ISOCAM at $15 \mu\text{m}$ (Elbaz et al., 2002), have revealed that only 20% of extragalactic background radiation in the infrared is attributable to AGN's. Since this background light is a relic of the sum the of star formation (and AGN) dust heating history, we can likely neglect AGN as the major contributor to dust heating.

1.3.4 Submillimeter Emission

There are two sources of emission at sub-mm wavelengths: thermal continuum from dust, and line emission. About 99% of energy released in the sub-mm comes from the thermal continuum; the remainder comes from atomic and molecular transitions (Blain et al., 2002). Some of the most useful and interesting line features in the sub-mm originate with CO molecular rotational transitions, which appear as a “ladder” on the sub-mm SED, spaced about every $115/(1+z)$ GHz. CO rotational lines are by no means the only lines. Fine structure lines, such as the singly ionized carbon ($158 \mu\text{m}$) [C II] emission line, are important and account for $\sim 0.5\%$ of the FIR bolometric luminosity (Nikola et al., 1998). Others, such as CS, HCN and HCO^+ are also present in the sub-mm but are more common at the highest gas densities only, whereas CO is more common at densities of the interstellar matter.

1.4 Star Formation Rate Indicators

1.4.1 Modeling Star Formation

Individual stars are unresolvable in all but the closest galaxies. Therefore, obtaining a measurement of the star formation rate must be accomplished by taking integrated light measurements either of continuum emission or nebular lines. This can be done in various wavelength regimes. Each will be discussed, in the following sections. Before the various methods are discussed it is worthwhile explaining the

principle behind the inferences made about star formation rate (SFR).

Stars generally form in clusters and associations, and have varying composition, mass, and spectral types. Stellar masses between $0.4M_{\odot} \leq M \leq 10M_{\odot}$ are distributed according to the Salpeter initial mass function (IMF) (Salpeter, 1955), which is a power-law with an exponent -1.35. Thus, at the high mass end of the distribution numbers of stars are far fewer⁴. However, even though these massive stars are small in number they contribute the bulk of the radiation in any new population of stars, since the luminosity of main sequence stars scales roughly as $\propto M^{3.5}$. As mentioned, massive, hot stars are highly indicative of a newborn population since such stars live only for $10^7 - 10^8$ years on the main sequence (H-burning) phase. This is in contrast to the lifetimes of most other main sequence stars (e.g. 10^{10} years for $1 M_{\odot}$). By measuring the luminosity of young stars, a measure of an instantaneous star formation rate can be inferred.

Having explained the motivation behind observations of young stars, there is still the task of relating these observations to a SFR in units of $M_{\odot} \text{ yr}^{-1}$. This is done with the help of spectral synthesis models that track the evolution of stars of various mass and spectral type over time, for a given rate of star formation. The most often-used computer models were written by Bruzual and Charlot (1993). They combined photometric isochrone synthesis models with an updated library of stellar spectra that ranged from the extreme UV to FIR. Model atmospheres were used to generate stellar spectra which were assigned to stars on evolutionary tracks in a colour-magnitude diagram. The evolution of flux was computed by convolving the SED for individual stars with a well-defined time-evolution of star formation rate. The models assumed a Salpeter IMF with upper and lower stellar masses given by $0.1M_{\odot} \leq M \leq 125M_{\odot}$. These models were evolved for various forms of $\text{SFR}(t)$: instantaneous, constant, and exponentially decreasing with different characteristic timescales. The results conformed with observed spectra of nearby galaxies of different Hubble type after several billion years of evolution. The power radiated in the UV can then be expressed

⁴The behaviour of the IMF for masses greater than $> 10M_{\odot}$ is not well known (Larson, 2002)

in terms of SFR for a give burst type. Madau et al. (1998) determined that the form of the SFR/L_{UV} was insensitive to the characteristic timescale of an exponentially decreasing starburst. This allowed them to relate UV luminosity at an arbitrary UV wavelength to a star formation rate. This method is really only applicable at $\lambda \leq 400\text{nm}$ (Pritchett, 1994).

1.4.2 Ultraviolet Continuum Indicators

The UV spectrum in the wavelength range $1250 - 2500\text{\AA}$ is dominated by hot, young stars and is relatively free from spectral contamination from older stellar populations. Due to this relative spectral purity the SFR simply scales with luminosity: the brighter the integrated UV light measured, the more stars that are forming. For ground-based observations these wavelengths are inaccessible due to atmospheric opacity in the UV. However, for galaxies with redshifts $z \sim 1 - 4$, rest wavelength UV photons are observable at visual wavelengths, thus making UV the most useful and direct SFR indicator for large look-back times.

The conversion between UV luminosity (over the wavelength range $1500\text{-}2800\text{\AA}$) and SFR has been recently calibrated by several authors (Cowie et al., 1997; Madau et al., 1998), who use models from Bruzual and Charlot (1993):

$$SFR(M_{\odot} \text{ yr}^{-1}) = 1.4 \times 10^{-28} L_{UV}(\text{ergs s}^{-1}\text{Hz}^{-1}). \quad (1.7)$$

Note that the composite spectrum is fairly flat over the range $1500\text{-}2800\text{\AA}$; this allows equation 1.7 to hold at any λ in this range. One note of caution: it must be assumed that the star formation has remained roughly constant over times scales that are long compared to the lifetimes of the dominant stars ($< 10^8$ years).

The principal advantage to using UV luminosity to gauge star formation is that this radiation is directly related to the atmospheric emission from young stellar populations. Additionally, because the rest wavelength emission is centred in the UV, it can be observed in the optical bands up to redshift ~ 4 . The main problem with

this method is that, as has been discussed, UV emission is very sensitive to dust absorption.

1.4.3 Emission Line Indicators: [O II] and H α

Nebular emission lines can also be used to measure star formation rate. These spectral lines form in hot, diffuse gas, energized by an embedded source. The lines re-emit integrated stellar light from below the Lyman limit (rest wavelength 912Å) and should be a good tracer of that population. The often-used [O II] line, a so-called “forbidden” line⁵ with a rest wavelength of 3727Å, is actually a doublet (3726,3729Å). The excitation of these states is sensitive to the abundance and ionization state of the gas, and can be calibrated against SFR. This calibration, however, is not done using models, as was the case for continuum UV luminosity. Rather, it is calibrated empirically with another emission line indicative of star formation (H α 6563Å).

$$SFR(M_{\odot} \text{ yr}^{-1}) = (1.4 \pm 0.4) \times 10^{-41} L_{[\text{O II}]} (\text{ergs s}^{-1}). \quad (1.8)$$

Again, since [O II] is in the UV, it can be used at large redshifts.

Calibrations between the H α emission line and SFR have been calculated from models, for example Madau et al. (1998). The models assume line recombination at an effective temperature of 10000K, and further assume no dust absorption.

$$SFR(M_{\odot} \text{ yr}^{-1}) = 7.9 \times 10^{-42} L(\text{H}_{\alpha})(\text{ergs s}^{-1}). \quad (1.9)$$

1.4.4 FIR Continuum Indicators

As discussed in the previous section, dust absorbs a significant portion of UV light and re-emits it as a thermal grey-body at wavelengths between roughly 10 and

⁵Forbidden lines result from atomic transitions between metastable states, with lifetimes of the order of a second. In high density gas frequent collisions inhibit the occupation of metastable states, favouring instead unstable states with very short lifetimes ($\sim 10^{-8}\text{s}$). Only low density gas will allow electrons to occupy metastable states and produce forbidden lines by spontaneous radiative de-excitation.

300 μm . Since the absorption is so strongly peaked in the UV, dust re-emission is a good tracer of star formation rate. Dust emission is sensitive to instantaneous star formation under two circumstances. First, the dust emitting in the FIR must be localized around a region of starburst activity; otherwise the radiation processed will reflect other physical processes or star formation elsewhere. Second, the dust opacity must be high; otherwise a significant fraction of the radiation will pass through the dust, and not be absorbed.

As revealed by Dunne and Eales (2001) and others, there are generally two spectral components of dust in galaxies. One is “warm” with temperatures of $\sim 40\text{K}$ and associated with dust surrounding regions of newly formed stars; this component dominates the $\sim 70 \mu\text{m}$ spectrum. The other is “cold”, at about $\sim 20\text{K}$; this is often referred to as “cirrus” because of its wispy or diffuse nature. Its structure is more extended than its warm counterpart, and its heating is associated with the interstellar radiation field; this dust component dominates the $\sim 100 \mu\text{m}$ spectrum. The relation between the cold component and star formation is much less clear than for the warm component. In bluer galaxies, both components are dominated by young stars; but in redder galaxies the extent of heating by older stars could be important, thereby biasing dust emission as a reliable indicator of SFR.

The calibration of SFR with L_{FIR} uses the same spectral synthesis models as described in section 1.4.1, but the the values of the conversion factor depend on stellar age in the models. The calibration is also affected by uncertainty in the relative contributions of the two dust components mentioned above. One of the most cited calibrations is that used by Kennicutt (1998a):

$$\begin{aligned} SFR(M_{\odot} \text{ yr}^{-1}) &= 4.5 \times 10^{-44} L_{FIR}(\text{ergs s}^{-1}), \\ SFR(M_{\odot} \text{ yr}^{-1}) &= 1.72 \times 10^{-10} L_{FIR}(L_{\odot}). \end{aligned} \tag{1.10}$$

This calibration is based on models by Leitherer and Heckman (1995); there are many other calibrations in the literature. At one end is the study by Scoville et al. (1983),

who, by assuming a starburst of length 10^9 yrs, found:

$$SFR(M_{\odot} \text{ yr}^{-1}) = 0.77 \times 10^{-10} L_{FIR}(L_{\odot}). \quad (1.11)$$

Thronson and Telesco (1986) used a Salpeter IMF to determine SFR's for O, B and A stars averaged over 2×10^6 years; assuming that all optical/UV radiation was absorbed by surrounding dust, they found:

$$SFR(M_{\odot} \text{ yr}^{-1}) = 2.1 \times 10^{-10} L_{FIR}(L_{\odot}). \quad (1.12)$$

However, the conversion factor may rise as high as 6.5×10^{-10} when stars of all masses are included.

The various conversion factors, ranging from $0.8 - 6.5 \times 10^{-10}$, differ in their choice of IMF and timescale of starburst. This thesis uses the value of Kennicutt (1998a) because of its use of Leitherer and Heckman's (1995) models. These models used the most up-to-date stellar atmospheres, and the best-available parametrization of stellar winds and evolution. The parameter space used in their models was chosen with infrared luminous starbursts in mind. It extends to both extremes of star formation: an instantaneous starburst, and a constant star formation over $\geq 3 \times 10^8$ years. This is a burst lifetime that seems reasonable for interacting galaxies—e.g. Barton et al. (2000).

1.4.5 Radio Luminosity

Radio continuum radiation at 1.4GHz is mainly produced by relativistic electrons. It is now generally believed that supernova shock fronts are responsible for accelerating these electrons, and this view has been reinforced by the close correlation of radio and FIR continuum, indicating that massive stars are the ultimate cause of both radiative mechanisms. If the average supernova rate is related to the SFR then the 1.4GHz radio luminosity can be correlated to star formation (Condon, 1992) as follows:

$$SFR(M_{\odot} \text{ yr}^{-1}) = 2.5 \times 10^{-22} L_{1.4GHz}(\text{W Hz}^{-1}). \quad (1.13)$$

1.4.6 Comparing Star Formation Indicators

Given the various methods of detecting star formation, one must ask which one is the most effective—that is, which determines the true SFR? The answer depends on the physical conditions of star formation. In a region where dust absorption is weak and nebular emission lines are faint, the UV continuum should provide the most realistic estimate. In starbursts heavily enshrouded by dust, the FIR continuum should provide the most accurate SFR, assuming that the radiation is not processed by emission lines before dust absorption. But in the most general situation, a more complicated picture emerges. Unless dust and gas content are known beforehand it is impossible to choose *a priori* which method to use. Therefore, a more accurate method might be to combine the SFR indicated in several of these methods, including especially the UV and FIR continuum.

The most critical discrepancy in SFR indicators is between the UV and FIR continuum. Since multiwavelength surveys are less common than observations at one waveband, the simplest way to estimate true star formation is to use a correction for the band that is being used. The 15 μm Infrared Space Observatory (ISO), observed a field of the Canada-France Redshift Survey (CFRS), and determined that SFR's inferred by UV fluxes are likely to be $\sim 3 - 4\times$ smaller than those determined using FIR fluxes (Flores et al., 1999; Hopkins et al., 2001), even at high redshifts (Blain et al., 1999). Other work has confirmed that the underestimation of SFR by UV continuum measurements alone is at least a factor of a few (Bell, 2002), while others quote that SFR estimators of by Kennicutt (1998a) are accurate to within a factor of $\sim 2\times$ (Inoue, 2002).

The factor by which optical/UV SFR's are underestimated is currently a matter of debate, particularly for $\text{H}\alpha$ SFR measurements. One study (Kewley et al., 2002) has shown that, before correcting for reddening, FIR inferred SFR is $\sim 3\times$ greater than the $\text{H}\alpha$ SFR, and increases with $\text{H}\alpha$ strength as follows:

$$\text{SFR}(\text{FIR}) = (2.7 \pm 0.3)\text{SFR}(\text{H}\alpha)^{1.30 \pm 0.06}. \quad (1.14)$$

When a reddening correction is applied to the $H\alpha$ SFR's the relationship comes into much closer agreement, as follows:

$$\text{SFR(FIR)} = (0.91 \pm 0.04)\text{SFR}(H\alpha)^{1.07 \pm 0.03}. \quad (1.15)$$

However, a more recent study (Cardiel et al., 2003) showed the exact opposite— that $H\alpha$ still underestimates SFR even when corrected for extinction. At least one other author (Hopkins et al., 2001) tries to explain the discrepancy between $H\alpha$ and infrared SFR with a reddening law that increases with increasing SFR. Clearly, how this issue will be settled is uncertain. Nevertheless, it is clear that dust attenuates optical and UV continuum photons by a factor of on average $\sim 2 - 3$, and that optical/UV SFR's are underestimated by the same factor. As we shall see, dust absorption probably varies significantly from galaxy to galaxy.

1.4.7 Total Star Formation Rate

As mentioned in the previous section, a reasonable method for determining the total SFR might include combining several methods. Certainly there is a case for combining FIR estimates of SFR with those of the optical/UV given the attenuation by dust. In this section we discuss the theoretical justification for such a method.

To determine if a combination of FIR and optical/UV SFR is an accurate indicator of the true star formation rate we begin with a flat UV spectrum, typical of the star forming regions of many galaxies (Bruzual and Charlot, 1993). With no absorption the flux from this spectrum is calibrated to infer a star formation rate of $1 M_{\odot} \text{ yr}^{-1}$. The UV spectrum is then obscured by dust, using the parametrized dust absorption function:

$$I_{\text{Obs}}(\lambda) = I_0 e^{-\mathcal{A}(\lambda)\tau_V}, \quad (1.16)$$

where I_{Obs} represents the observed, or attenuated, intensity at UV wavelength $1000\text{\AA} < \lambda < 4000\text{\AA}$, I_0 is the unobscured UV intensity, fixed at $7.14 \times 10^{27} \text{ ergs s}^{-1} \text{ Hz}^{-1}$; $\mathcal{A}(\lambda)$ is the dust absorption function (see equation 1.3); and τ_V is the absorption in the V

band. Figure 1.6 shows the attenuation of UV spectral intensity by dust for varying degrees of absorption.

Energy absorbed by dust in the UV is re-emitted in the FIR ($8 \mu\text{m} - 1000 \mu\text{m}$). The exact amount of energy re-emitted in the far infrared is then equal to:

$$L_{\text{FIR}} = \int_{1000\text{\AA}}^{4000\text{\AA}} I_0(1 - e^{-A(\lambda)\tau_V}) d\nu, \quad (1.17)$$

Thus, for a given level of absorption the energy in the UV and the FIR can be calculated. And since UV and FIR flux can be converted to SFR (equations 1.7 and 1.11, respectively), the two estimates of SFR can be compared.

One more factor must be taken into consideration. As observed in figure 1.6 the amount of absorption depends on wavelength. Clearly, a relatively large amount of energy is absorbed near 2150\AA , while relatively less absorption occurs for $\lambda > 2700\text{\AA}$. To properly estimate the UV SFR the *mean* intensity for a given τ_V must be used, rather than the intensity at a particular wavelength. Figure 1.7 demonstrates the result of measuring the total SFR, using UV absorption at a particular wavelength, rather than the mean absorption over all wavelengths.

Figure 1.8 shows the UV, FIR and total (UV + FIR) SFR's as a function of absorption. The true value of SFR is set to $1 M_{\odot} \text{yr}^{-1}$. Clearly, the combined UV and FIR SFR are a good estimator of the true value.

1.5 Mergers and Induced Star Formation

1.5.1 Mergers and Interactions

Since this research is concerned with star formation in interacting pairs, it is necessary to discuss the nature of mergers and interactions. This topic gained considerable interest upon release of the IRAS results (Soifer et al., 1984), which revealed

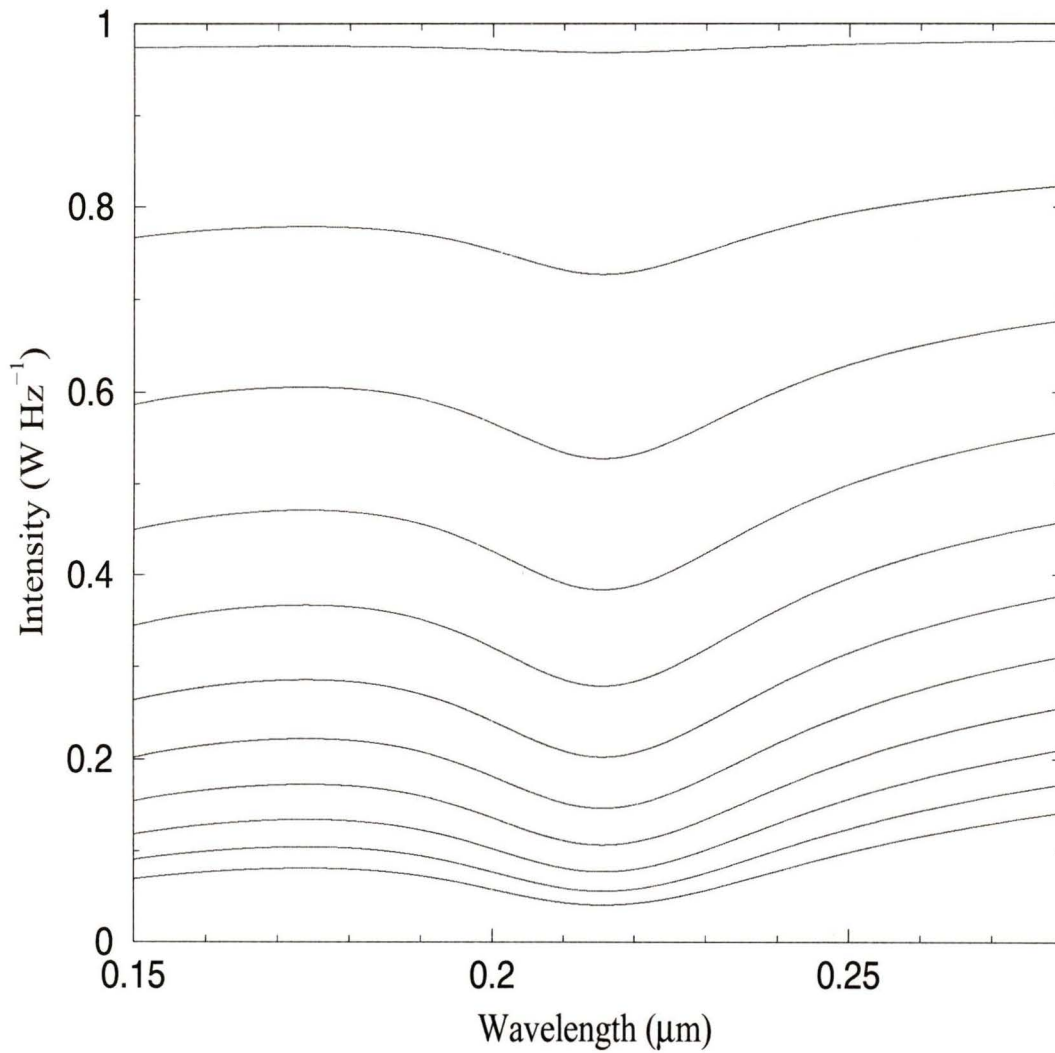


Figure 1.6: Dust absorption within the range $1500\text{\AA} < \lambda < 2800\text{\AA}$ for degrees of absorption, τ_V . The top curve represents the normalized UV intensity for $\tau_V = 0.01$. The second-to-top curve shows intensity for $\tau_V = 0.1$. Each successive curve shows the intensity with τ_V incremented by 0.1.

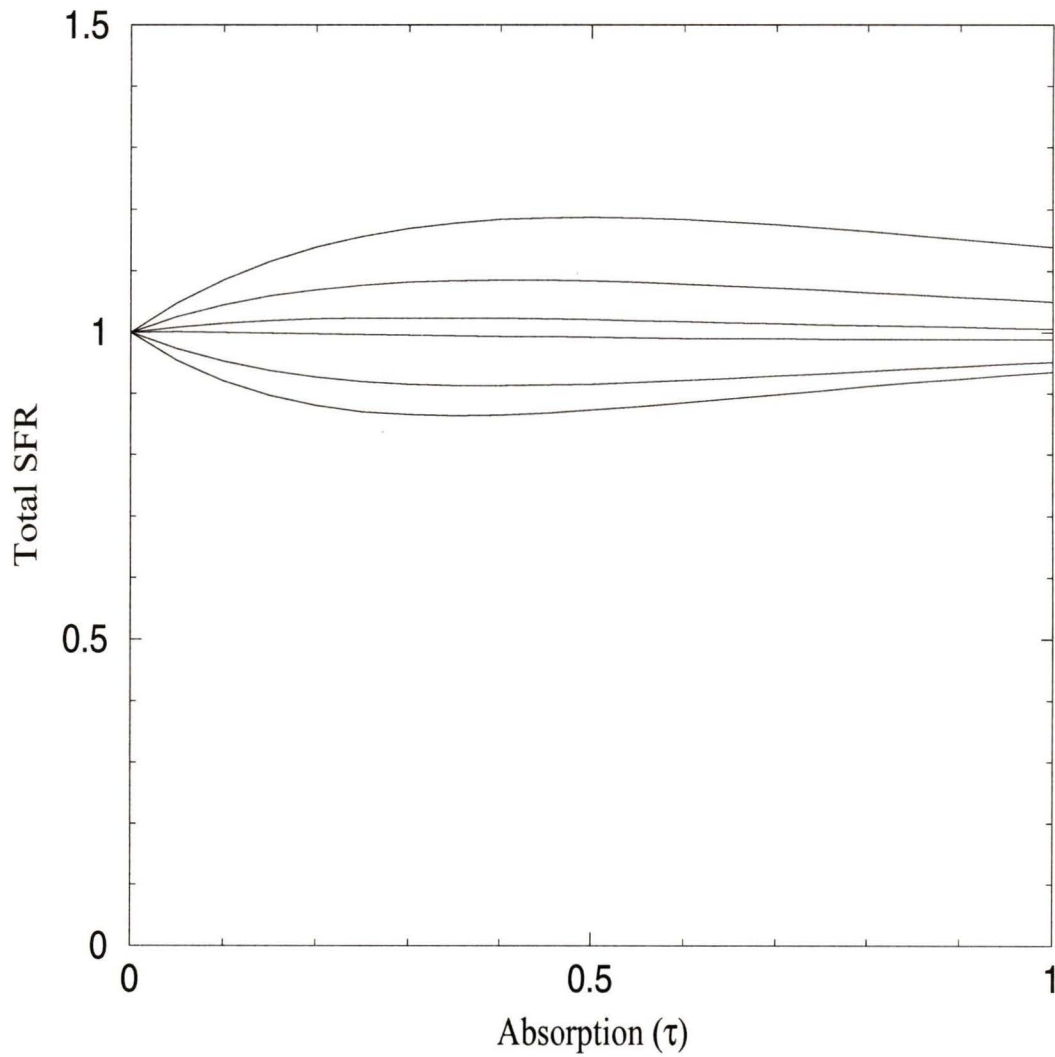


Figure 1.7: The total SFR (FIR+UV). Each curve represents the total taken with a UV measurement at a different wavelength. Due to the non-uniform absorption across the UV spectrum, certain wavelengths underestimate or overestimate the mean amount of absorption. The wavelengths used, going from top to bottom, are: 4000Å, 2800Å, 1250Å, 1750Å, 2100Å and 1200Å.

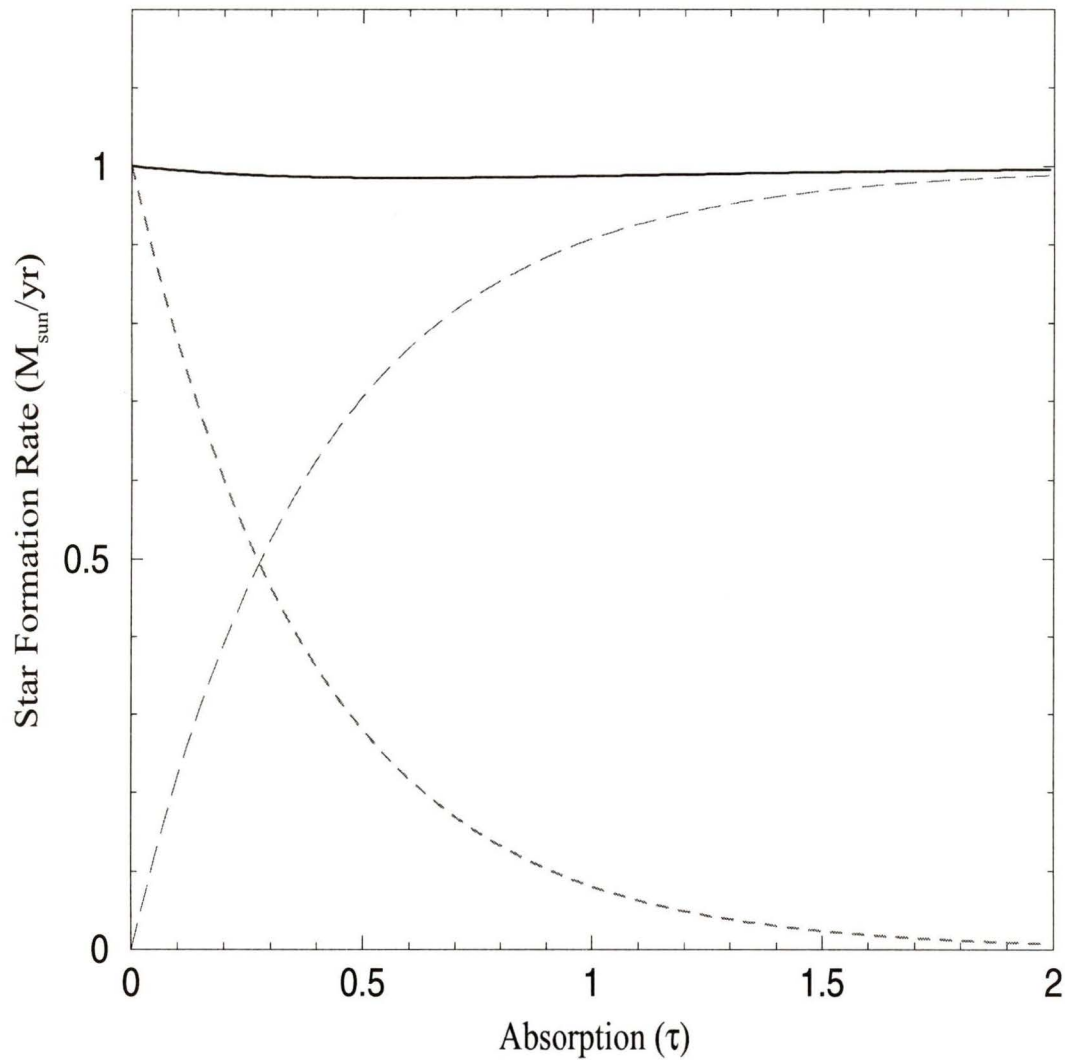


Figure 1.8: This plot demonstrates that the sum of UV and FIR SFR give an accurate estimate of the true SFR ($1 M_{\odot} \text{ yr}^{-1}$). The short-dashed curve shows the UV SFR decreasing as the absorption, τ_V , increases. The long-dashed curve shows the FIR SFR increasing to a maximum of $1 M_{\odot} \text{ yr}^{-1}$. The top (solid) curve shows the total SFR (UV + FIR). It remains consistently near the true value.

a large population of galaxies emitting the bulk of their bolometric luminosity in the infrared. The most luminous of these galaxies exhibited such a frequency of merger activity that follow-up research was soon underway to study this further (Sanders et al., 1988).

The most generally accepted explanation for merger-induced star formation contends that star formation is triggered as a result of collisions between gas-rich galaxies. Note that in the absence of interstellar gas, mergers and interactions cannot produce star formation. A good example of this is the pair NGC 750/751, two elliptical galaxies in the later stages of a merger which show no increase in star formation (Kennicutt et al., 1998).

There are two ways to measure the effect of interactions on star formation. The first is to compare the star formation rates in merging or interacting systems with those observed in a control sample of isolated galaxies. The difficulty with this approach is in finding a suitable control sample. The other method involves measuring the frequency of starburst galaxies among mergers. This approach will yield information about the relative importance of mergers in fuelling starbursts, but it is difficult to compare this information with non-merger populations. If comparisons are desired the best method is the former.

Before reviewing the body of knowledge concerning mergers and star formation, it is instructive to review the range of interactions referred to as merger events. At the “early” end of the spectrum are interacting systems like Arp 281, which shows only weak merger activity through a distorted HI structure (Rand, 1994). This is followed by galaxies undergoing the first stage of physical interaction, like NGC 4038/4039—also known as the “Antennae” galaxies. An example of a mid-encounter pair is M51, also known as the “Whirlpool” galaxy, and its less famous companion NGC 5195. Finally we come to Arp 220, which reveals a double nucleus, suggestive of the final stages of a merger (Graham et al., 1990). M82, while a strong starburst, shows only vestigial evidence of interaction, in the form of a HI tidal bridge to M81 (Yun et al., 1993).

Correlations between galaxy interaction and star formation enhancement were found as early as the 1970's. Larson and Tinsley (1978) discovered that morphologically normal and peculiar galaxies differed in their distribution in the $(U-B, B-V)$ colour-colour diagram. (By morphologically peculiar, the authors refer to those galaxies showing signs of interaction or merger activity; these galaxies were drawn from the Arp catalog.) The non-interacting galaxies obeyed a precise correlation in this diagram, while interacting galaxies showed considerable scatter. Larson and Tinsley showed that by modelling starbursts of varying age and intensity, the scatter of the two populations could be explained. The observations of non-interacting galaxies coincided with models of decreasing SFR and relatively large time scales $\lesssim 5 \times 10^8$ yr. The observations of interacting galaxies most closely resembled models with short ($\sim 2 \times 10^7$ yr) and intense bursts of star formation. Additionally, those interacting pairs in the initial stages of interaction showed colours associated with the most recent bursts, as predicted by their models. This study was among the first to demonstrate the association between induced star formation and interaction phenomenon with a large sample of galaxies.

Although there are many other papers published about correlations between mergers and SFR for various galaxies, the first complete, comprehensive study examined the phenomenon in Markarian galaxies (Keel and van Soest, 1992). Note that these galaxies were chosen from the First Byurakan Survey and so constitute optically selected starbursts. The study found that 36% of 516 non-Seyfert Markarian galaxies were in pairs, or possessed double nuclei. Although this survey provided sound evidence for merger-induced star formation, the remaining $\sim 60\%$ of galaxies in that survey, which are also starbursts, indicate that obvious interactions need not be the sole trigger of starbursts.

Two other studies showed the correlation between mergers and star formation in a more quantitative sense. Bushouse (1987) and Kennicutt (1987) found a modest enhancement of SFR by $\sim 2.5\times$ among interacting pairs when compared to a control sample. This was measured using the equivalent line widths (EW) of the $H\alpha$ and $[N II]$

lines. The mergers demonstrated increased equivalent width, which signifies increased SFR, though the dispersion was considerable (Kennicutt et al., 1994). Kennicutt also showed that no correlation existed between Hubble type and SFR for interacting galaxies; this discovery came as a surprise, given that a correlation does exist for non-interacting objects.

Comparisons with kinematical parameters, like relative velocity separation, have shown that an anticorrelation exists between velocity separation and SFR (Keel, 1993). Barton et al. (2000) explain the anti-correlation in terms of fading starbursts following interactions. In other words, close encounters do trigger starburst activity — activity that decreases as the companion recedes.

1.5.2 Ultra-Luminous Infrared Galaxies (ULIRG's)

The IRAS survey catalogued ~ 30000 galaxies at 12, 25, 60 and 100 μm (Soifer et al., 1987). Among these were a population of luminous galaxies emitting prodigious amounts of radiation in the infrared $\geq 10^{12}L_{\odot}$; these are ultra-luminous infrared galaxies, now called ULIRG's. The IRAS ULIRG's showed a general excess of companions and tidal signatures compared with optically selected galaxies of comparable luminosity. However, what was particularly striking was the incidence of mergers and interactions among ULIRG's. Furthermore, the interaction frequency increased with luminosity, from 20-30% for $L_{IR} \leq 10^{10}L_{\odot}$, to $\geq 90\%$ for $L_{IR} \geq 10^{12}L_{\odot}$. Indeed, the observations revealed that the most luminous ULIRG's were associated with evolved mergers, rather than just tidal interactions (Sanders et al., 1988). This showed that, while interactions were not necessary to power normal starbursts, they were required to power the most luminous ones. Due to their considerable energy output, originating from the most intense starbursts (and possibly AGN activity), mapping this power is critical to understanding the star forming history of the Universe.

1.5.3 Star Formation in Interacting Pairs

Star formation rates among interacting pairs have also been analysed according to the surface gas density observed, using a Schmidt Law. Schmidt (1959) used a power-law to relate the observed surface density of gas to inferred star formation rate:

$$\Sigma_{\text{SFR}} = A \Sigma_{\text{gas}}^N. \quad (1.18)$$

Most starbursts can be characterized by the linear, or near-linear regime, where the exponent, N , is close to unity. Kennicutt (1998a) found that a value of $N = 1.4 \pm 0.15$ and $A = (2.5 \pm 0.7) \times 10^{-4}$ closely described the star formation properties among normal spiral and starburst galaxies. This relation was observed for star formation rates of $10^{-3} \text{ M}_{\odot} \text{ yr}^{-1} \text{ kpc}^2$ in normal spirals, to $\sim 10^3 \text{ M}_{\odot} \text{ yr}^{-1} \text{ kpc}^2$ in circumnuclear starbursts.

By way of comparison, the dynamical free-fall timescale for one Milky Way mass of gas ($\sim 10^{11} \text{ M}_{\odot}$) to coalesce at the galactic nucleus and form stars with 100% efficiency is $1 - 2 \times 10^8$ years; this gives an idealized upper limit to the star formation rate of $\sim 500 - 1000 \text{ M}_{\odot} \text{ yr}^{-1}$.

1.6 The Star Formation History of the Universe

Measuring the local effect of interactions on star formation is not the only tool for understanding star formation history. From a more global perspective, we are interested in star formation throughout the history of the Universe. To understand the evolution of star formation, the co-moving SFR density, ρ_{SFR} , is generally used. This quantity measures the rate of star formation per unit co-moving volume in the Universe, expressed in units of $\text{M}_{\odot} \text{ yr}^{-1} \text{ Mpc}^{-3}$. Of particular interest is the question: what is the star formation behaviour of the Universe at large look-back times? As a rough illustration of the problem, we note that, if the current visible mass of the Milky Way ($\sim 10^{11} \text{ M}_{\odot}$) were to have formed at its present star formation rate ($\sim 1 \text{ M}_{\odot} \text{ yr}^{-1}$),

the timescale for this to happen would exceed the age of the Universe by $\sim 10\times$. Of course there are ways around this problem; but, given the bursts of star formation observed at high redshift (Steidel et al., 1999; Chapman et al., 2000), and detection of a population of ULIRG's with very large look-back times (Clements, 1999; Dey et al., 1999), one might conclude that the global star formation history of the Universe has been anything but uniform.

In recent years this question motivated some authors to investigate the star formation density up to large redshifts. Madau et al. (1996) combined observations of the high redshift Universe from the Hubble Deep Field (HDF) and the moderate redshift Universe. The moderate z data were taken from the Canada-France Redshift Survey (CFRS), in which UV luminosity densities were measured at redshifts over the range $z = 0.2-1$ (Lilly et al., 1996). Madau's paper did not actually calculate star formation history, but rather its cousin metal-ejection rate (MER):

$$\dot{\rho}_Z = \psi \int m p_{zm} \phi(m) dm, \quad (1.19)$$

where ψ is the star formation rate, $\phi(m)$ is the normalized IMF, and p_{zm} is the mass fraction of a star of mass m that is converted into metals and ejected. The integral, assuming a Salpeter IMF, is calculated to be:

$$\int m p_{zm} \phi(m) dm = 0.024, \quad (1.20)$$

making $\text{SFR} = 42 \times \text{MER}$. This method should be a reliable calculator of MER, and hence SFR, since UV flux per unit metal mass ejected in massive stars is constant for wavelengths in a range $1000\text{\AA} \leq \lambda \leq 3000\text{\AA}$ regardless of IMF chosen (Songaila et al., 1990).

Using the UV data of Lilly et al. (1996), Madau showed that star formation increases dramatically by a factor of ~ 10 up to $z \simeq 1$, and then trails off at higher redshifts. In fact for $z \leq 1$ the empirical form of the SFR density is:

$$\dot{\rho}_{\text{SFR}} \simeq (6.3 \pm 2.5) \times 10^{-2} \left(\frac{1+z}{2} \right)^{3.9} h_{50} \text{M}_{\odot} \text{yr}^{-1} \text{Mpc}^{-3}. \quad (1.21)$$

However, three years after Madau's paper, Steidel et al. (1999) published a result that differed from that of Madau et al. Measuring restframe UV light from Lyman break galaxies at high redshift ($3.8 \leq z \leq 4.5$) they found no evidence for the gradual decline in SFR that characterized Madau's plot at high redshift. Steidel's analysis has the advantage of internally correcting for dust extinction, a fact that should increase SFRs by a factor of $\sim 2 - 4$.

Fortunately this controversy does not affect our research since the matter being debated is the global SFR at *high* redshift; in contrast we are concerned with moderate redshift only in this thesis. Note that the true value is likely $\sim 2 - 4$ times higher, due to dust extinction.

However, the preceding description of star formation history is not yet definitive. Shortly after Lilly et al. (1996) published their paper, Cowie et al. (1999) reported that the UV luminosity density (indicative of SFR) did not drop dramatically between $z \simeq 1$ and the present. Rather it has declined gradually, hinting at the possibility that the peak in star formation was earlier than previously believed. Cowie et al. (1999) used a value of the local ρ_{SFR} determined by Treyer et al. (1998) of $4.33 \pm 1.43 \times 10^{-2} \text{ M}_{\odot} \text{ yr}^{-1} \text{ Mpc}^{-3}$. Lilly et al. (1996) reported observing the UV luminosity density at 2800\AA increasing as $(1+z)^{3.9}$ for $0 < z < 1$; on the other hand, Cowie et al. (1999) reported an increase in $\rho_L(2500\text{\AA})$ as being less pronounced, $(1+z)^{1.5}$. Cowie et al.'s results have since been confirmed by Wilson, et al. (2002), suggesting that this latter interpretation of global SFR in the Universe may be correct.

1.7 The Astronomical Samples

Before proceeding to the data and analysis, a discussion of the observing targets and their parent populations is warranted. The Canadian Network for Observational

Cosmology 2 (CNO2) has been used to collect 27 targets for SCUBA observations. The nature of these targets is discussed here.

1.7.1 The surveys: SSRS2, CNO1, CNO2 and SLUGS

The CNO2 field galaxy redshift survey (Yee et al., 2000) was a photometric/spectroscopic survey of faint field galaxies over 1.5 deg^2 in four different patches of the sky using the 3.6m Canada-France-Hawaii Telescope. With a limiting spectroscopic magnitude of $R_C \simeq 21.5$ and a redshift range of $z \sim 0.1 - 0.6$, the survey's purpose was to investigate galaxy evolution and clustering at moderate look-back times. The survey studied $\sim 40,000$ galaxies using five-colour photometry (I_C, R_C, V, B, U) with a limit of $R_C \simeq 23.5$ mag. Reliable redshifts have been obtained for ~ 6000 of these galaxies. The CNO2 survey builds on the experience of the CNO1 survey, which measured redshifts for a similar number of galaxies and similar redshift range (Yee et al., 1996). However, most of the CNO1 galaxies were found in fairly rich clusters; the purpose of the CNO1 survey was to measure the change in mass-to-light ratio with distance from the cluster centre. All of the targets chosen for this research are taken from the CNO2 catalogs; these targets will be described shortly.

Another survey, of some importance to this work, is the Canada-France Redshift Survey (Lilly et al., 1995). The CFRS catalogued several thousand objects brighter than $I_{AB} \sim 22.5$. With a mean redshift of $z \simeq 0.6$, the CFRS studied galaxy evolution over the redshift range $0 \leq z \leq 1$. The survey obtained spectra for 85% of target objects with very faint magnitudes, $17.5 \leq I_{AB} \leq 22.5$ (Crampton et al., 1995). The magnitude limits, redshift range and intent of the survey all make the CFRS an ideal candidate for comparisons with the CNO2 survey, and hence our own data. In fact the CFRS has been used as the basis for determining the star formation rate in the $z < 1$ Universe.

Another survey, of some importance to this thesis, is the Southern Sky Redshift Survey (SSRS2) (da Costa et al., 1998). This survey catalogued redshifts, magnitudes

and morphological classifications for ~ 5000 nearby galaxies with $m_B \leq 15.5$ in the southern and northern galactic caps. The SSRS2 will be used as a local redshift survey with which to compare CNOC2.

The final survey, which is second only to CNOC2 in its importance to this research, is the SCUBA Local Universe Galaxy Survey (SLUGS) (Dunne et al., 2000; Dunne and Eales, 2001; Dunne and Eales, 2002). SLUGS was a statistical survey of the local Universe using SCUBA at the JCMT. The purpose was to obtain $450 \mu\text{m}$ and $850 \mu\text{m}$ fluxes for a subset of galaxies selected from the IRAS Bright Galaxy Sample. These galaxies had been identified as having $60 \mu\text{m}$ fluxes $> 5.4\text{Jy}$, from which SLUGS selected 104 targets. The targets chosen for SLUGS covered a sky area of 10400 deg^2 with redshifts between $0.006 \leq z \leq 0.07$ and declinations $-10^\circ < \delta < 50^\circ$. The galaxies were also chosen so that they could fit in the SCUBA field of view. Among the 104 galaxies, 10 interacting pairs were resolved with SCUBA. SLUGS used the $850/450 \mu\text{m}$ SCUBA measurements, in conjunction with $60 \mu\text{m}$ and $100 \mu\text{m}$ fluxes from IRAS, to derive fits to galactic spectral energy distributions, from which dust temperatures and masses could be inferred. However, given the sub-mm fluxes, the SLUGS data suits the purpose of determining star formation rates just as readily. With 10/104 galaxies identified as pairs, the SLUGS data also affords a simple comparison of paired and non-paired galaxies similar to our own. The main benefit in analysing the star formation rate for the SLUGS survey is that the star formation density can be compared at different redshifts: SLUGS represents the local Universe whereas CNOC2 represents the moderate redshift Universe.

1.7.2 Properties of the Sample

Since this research is concerned with analysing star formation and interacting pairs, a detailed knowledge of pairs in the populations studied is necessary. Most of this knowledge comes from the work of Patton et al. (1997), Patton et al. (2000) and Patton et al. (2002).

Two new pair statistics were introduced— N_c , the mean number of companions per galaxy, and L_c , the luminosity in companions per galaxy. In this thesis we use the former quantity.

N_c was calculated for CNOC2 using a series of numerical weights that accounted for spectroscopic incompleteness of magnitude, colour, location, redshift and angular separation. Additional weights accounted for boundary effects, such as companions which lie near the edge of the velocity separation or near bright foreground stars. These weights were intended to provide unbiased pair information for a flux-limited survey in a specific range of absolute magnitude (in this case $18 \leq M_B \leq 21$).

In addition to these weights a criterion was established to identify pairs based on physical and dynamical separation. A distance of ($5h^{-1}\text{kpc} \leq r_{\text{pair}} \leq 20h^{-1}\text{kpc}$) and velocity difference of ($\Delta V \leq 500\text{km s}^{-1}$) were used to select pairs.

There is one final note about pair statistics. In spite of the criteria above, there is still an ambiguity in confirming *real* physical pairs. As described in Patton et al. (2000) only about half of pairs meeting the above requirements are actually undergoing physical interactions, or will ever interact. Two galaxies with a small velocity separation may in fact be simply separating in the Hubble flow at nearly identical radial velocities, and yet not undergoing gravitational interaction. The fraction of galaxies with true three-dimensional physical separations, f_{3D} , of $r < 20h^{-1}$ kpc was determined to be ($f_{3D} \simeq 0.5$). This implies that only about half of confirmed projected pairs are true physical pairs.

The techniques for determining pair statistics (the number and luminosity in pairs) were first tested upon the SSRS2. Patton et al. (2000) found that (2.26 ± 0.52)% of the ~ 5000 galaxies defined in SSRS2 were in pairs, and that $\sim 6\%$ have undergone mergers since $z = 1$. This first technique was extrapolated to the CNOC1 survey (Patton et al., 1997), where (7.1 ± 1.4)% of galaxies were found in physical pairs; from this the merger rate evolution was calculated. The merger rate evolution was consistent with a power-law function $(1+z)^m$, where m for CNOC1 galaxies was

2.8 ± 0.9 .

More recently, pair statistics have been calculated for the CNOC2 population (Patton et al., 2002). The number of companions per galaxy was found to be $N_c = 0.0321 \pm 0.0077$ at $z = 0.3$; i.e. approximately 3.2% were found in pairs. Assuming that N_c is proportional to the galaxy merger rate, the evolution of galaxy mergers was found to be $(1 + z)^{2.3 \pm 0.7}$. (Note that this evolution is estimated for redshifts $0 < z \lesssim 0.5$.)

One further note of caution, regarding these pair statistics, should be made. The value of the pair statistic is sensitive to both the physical criteria of pair selection and the choice in limits of absolute magnitude. For instance, changing the faint limit of absolute magnitude from -18 to -17 changes the value of N_c to 0.0581 ± 0.0139 . See Patton et al. (2002) for full details.

Other relevant properties of the CNOC2 sample include the luminosity density (Lin et al., 1999), which was calculated for early, intermediate, and late type galaxies, for restframe U, B, R_c bands, and for different cosmological models and redshift ranges (see table 3.2.6).

When compared to previous surveys of pairs and merger rates the work of Patton et al. (2002) is fairly consistent, when discrepancies like spectroscopic incompleteness are taken into account. However, any comparisons to other studies should be made with caution since Patton et al.(2002) represents the most comprehensive attempt to date to account for various selection effects in pair statistics.

Table 1.2: CNOC2 properties of our 27 targets

Name ^a	redshift	RA ^b	Dec. ^b	M_B^c	r_p^d	ΔV^e
0223-131533	0.40455	2 25 26.4	+00 21 44.33	-20.01	6.2	273
-131534				-19.84		
0223-030307	0.29794	2 25 49.17	+00 30 31.33	-18.98	5.7	162
-030309				-18.16		
0223-140119	0.26731	2 25 35.4	+00 7 17.83	-18.86	12.1	76
-140109				-18.27		
0223-031099	0.40707	2 25 48.97	+00 33 59.33	-19.69	10.6	264
-031118				-18.39		
0223-040997	0.39868	2 26 17.34	+00 41 13.83	-19.22	6.8	62
-040989				-19.22		
0920-101993	0.10760	9 24 21.44	+36 53 38.5	-19.42	9.3	252
-101995				-19.08		
0920-010722	0.19087	9 24 3.24	+37 4 47.5	-20.18	17.6	423
-010688				-17.94		
0920-081315	0.24586	9 24 39.56	+37 8 16	-19.82	5.2	284
-081301				-17.49		
0920-131238	0.39028	9 23 12.57	+37 7 4.51	-20.17	5.5	50
-131230				-18.76		
0920-020557	0.32464	9 23 30.73	+37 11 19	-19.52	6.9	29
-020566				-19.10		
0920-160826	0.39254	9 22 27.91	+36 46 52.01	-19.49	8.0	198
-160832				-19.16		
0920-191850	0.44082	9 21 6.95	+36 41 13.5	-19.65	15.9	10
-191890				-18.99		
1447-051065	0.34895	14 49 55.07	+9 38 42.89	-19.42	5.5	138
-051056				-19.06		
1447-082155	0.36381	14 50 5.93	+9 11 54.39	-19.91	15.0	171

Table 1.2: CNOC2 properties of our 27 targets

Name ^a	redshift	RA ^b	Dec. ^b	M_B^c	r_p^d	ΔV^e
-082172				-19.12		
1447-091998	0.32478	14 50 9.87	+9 4 35.39	-19.28	11.0	41
-091999				-18.97		
1447-040704	0.51035	14 49 38.87	+9 29 30.39	-19.49	13.6	44
-040709				-18.81		
2148-070450	0.15495	21 51 11.46	-4 47 58.64	-16.97	19.2	249
-070479				-20.57		
2148-071349	0.40806	21 51 21.96	-4 45 15.64	-19.69	15.5	143
-071332				-18.40		
2148-051898	0.29727	21 51 26.05	-4 58 20.14	-17.50	19.5	42
-051930				-18.77		
2148-162261	0.50600	21 50 16.54	-5 45 45.64	-19.43	7.4	125
-162264				-18.79		
0223-130503	0.56887	2 26 36.74	+00 00 7.83	-20.19	-	-
0223-100265	0.61417	2 25 10	+00 17 9.83	-20.00	-	-
0223-180416	0.59001	2 24 24.27	-00 8 12.17	-20.42	-	-
0920-162288	0.59536	9 22 25.82	+36 51 27	-20.21	-	-
0920-171094	0.62565	9 22 27.62	+36 38 46	-19.99	-	-
2148-141128	0.44663	21 50 42.04	-05 41 9.64	-20.74	-	-
2148-170710	0.62317	21 49 51.2	-5 59 3.64	-20.78	-	-

^a CNOC2 Catalog name for both companions.

^b Values signify the mean coordinate for the pair.

^c Absolute B magnitude ($H_0 = 100 \text{ km s}^{-1} \text{ Mpc}^{-1}$ and $q_0 = 0.1$).

^d Physical distance of separation in h^{-1} kpc.

^e Observed radial velocity difference between pairs in km s^{-1} .

Included are some representative sample pictures of interacting pairs used in this thesis. These pictures were snapshots taken with the Hubble Space Telescope (Patton et al. 2003, in preparation). Note that we could not obtain images for all 20 pairs used. Figure 1.9 shows images for 12 pairs from our sample. Pairs 34 and 68 were detected above 2.5σ .

1.8 The Program of Research

The program of research for this thesis incorporates many aspects of the literature that have been introduced in the preceding sections.

First and foremost, this thesis discusses $850\ \mu\text{m}$ and $450\ \mu\text{m}$ SCUBA fluxes for a set of 27 targets chosen from the CNOC2 survey. Nineteen of these targets are randomly chosen interacting pairs, as defined by Patton et al. (2002); seven targets are isolated field galaxies chosen from among those with the highest optically-inferred star formation rates in the CNOC2 survey; and one pair is chosen because of its high star formation rate. Those galaxies chosen for their high star formation rate are used to test the hypothesis that high optical SFR implies a high far-infrared SFR. The pairs constitute the main observing sample since they are the focus of the thesis, and since they were mostly randomly chosen. Star formation rates for these pairs are inferred from SCUBA fluxes and combined with SFR's from optical/UV indicators. These SFR's are used to calculate a star formation density in pairs at redshift $\simeq 0.35$.

For the high SFR field galaxies we might expect that they will have high FIR star formation since FIR indicators usually exceed optical/UV indicators by a factor of ~ 3 . Conversely, the pairs, in general, do not have high optical/UV SFR and therefore any such detections would be quite surprising.

There is yet one more goal of this thesis: to compare the star formation behaviour in pairs to the global average SFR for field galaxies at the same redshift. Ideally this is accomplished by comparing the pairs with a consistent sample of non-pairs chosen

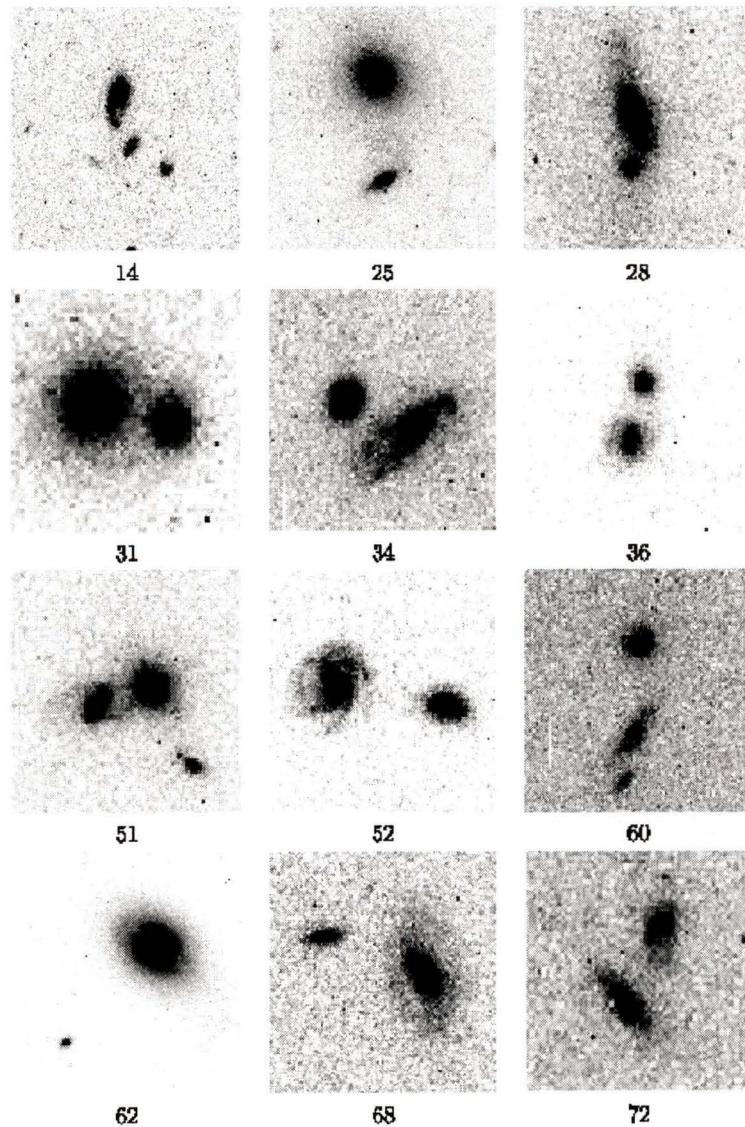


Figure 1.9: Images of 12 pairs taken with the Hubble Space Telescope. Each panel is $10'' \times 10''$ ($30h^{-1} \times 30h^{-1}$ kpc at $z=0.3$). Identification: *first row (left to right)*: pair 14 ($z=0.40707$), pair 25 ($z=0.19087$), pair 28 ($z=0.24586$); *second row (left to right)*: pair 31 ($z=0.39028$), pair 34 (detection) ($z=0.32464$), pair 36 ($z=0.392$); *third row (left to right)*: pair 51 ($z=0.34895$), pair 52 ($z=0.36381$), pair 60 ($z=0.51035$); *fourth row (left to right)*: pair 62 ($z=0.15495$), pair 68 (detection) ($z=0.40806$), pair 72 ($z=0.50600$).

objects that are less than ~ 2.3 arcmin in diameter.

- **Scan-Map:** The principle here is essentially the same as for jiggle-maps, but it is used for sources larger than the field of view.

Our targets were either pairs or field galaxies. The average angular separation between pairs is $\sim 7''$ at $z \simeq 0.3$ and they are therefore contained on a single pixel. The angular dimension of the field galaxies is smaller than the separation for pairs so they can also be contained on a single pixel. Due to the fact that our sources are all smaller than the resolution limit of a pixel they can be considered as point sources in the SCUBA array. We therefore use the photometry mode to measure fluxes for our targets.

2.1.4 Observing in Photometry Mode

Although photometry is used principally for detecting point-like sources on the central pixel, it too uses a small jiggle pattern, called nodding, of 9 points separated by about 2 arcseconds. In addition to the nodding, the JCMT mirror itself “chops” $60''$ in the azimuthal direction. One full chop comprises a full $60''$ turn to the left and back, followed by a full $60''$ turn to the right and back. The chopping allows the array to observe the sky and then subtract that value from the previous signal value. In doing so the instrument accomplishes a removal of the sky. This is especially important because the sub-mm sky varies rapidly. A full completion of the chop-nod sequence is called one integration, and the signal from each point in the 9-pt nod pattern is coadded to give a mean signal (called “one integration”). 300 integrations takes about 2 hours, implying that 1 integration is 0.4 minutes of elapsed time including overhead.

Since the sky can be particularly noisy it quite often happens that for faint sources the sky is “brighter” than the source for a given chop-nod sequence. When this happens the data records a negative value for the signal. Negative signals do not infer negative energy or flux; they are merely an artifact of the sky subtraction

algorithm and are likely to occur for sources that are barely above sky noise, if visible at all.

Additionally, since the point source falls on one pixel (usually the central pixel) the other bolometers usually fall on empty sky. Then the other bolometers can be used to determine a residual sky offset that chopping and nodding failed to remove.

The raw bolometer voltages are sampled at 128 Hz and are digitally demodulated by a transputer to give the internal calibrator signals for each jiggle position and each integration. The demodulation occurs immediately at the telescope and the demodulated data file constitutes the most basic form of SCUBA data that is saved and written to disk.

2.1.5 Observing at the JCMT

Having explained the basics of photometry observations it is worthwhile to briefly explain how the observing proceeds at the telescope.

Before arriving at the telescope a queue of observer definition files (ODF's) is constructed, composed of the pointing locations of each of the observer's objects. After one observation is done the queue searches for the next entry and the instrument automatically moves to that position. It is always possible to override queue priorities. This is often desirable in order to observe sources that are near transit, or to finish observations started on a previous night that were not finished.

Atmospheric Opacity

In principle observations can be made strictly following the queue for the entire night, and observing can be conducted from 17 00h until 9 00h the following morning. After the mid-morning the sun heats up the water vapour in the atmosphere which greatly increases the variability and reduces transmission. In practice there

are other complications. Sky opacity and seeing conditions change throughout the night; it is necessary to keep track of them in case they become incompatible with the observing regime as established by the requirements in the observer's proposal. In our case we required the most transparent skies to perform our observations, with atmospheric opacity $\tau \leq 0.08$. There are two measurements of τ that were used at the telescope. The most reliable estimate (since it is internally calibrated) is the skydip performed at JCMT in between sets of integrations. When a skydip is performed the telescope measures the sky brightness at different air masses (elevations between 15° and 80°). These sky brightness data points are then fit to a curve from which the zenith sky opacity is determined (Oliveira and Coulson, 2002). The other method of determining τ uses the Caltech Submillimeter Observatory (CSO), which also performs skydips with its high frequency heterodyne receivers to measure the atmospheric opacity, albeit at a permanently fixed azimuth. The CSO measures τ every ten minutes at 225GHz ($1332 \mu\text{m}$). The main advantage of the CSO τ is that measurements are constantly being taken throughout the night, whereas skydips can only be performed between integrations with JCMT. However, since the CSO τ measurements are made at $1332 \mu\text{m}$ they must be converted to τ_{850} . The conversion formulae are below (Archibald et al., 2000):

$$\begin{aligned}\tau_{850 \mu\text{m}} &= 4.02(\tau_{CSO} - 0.001); \\ \tau_{450 \mu\text{m}} &= 26.2(\tau_{CSO} - 0.014).\end{aligned}\tag{2.1}$$

For all of our targets the average τ was within the parameters established by our requirements ($\tau_{CSO} \leq 0.08$, $\tau_{850 \mu\text{m}} \leq 0.318$) and in many cases was much lower and well-behaved throughout the night. The average τ per target was 0.061.

Calibration

Raw signal (in volts, for example) from a source must be calibrated against some standard source with a known sub-mm flux (in Janskys¹). The primary calibrators for SCUBA measurements are Mars and Uranus. Since the brightness of these sources varies with their position and orientation with respect to the Earth, SCUBA makes use of a program that calculates their expected brightness for any given date. There are also a set of secondary calibrators to use if Mars and Uranus are unavailable at the time of observation. Calibrating the signal also provides a way to check the gain by dividing the known flux for the standard object, corrected for atmospheric extinction, by the readout signal (in Volts).

The gain is essentially the conversion factor between a raw signal in Volts and the flux density of the source. For the long wavelength (850 μm) data, the gain has been estimated as 197 ± 13 V/mJy as of March 2000. There is no appreciable variation of gain with τ , airmass or time. For the short wavelength (450 μm) data, the gain is 384 ± 82 V/mJy and it is much more dependent on dish temperature. Though these values for gain are in some sense “official,” we have employed marginally different numbers (207 V/mJy) for 850 μm in order to conform with data reduction by ORAC-DR. More will be said on this shortly.

2.1.6 Selection of Targets

The 27 targets observed in this thesis were selected on the basis of their properties, as reported in the CNOC2 catalog, and their availability for observing. The field galaxies that were observed were selected from a list of about 20 galaxies with high optical/UV SFR's. The 20 pairs were selected from a list of 72 confirmed physical pairs (Patton, 2003) from the CNOC2 catalog (Yee et al., 2000). With the exception of pair 08 those observed were chosen at random. (Pair 08 was pre-selected because

¹1 Jy = 10^{-26} W m⁻² Hz⁻¹.

it has a high star formation rate.) Once a target was selected, observations continued (sometimes on an ongoing basis) until 300 integrations were acquired.

Table 2.1: Observing conditions and dates for 19 interacting pairs.

Name ^a	Name ^b	Exp. ^c	Tau ^d	Seeing	Dates Observed
0223-030307-030309	pair 10	300	0.048	0.497	20001123, 20001124
0223-140119-140109	pair 12	60	0.070	1.190	20011024
0223-031099-031118	pair 14	275	0.040	0.158	20001123
0223-040997-040989	pair 19	320	0.05	0.755	20000126, 20020304
0920-101993-101995	pair 24	400	0.057	0.336	20020222, 20020223
0920-010722-010688	pair 25	300	0.042	0.438	20020303, 20020304
0920-081315-081301	pair 28	301	0.065	0.374	20020304
0920-131238-131230	pair 31	222	0.063	0.315	20020311
0920-020557-020566	pair 34	450	0.048	0.755	20001020, 20011022, 20011023, 20020310
0920-160826-160832	pair 36	542	0.043	0.826	20011023, 20011024, 20020303
0920-191850-191890	pair 37	150	0.09	0.46	20001020
1447-051065-051056	pair 51	300	0.063	0.530	20020306
1447-082155-082172	pair 52	300	0.043	0.435	20020310
1447-091998-091999	pair 54	302	0.046	0.593	20020310
1447-040704-040709	pair 60	300	0.052	0.363	20020311
2148-070450-070479	pair 62	280	0.053	0.613	20020301, 20020310
2148-071349-071332	pair 68	300	0.043	0.182	20001123
2148-051930-051898	pair 70	6	0.050	0.590	20001124
2148-162261-162264	pair 72	340	0.075	0.965	20001018, 20020306, 20020310

^a CNOC2 catalog name.

^b Pair identification name.

^c Exposure time in number of integrations. 300 integrations \simeq 2 hours of elapsed time.

^d Atmospheric opacity as indicated by Caltech Submillimeter Observatory (CSO).

^e All dates in Universal Time (UT).

Table 2.2: Observing conditions and dates for 1 interacting pair and 7 field galaxies. These galaxies were selected because of high optically-inferred SFR.

Name ^a	Name ^b	Exp. ^c	Tau ^d	Seeing	Dates Observed
0223-131533-131534	pair 08	290	0.064	1.066	19991219, 20011024
0223-100265	—	295	0.051	0.966	20001020, 20001124
0223-130503	—	150	0.105	0.755	20001020
0223-180416	—	50	0.035	0.205	20001125, 20001126
0920-162288	—	145	0.090	0.830	20001020
0920-171094	—	150	0.100	0.550	20001020
2148-141128	—	300	0.115	0.225	20001018
2148-170710	—	300	0.048	0.802	20001124

^a CNOC2 catalog name.

^b Pair identification name.

^c Exposure time in number of integrations. 300 integrations \simeq 2 hours of elapsed time.

^d Atmospheric opacity as indicated by Caltech Submillimeter Observatory (CSO).

^e All dates in Universal Time (UT).

2.2 Data Reduction

2.2.1 The Reduction Scheme

ORAC-DR

The first stage of reduction used the Observatory Reduction And Control software (ORAC-DR) (Economou and Jenness, 1998). This software consists of recipes of “SURF ” commands (see below) that perform the reductions in a quick and easy manner. ORAC is also the pipeline reduction software used at the JCMT to reduce data on the fly. It should be noted, however, that ORAC-DR is not meant to be the definitive reduction step, but it does provide a fast way to obtain fluxes at the telescope, and has a reputation for being quite reliable. (The reduction steps used by ORAC are similar to those described below.)

ORAC obtains all necessary information for the reduction from the header file of the desired data. Furthermore, since it is useful to compare our final fluxes with those obtained from the ORAC reduction we have adopted the gain values used by ORAC to remain consistent. ORAC uses a long wavelength gain of 207 V/mJy, and a short wavelength gain of 340 V/mJy.

SURF

To improve the quality of the reduction we have reduced the data from “first principles”, that is to say, using the basic commands of SURF (SCUBA User Reduction Facility).

The following list outlines the basic steps necessary to reduce the raw, demodulated data files from the telescope to obtain sub-mm fluxes.

1. `reduce_switch` This task subtracts the “on” position from the “off” position

that results as the telescope “chops” back and forth from the target to the sky.

2. **flatfield** Sub-mm exposures must be flatfielded in order to reduce the effect of variations in “pixel-to-pixel” sensitivity (really bolometer to bolometer), just as in optical photometry. The flatfield image is contained in the demodulated data file, and the **flatfield** command performs this function automatically.
3. **extinction** This command applies an extinction correction to the flatfielded images. The atmospheric extinction is determined by the opacity τ ; the appropriate value for τ is fed into this command depending on the image being reduced.

The preceding commands, which must be applied in the order given, constitute only the “preprocessing” phase of the reduction. Now that the images have been excised of systematic and atmospheric effects, the photometric reduction can begin.

The following is a list of the main commands used in reducing the photometric data, along with some of their parameters. Full details of **SURF** commands can be found in any of the JCMT SCUBA online documentation (Jenness and Lightfoot, 2000).

- **scuclip** This task processes each bolometer in turn and removes all signals lying outside the range specified by the user. Thus if a 3σ clip is used, the mean signal on each bolometer is calculated and any data point with signal greater than the mean ± 3 standard deviations is removed. This task is performed in an iterative fashion: the mean is recalculated each time a point lies outside the range, until no more points are eliminated.
- **remsky** This task removes the sky by subtracting a constant offset from each pixel. This offset is determined as the mean signal of a group of pixels that the user defines as the sky. The user may specify which pixels in the array to use when calculating the sky noise. For example, one may choose all pixels

(except of course the central photometry pixel) —a good choice if there are no bright sources elsewhere in the field. Alternately, the user can choose the ring of pixels around the central pixel, or any other combination of pixels, for that matter. Sky removal can be accomplished in an iterative fashion too, just as for `scuclip`.

- `scuphot` This command performs the actual photometry on the image. The 9-point jiggle pattern is reduced and converted into a mean signal (in mV) for each integration.

Given that we are searching for *very* weak sources, in order to achieve the best possible reduction we experimented with several different combinations of the photometric reduction commands listed above. Most permutations of these commands should produce similar fluxes; no one procedure is expected to be vastly superior to any other, since all we are doing is rearranging the order of operations. That being stated, some permutations might differ slightly from others (because of non-linearities in the reduction procedure); by searching for those that produce consistent results we should hopefully find the most reasonable method of reductions. These are shown in table 2.2.1.

Thus seven scripts were written, each attempting a slightly different permutation of the photometric reduction.

Figure 2.1 demonstrates how 2 particular reduction procedures were compared. By plotting the signals obtained from each procedure against each other, the relative reliability of each one was determined. Procedures that were the most consistent ought to give a slope of unity, demonstrating that there is no difference between signals obtained by one method and those of another. Figure 2.2 shows that this was clearly the case for procedures 1 and 7, while 5 and 4 (Figure 2.1) show considerable scatter in their respective signals. Procedures 1, 2 and 7 each produced the most consistent signals. This came as no great surprise given that procedure 2 is merely the inverse of 1, or that 7 is simply 1 repeated.

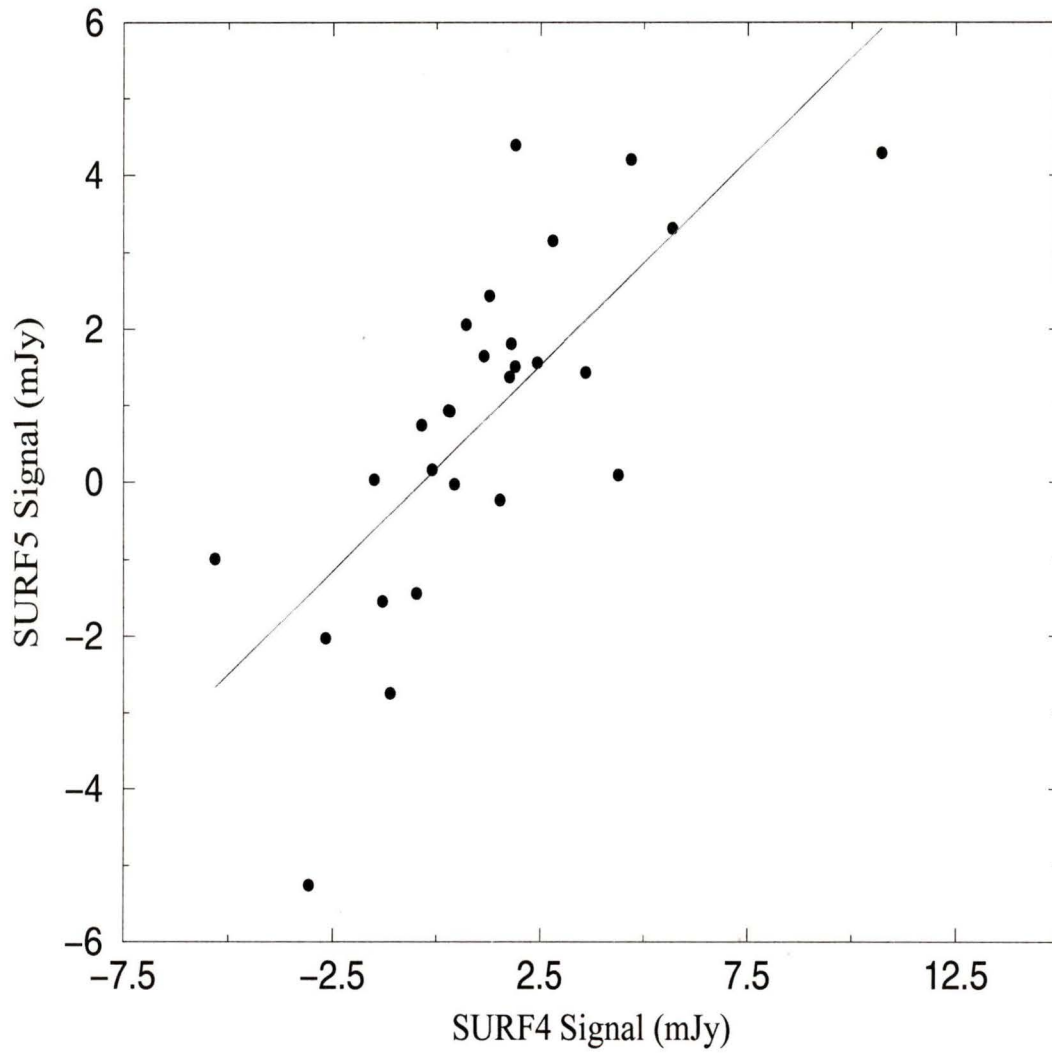


Figure 2.1: A comparison of signal obtained from 27 targets using SURF procedures 5 and 4. The correlation is very low for these two recipes.

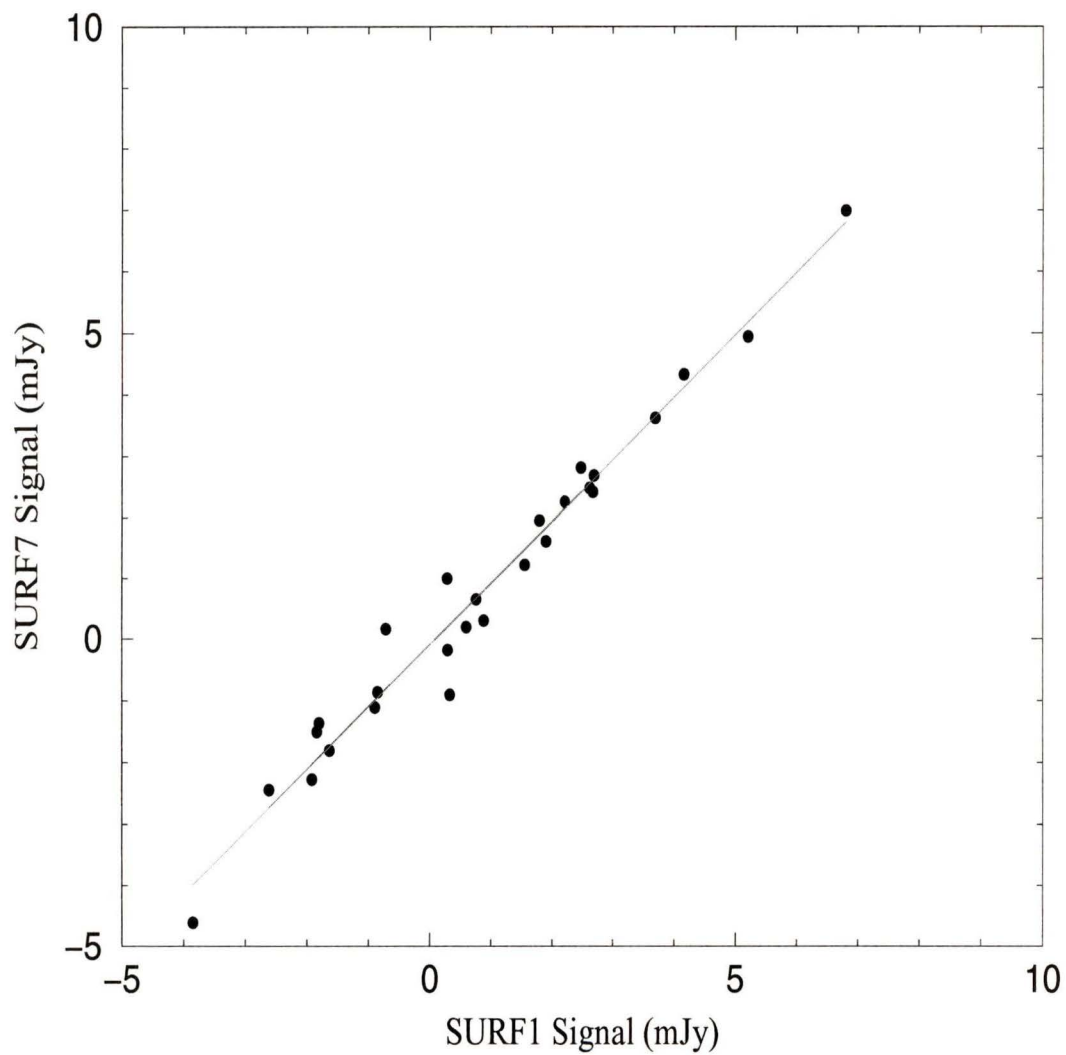


Figure 2.2: On the left a comparison of signal obtained from 27 targets using SURF procedures 1 and 7 with line of best fit having a slope of 1.012 and an rms 1σ scatter about the line of parity of 0.084

Table 2.3: Order of data reduction operations for the seven reduction attempts. Note that procedure 7 is actually five operations.

Name	1 st operation	2 nd operation	3 rd operation
photproc1	scuclip (3σ)	remsky	scuphot
photproc2	remsky	scuclip (3σ)	scuphot
photproc3	remsky (1 st ring only)	scuclip (3σ)	scuphot
photproc4	scuclip (3σ)	remsky (1 st ring only)	scuphot
photproc5	scuclip (2.5σ)	remsky	scuphot
photproc6	scuclip (3σ)	remsky (iterative)	scuphot
photproc7	scuclip (3σ)+ remsky	scuclip (3σ)+ remsky	scuphot

To further discriminate between the relative consistency of procedures 1, 2 and 7 we subtracted from each plot the so-called line of parity and determined the root-mean-square scatter about that line. (The line of parity is simply the line with slope of unity corresponding to perfect correlation between procedures.) The smallest scatter existed between procedure 1 and 7.

We also investigated whether, by repeating the operations in procedure 1 several times, we could improve the data quality. (Recall that procedure 7 repeats 1 once.) Although the rms scatter decreased slightly the improvement in signal-to-noise that was achieved was minimal.

The best reduction technique should be the one that is the simplest to perform and that introduces the least amount of error. Procedure 1 is the simplest procedure and shows the most consistency with another procedure (number 7). Therefore it was chosen to reduce our data.

Perfecting the technique

Having settled on the most basic and reliable reduction algorithm, we added one more level of sophistication before determining the fluxes. To further reduce the noise we introduced an algorithm to take into account variations in the Earth's atmosphere that would have occurred during our observations.

The un-coadded data is a series of signal values in voltage, one for each integration or observation. On average there were 267 integrations per target. Here we explain how a mean signal for a set of integrations is normally calculated, and with a special technique that we applied.

Ordinarily to obtain a mean total signal the average of those integrations is calculated

$$\bar{F} = \frac{1}{N} \sum F_i, \quad (2.2)$$

where F_i are the individual signal measurements for *each integration* and N is the total number of integrations. The uncertainty in the signal is taken to be the standard deviation, σ , divided by \sqrt{N} ,

$$\text{Error} = \frac{\sigma}{\sqrt{N}}. \quad (2.3)$$

However, throughout the integrations the sky conditions were constantly changing, with the beam being perturbed by turbulent cells in the upper atmosphere. These cells have a time scale of several minutes before they disperse, so we divided the series of signals into groups of 10. (Ten integrations correspond roughly to four minutes of elapsed time.) Now, instead of a series of N integrations (where $N \simeq 270$) there were $N/10$ groups of n integrations (where $n = 10$, unless there was a remainder $5 \leq n \leq 10$). Groups with < 5 remaining integrations were discarded. The mean and

error in the mean (standard deviation divided by $\sqrt{10}$) were calculated as follows:

$$\begin{aligned}\bar{x}_g &= \frac{1}{n} \sum_{i=1}^{n \leq 10} x_i, \\ \sigma_g^2 &= \frac{1}{n-1} \sum_{i=1}^{n \leq 10} (x_i - \bar{x}_g)^2.\end{aligned}\tag{2.4}$$

With ~ 27 mean signals (from each group) and their corresponding errors, the weighted mean of those ~ 27 measurements was calculated and taken to be the total mean signal for the source,

$$\bar{F}_{\text{tot}} = \frac{\sum_{i=1}^{N/10} (\bar{x}_g / \sigma_g^2)}{\sum_{i=1}^{N/10} (1 / \sigma_g^2)}.\tag{2.5}$$

The noise was taken to be the weighted error in that mean,

$$\sigma_{\text{tot}} = \sqrt{\frac{1}{\sum_{i=1}^{N/10} (1 / \sigma_g^2)}}.\tag{2.6}$$

In this way we hoped to reduce the signal contribution from groups of 10 integrations where the atmosphere fluctuated wildly, and enhance those that were more stable. This process increased the average signal-to-noise ratio among all our sources by 6%, as well as increasing the signal-to-noise ratio of our brightest sources.

The 450 μm data

Pure Poisson noise scales as $\propto \frac{1}{\sqrt{N}}$, where N is the number of integrations. Figures 2.3 and 2.4 shows a log-log plot of noise as a function of time (number of integrations), for both long and short wavelengths. In the case of the 850 μm data the noise obeys Poisson statistics very well. The slope of the line of best fit (drawn in the figure) is -0.55 ± 0.08 , which is very close to the expected slope of -0.5 for a log-log plot. This suggests that the noise measurements are most likely due to photon noise, and not some systematic or atmospheric effect. In the case of the 450 μm data the noise is quite scattered from any best fit line, and the slope is -0.73 ± 0.27 . The

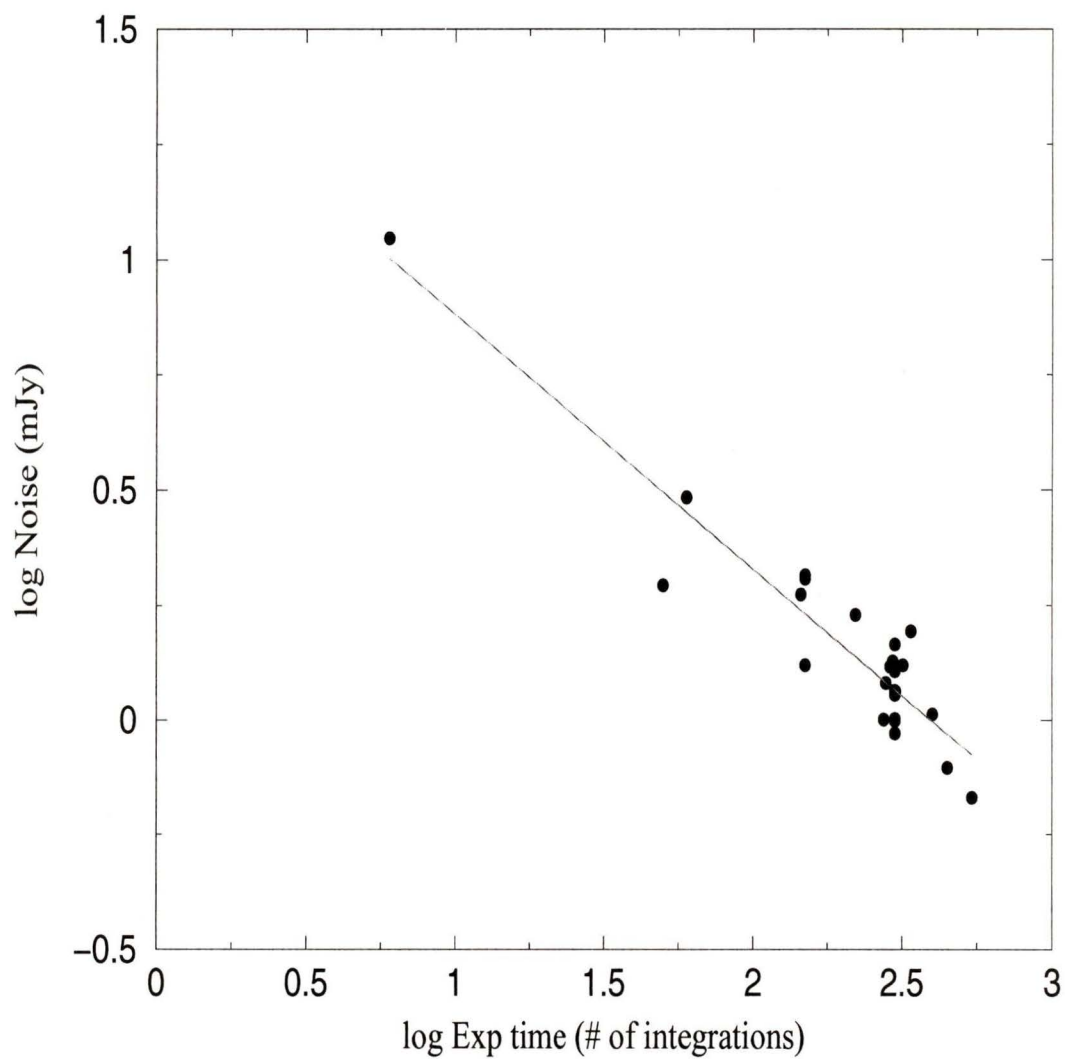


Figure 2.3: Noise vs. number of integrations for the long wavelength data. For pure Poissonian noise the slope of the line of best fit should be -0.5 . The slope for $850\ \mu\text{m}$ is -0.55 ± 0.08 , where the error represents rms scatter from the line of best fit.

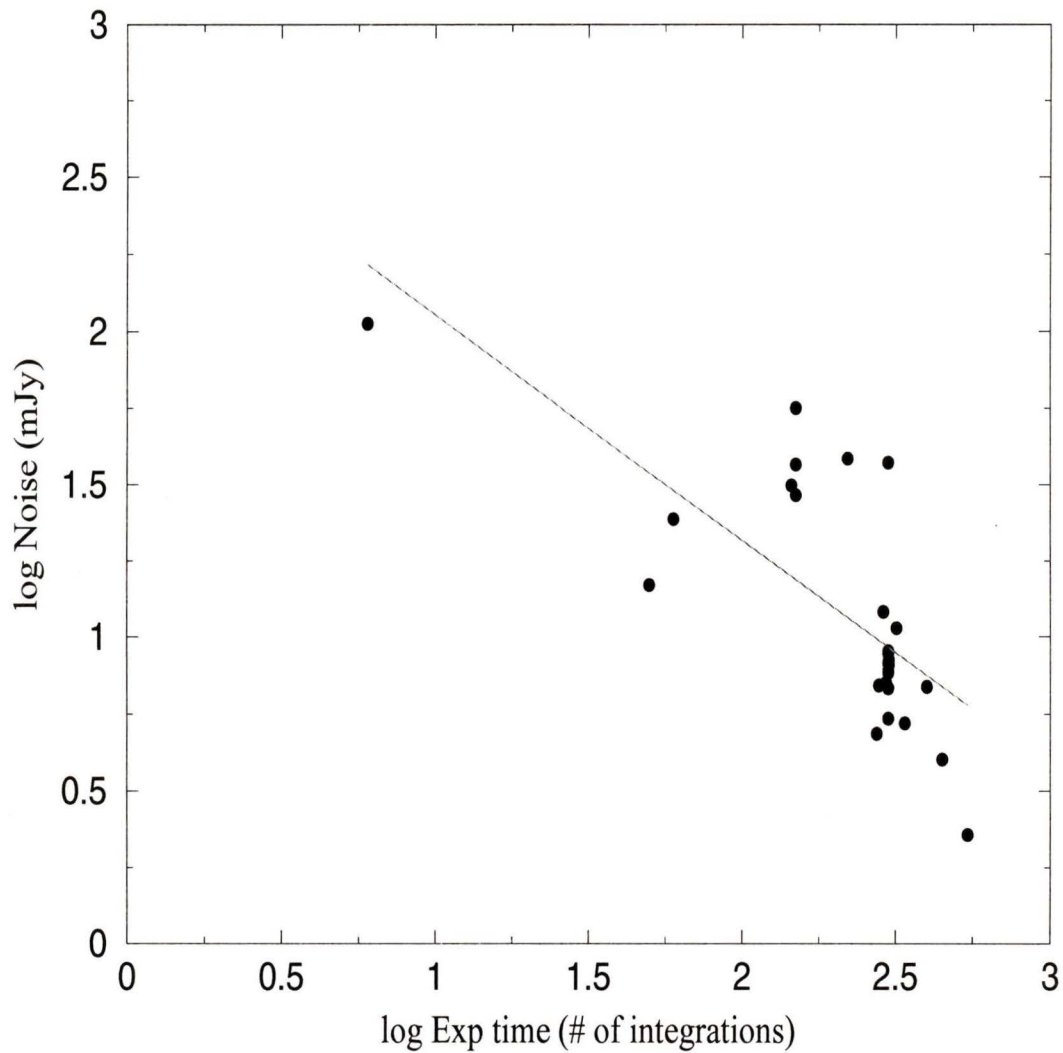


Figure 2.4: Noise vs. number of integrations for the short wavelength data. For pure Poissonian noise the slope of the line of best fit should be -0.5 . The slope on the $450\ \mu\text{m}$ plot is -0.73 ± 0.27 where the error represents rms scatter from the line of best fit.

noise is therefore not fully Poissonian. For this reason the short wavelength data was not incorporated into our analysis of star formation rates. The deviation in noise for the 450 μm data is likely attributed to atmospheric variability as well as poor transmission (see Table 1.1 for details).

2.3 Observations of Pairs

The reduced flux measurements for 27 targets are presented below. Note that target 2148-051898-051930, also known as pair 70, appears in the Table 2.4 even though it has been omitted from the analysis since it was observed for only 6 integrations.

Note also that Tables 2.4 and 2.5 presents only those measurements taken at 850 μm . We have neglected the 450 μm data because of greater sky variability at that wavelength.

Table 2.4: Fluxes for 19 interacting pairs.

Name ^a	Name ^b	Exp. ^c	Flux ^d	Noise ^d	S/N ^e
0223-030307-030309	pair 10	300	0.32	0.94	0.34
0223-140119-140109	pair 12	60	5.20	3.05	1.71
0223-031099-031118	pair 14	275	-0.90	1.00	-0.90
0223-040997-040989	pair 19	320	2.62	1.32	1.99
0920-101993-101995	pair 24	400	2.67	1.03	2.59
0920-010722-010688	pair 25	300	0.29	1.00	0.29
0920-081315-081301	pair 28	301	-1.84	1.32	-1.40
0920-131238-131230	pair 31	222	-2.62	1.70	-1.54
0920-020557-020566	pair 34	450	2.21	0.79	2.81
0920-160826-160832	pair 36	542	0.29	0.68	0.42
0920-191850-191890	pair 37	150	1.79	2.07	0.86
1447-051065-051056	pair 51	300	0.88	1.28	0.69
1447-082155-082172	pair 52	300	-1.64	1.14	-1.44
1447-091998-091999	pair 54	302	-1.92	1.16	-1.66
1447-040704-040709	pair 60	300	2.69	1.01	2.67
2148-070450-070479	pair 62	280	-1.81	1.21	-1.50
2148-071349-071332	pair 68	300	3.69	0.94	3.94
2148-051930-051898	pair 70	6	6.79	11.1	0.61
2148-162261-162264	pair 72	340	-3.86	1.56	-2.46

^a CNOC2 catalog name.

^b Pair identification name.

^c Exposure time in number of integrations. 300 integrations \simeq 2 hours of elapsed time.

^d Units in milli-Janskys (where 1 mJy = 10^{-3} Jy = 10^{-29} W m⁻² Hz⁻¹).

^e Signal-to-Noise ratio.

Table 2.5: Fluxes for 1 interacting pair and 7 high star formation field galaxies.

Name ^a	Name ^b	Exp. ^c	Flux ^d	Noise ^d	S/N ^e
0223-131533-131534	pair 08	290	4.15	1.31	3.17
0223-100265	—	295	-0.85	1.34	-0.64
0223-130503	—	150	1.55	1.32	1.17
0223-180416	—	50	-0.72	1.97	-0.37
0920-162288	—	145	0.59	1.88	0.31
0920-171094	—	150	1.90	2.03	0.93
2148-141128	—	300	2.48	1.46	1.69
2148-170710	—	300	0.75	1.16	0.65

^a CNOC2 catalog name.

^b Pair identification name.

^c Exposure time in number of integrations. 300 integrations \simeq 2 hours of elapsed time.

^d Units in milli-Janskys (where 1 mJy = 10^{-3} Jy = 10^{-29} W m⁻² Hz⁻¹).

^e Signal-to-Noise ratio.

2.4 Reduction and Observations of Serendipitous Sources

After the fluxes from the central pair/field galaxies had been analysed, the fields were then searched for other CNOC2 galaxies. This presented several challenges. First, as previously mentioned, only 30% of the array area is sensitive to radiation. Thus any sources found serendipitously (so-called serendipitous sources) had a 70% chance of being missed by all bolometers at a given time. Second, the telescope is mounted in an altitude-azimuth coordinate frame, incurring rotation of the field of view about the central pixel (see figure 2.5). (Obviously, this poses no problem for the central pairs, since the telescope was tracked so that these targets were always located on the central pixel.) The fact that the SCUBA instrument is located at the Nasmyth focus introduces a further complication. Finding serendipitous sources in the field meant taking into account the field rotation, an angle that varies both with the declination and the hour angle.

2.4.1 Finding CNOC2 Galaxies

Before accounting for rotation and deadspace, a list of CNOC2 galaxies in each of the 27 fields was determined. The CNOC2 survey observed four patches of the sky, with total area 5433.5 arcmin^2 (Yee et al., 2000). In the catalog there were 6177 galaxies with definitive redshifts, resulting in 3.158×10^{-4} CNOC2 galaxies per square arcsecond. The SCUBA field has a radius of approximately $69''$ (this radius being the radius of a circle inscribed *within* the hexagonal arrangement of bolometers), giving a total sky area of 16492 arcsec^2 . Thus the number of CNOC2 galaxies one would expect to find in any given field was ~ 5 . In running our galaxy selection code, a square area equal to $\sim 28000 \text{ arcsec}^2$ was extracted for computational ease; this resulted in 8.4 galaxies/field. However, when the search area is scaled down to represent the correct hexagonal area, ($\times 16500/28000$), we found an average of 4.9

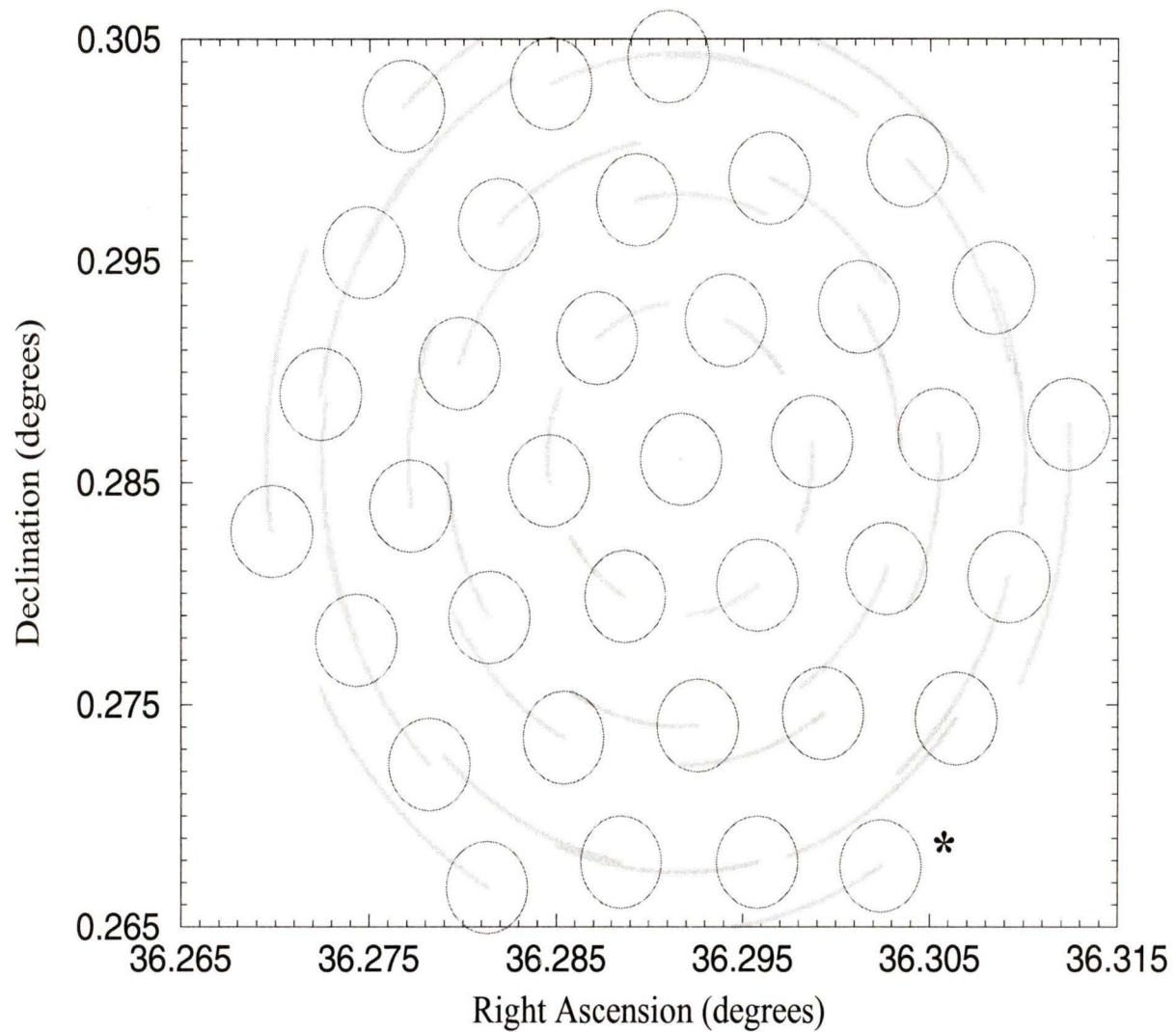


Figure 2.5: The rotation of individual bolometers about the central pixel is shown. The circles represent the beamwidths of each bolometer (half-power sensitivity) at the first integration of observation. The central pixel is pointed to target 0223-130503. This exposure represents 150 integrations (one hour) started at hour angle 2h 25 m 9.6 s. The star in the lower right identifies the bolometer 1 (G1).

galaxies per field. The agreement between the prediction and our code confirmed that we had indeed retrieved the galaxies that were in our fields. Note also that these numbers include the central object (pair/field galaxy), since by definition of the pair sample, they too are included in the CNOC2 redshift sample. When these are removed, there are ~ 4 serendipitous galaxies per field.

2.4.2 Bolometer Positions

The next step was to determine the positions of each bolometer at each integration step in each field. The SURF command `extract_data` was used; this command outputs the position of the bolometer offset relative to the central pixel in radians. Since the values for offset RA are given in the sky coordinates, they must be divided by a factor $\cos \delta$ so they can be scaled to absolute RA. Ultimately we wish to match up signal values with bolometer positions for each integration. Unfortunately `extract_data` outputs offsets for all positions in the 9 point jiggle pattern, so this 9 pt pattern must be reduced to one position per integration. This was accomplished by finding the middle point in the pattern and choosing that as the appropriate average position for the bolometer during one integration.

In principle the above procedure should yield bolometer positions for each of the integrations of a given observation. However, in reality the 9 pt jiggle pattern can be distorted or truncated and in some cases the bolometer positions in certain fields had to be reduced by hand, rather than with a script. The bolometer positions were then verified to ensure that they contained the correct total number of integrations. The signal of a given bolometer and integration was then determined with the `scuphot` command, setting `allbols=yes`. This has the effect printing the signals recorded from each bolometer in the array, rather than just the central bolometer.

2.4.3 “Capturing” Serendipitous Sources

Bolometer position and signal were now known for every integration of every field. The next task was to “follow” a given source in the field as it traced out an arc-like path (relative to the central pixel—see figure 2.5) and collect only the signal values for the bolometers it crossed over.

The first step prior to capturing the source fluxes as they cross bolometers is to properly instruct the reduction code as to the bolometer beam shape on the sky. The bolometer’s beamwidth is 13" in diameter, so any source passing within a radial distance d of 13"/2 will be seen by that bolometer. However, one must be careful in ascribing radial distances on the sky. In the component of RA direction a correction factor of $\frac{1}{\cos \delta}$ must be applied. For a bolometer centred at sky coordinates (α, δ) , where α is the right ascension and δ the declination, and serendipitous source in the field at (α_0, δ_0) , the angular distance at which the bolometer reaches half-power sensitivity is:

$$R(\theta) = \sqrt{(d \sin \theta)^2 + \left(\cos \theta \frac{d}{\cos \delta} \right)^2}, \quad (2.7)$$

where $\theta = \tan^{-1} \left(\frac{\delta_1 - \delta_0}{\alpha_1 - \alpha_0} \right)$. This formula will correct the beam shape on the sky for RA.

Since a given source could pass over several bolometers in a night of observing, it was necessary to check all bolometers systematically, one source at a time. The most difficult aspect of this was ensuring that the right bolometer was “seeing” the right source for not only the correct number of integrations, but also in the correct order.

To verify that this was the case a code that predicted the field rotation for an alt-az Nasmyth telescope from first principles was written independently. This code used an altogether different method of searching for sources passing over bolometers. Both codes were verified to give identical results.

2.4.4 Eliminating Bad Bolometers

Throughout the reduction process it was necessary to remove those bolometers that were exceptionally noisy. In the ORAC-DR reduction this was done automatically, but using `SURF` it had to be done manually. ORAC-DR determines if a bolometer is noisier than 100 mJy; however, in writing our own scripts we are free to set our own threshold for noise. By examining the distribution of bolometers with noise we observed that the median noise for all bolometers in all target fields was 26 mJy, while the mean was 45 mJy. However, the standard deviation was large and a small, but significant, number of bolometers had noise above 100 mJy. It was also discovered that $\sim 90\%$ of bolometers had noise < 60 mJy; we chose this as our threshold and disregarded any bolometers with noise above this limit. (See Figure 2.6.)

2.4.5 Noise Analysis

Finally, to ensure that our observations of serendipitous sources were not contaminated by sky variability the noise was analysed, looking for a characteristic $\frac{1}{\sqrt{N}}$ relationship between exposure time and noise. Figure 2.7 shows this relation. The slope of the line of best fit is -0.56 ± 0.21 . The slope indicates that the noise is nearly Poissonian but there is a large scatter. Nevertheless, this confirms that we have realistic noise measurements.

2.4.6 Observations of Serendipitous Sources

After the codes were run to find serendipitous sources, and “capture” the signal values of the bolometers they passed over, the mean fluxes were calculated in the same way as described in section 2.2.1. In total there were 108 CNOC2 galaxies that were observed in our target fields and that passed over a bolometer. (Recall that, owing to the deadspace, it was possible for a source to remain completely “hidden”

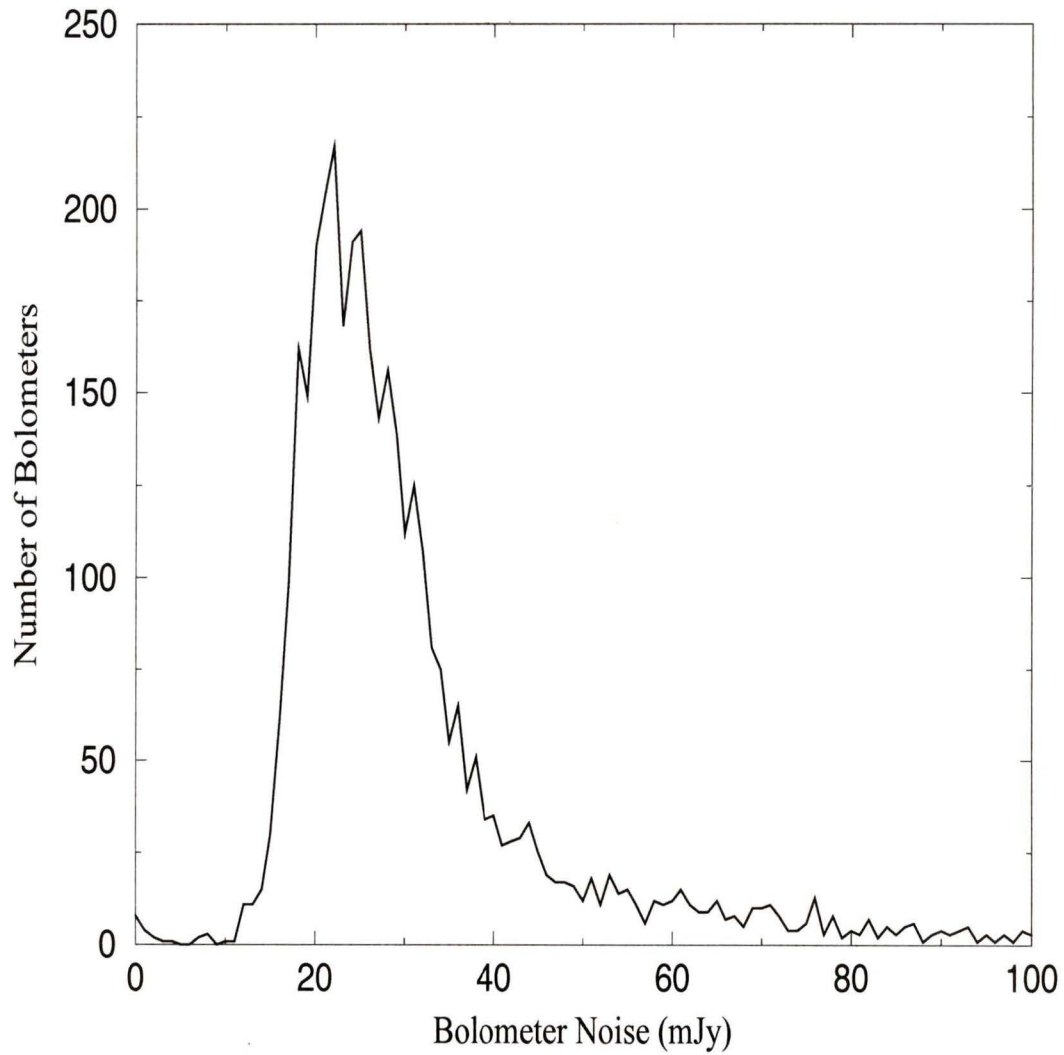


Figure 2.6: The figure above shows the number of bolometers with a given noise. Most bolometers clearly show noise levels of between 10 mJy and 50 mJy, but some extend to 100 mJy and beyond. Since $\sim 90\%$ of bolometers are never noisier than 60 mJy we have rejected all those above that threshold. The bolometer noise was determined by calculating the standard deviation in the total number of integrations for each bolometer, in each field.

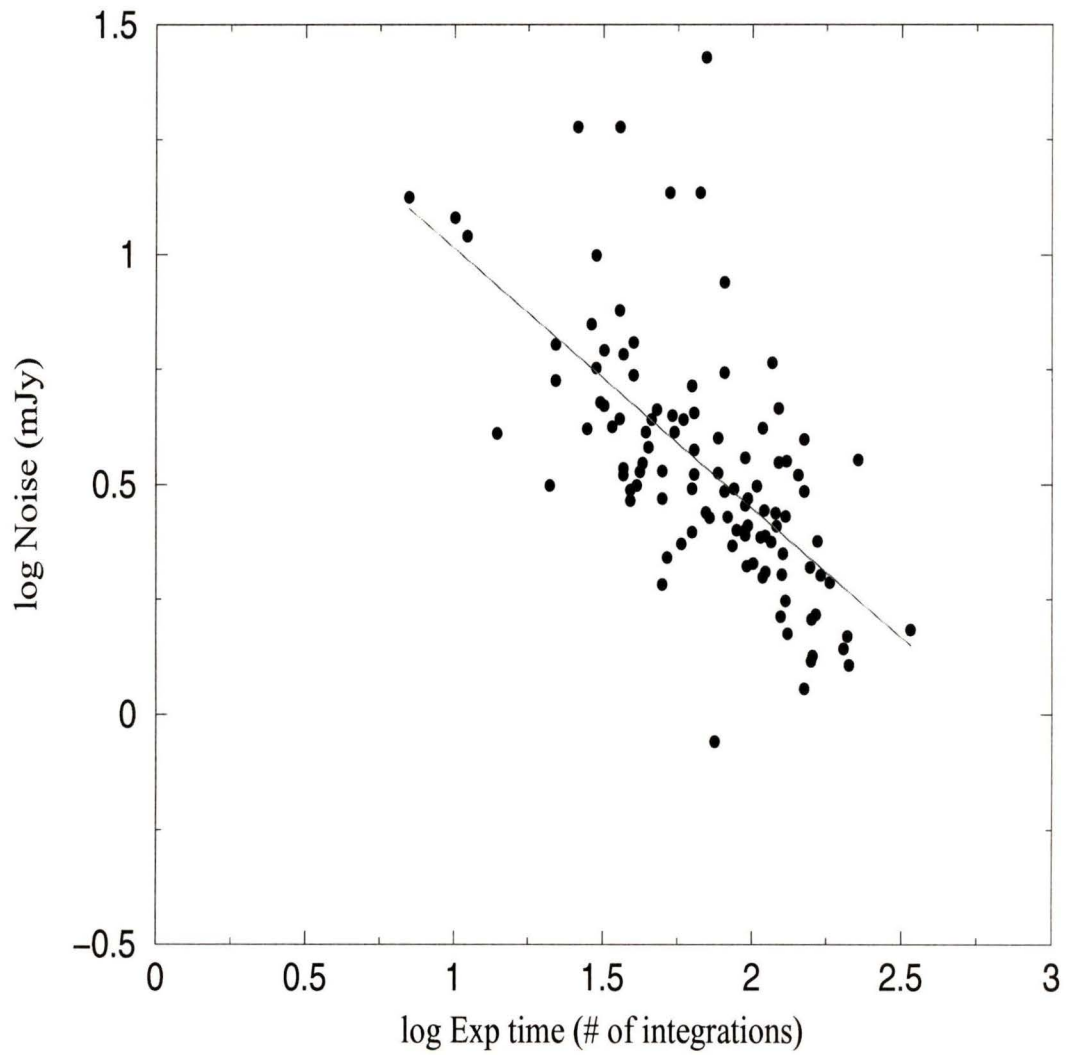


Figure 2.7: The noise is examined here with respect to exposure time for 108 serendipitous sources. The slope of the line is approximately -0.5 (-0.56 ± 0.21), the value a Poisson distribution would yield.

from bolometers.)

Unlike the pairs, for which a median of 299 integrations/target was obtained, the number of integrations for serendipitous sources varied widely. This is because only integrations while the source was over a bolometer were included in the calculation of flux. Figure 2.8 shows the distribution of serendipitous sources with integration time. The median number of integrations was 59, much lower than for pairs.

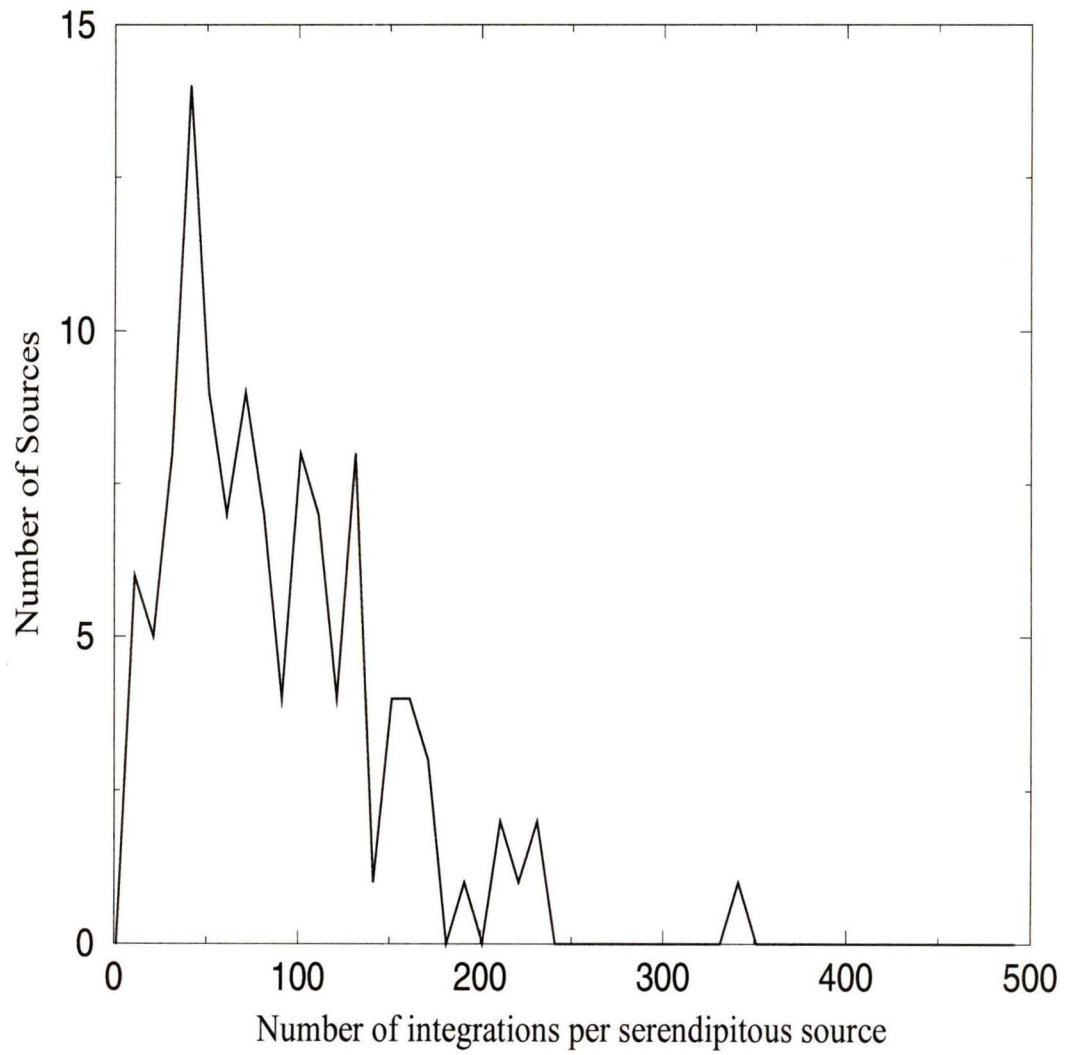


Figure 2.8: A distribution of the number of serendipitous sources with a given number of integrations. The median is 59 integrations.

Table 2.6: Fluxes for 108 serendipitous sources from the fields of our 27 original targets

Name ^a	Exp. ^b	Flux ^c	Noise ^c	S/N ^d	z	RA ^e	Dec ^e
0223-130436	170	4.41	2.01	2.19	0.36160	02:25:11.07	+00:16:53.83
0223-130495	130	3.38	2.70	1.25	0.52811	02:25:08.00	+00:17:07.83
0223-130656	121	-0.10	2.57	-0.04	0.30653	02:25:13.27	+00:17:51.83
0223-130667	48	0.94	4.59	0.20	0.35944	02:25:12.60	+00:17:54.83
0223-130707	34	-0.32	4.22	-0.08	0.35120	02:25:09.34	+00:18:04.83
0223-130708	46	-1.06	4.38	-0.24	0.35060	02:25:09.07	+00:18:04.83
0223-180072	14	-2.74	4.08	-0.67	0.28854	02:24:23.47	-00:09:24.17
0223-180770	50	3.19	1.92	1.66	0.39608	02:24:23.94	-00:07:00.17
0920-162459	97	-5.44	2.95	-1.84	0.66091	09:22:29.39	+36:51:59.00
0920-162589	37	-8.67	3.43	-2.53	0.59235	09:22:23.39	+36:52:25.00
0920-171435	45	6.53	3.82	1.71	0.24403	09:22:28.60	+36:39:34.00
0920-171472	44	5.31	4.12	1.29	0.28649	09:22:24.03	+36:39:40.00
0920-171528	55	3.64	4.12	0.88	0.28597	09:22:23.95	+36:39:48.00
2148-140867	10	6.84	12.01	0.57	0.43281	21:50:46.25	-05:42:01.64
2148-140926	120	-5.51	2.74	-2.01	0.35778	21:50:38.62	-05:41:50.64
2148-140948	40	2.40	6.44	0.37	0.44288	21:50:46.72	-05:41:45.64
2148-141057	81	3.98	3.06	1.30	0.43683	21:50:43.64	-05:41:23.64
2148-141135	157	1.71	2.09	0.82	0.33683	21:50:38.62	-05:41:06.64
2148-141154	54	-1.43	4.47	-0.32	0.39214	21:50:37.55	-05:41:03.64
2148-141158	22	1.76	6.36	0.28	0.43991	21:50:37.75	-05:41:02.64
2148-141168	89	1.06	2.52	0.42	0.43950	21:50:43.64	-05:40:58.64
2148-141170	64	3.27	3.34	0.98	0.43485	21:50:40.83	-05:40:59.64
2148-141231	104	-5.44	3.14	-1.73	0.44378	21:50:44.78	-05:40:44.64
2148-141256	59	-4.51	4.37	-1.03	0.43842	21:50:37.55	-05:40:39.64
2148-141424	107	0.76	2.43	0.31	0.44576	21:50:40.50	-05:40:03.64
2148-170459	95	-1.22	2.85	-0.43	0.15907	21:49:51.34	-06:00:16.64

Table 2.6: Fluxes for 108 serendipitous sources from the fields of our 27 original targets

Name ^a	Exp. ^b	Flux ^c	Noise ^c	S/N ^d	z	RA ^e	Dec ^e
2148-170486	97	2.04	2.58	0.79	0.15374	21:49:49.99	-06:00:07.64
2148-170565	126	-3.08	2.02	-1.53	0.25909	21:49:52.88	-05:59:42.64
2148-170801	42	2.17	3.38	0.64	0.35998	21:49:54.83	-05:58:37.64
2148-170875	95	0.11	3.61	0.03	0.06015	21:49:51.68	-05:58:18.64
2148-170963	30	1.77	9.97	0.18	0.05531	21:49:52.68	-05:57:54.64
0223-131602	127	-2.66	2.24	-1.19	0.50480	02:25:30.74	+00:22:00.83
0223-131607	164	-1.72	1.65	-1.04	0.31782	02:25:25.00	+00:22:00.83
0223-131650	37	-9.88	6.06	-1.63	0.52730	02:25:21.20	+00:22:11.83
0223-131658	87	2.82	3.10	0.91	0.52657	02:25:21.74	+00:22:14.83
0223-131666	43	-1.48	3.52	-0.42	0.58797	02:25:27.74	+00:22:15.83
0223-131679	64	-1.13	3.76	-0.30	0.42884	02:25:30.14	+00:22:19.83
0223-131723	63	2.30	3.10	0.74	0.20448	02:25:28.47	+00:22:34.83
0223-131854	36	5.47	7.57	0.72	0.42844	02:25:26.00	+00:23:07.83
0223-021752	70	-0.19	2.76	-0.07	0.41983	02:25:47.27	+00:29:12.83
0223-021797	96	-1.05	2.10	-0.50	0.36418	02:25:47.20	+00:29:23.83
0223-030217	130	-1.29	1.77	-0.73	0.22540	02:25:46.47	+00:30:06.83
0223-030333	39	-5.62	3.08	-1.82	0.29836	02:25:45.54	+00:30:34.83
0223-030382	86	4.37	2.33	1.88	0.29849	02:25:51.74	+00:30:47.83
0223-030548	21	-5.87	3.16	-1.86	0.22343	02:25:51.40	+00:31:29.83
0223-151657	7	0.85	13.30	0.06	0.21744	02:25:39.00	+00:06:32.83
0223-030977	63	1.20	2.49	0.48	0.30477	02:25:52.80	+00:33:23.83
0223-030996	52	-3.09	2.20	-1.41	0.30046	02:25:45.74	+00:33:29.83
0223-031187	75	1.39	0.87	1.59	0.39731	02:25:51.94	+00:34:13.83
0223-031406	132	1.77	1.50	1.18	0.34996	02:25:50.20	+00:35:03.83
0223-040840	22	6.62	5.31	1.25	0.24311	02:26:14.14	+00:40:36.83
0223-040842	53	15.83	13.59	1.16	0.19181	02:26:21.40	+00:40:37.83

Table 2.6: Fluxes for 108 serendipitous sources from the fields of our 27 original targets

Name ^a	Exp. ^b	Flux ^c	Noise ^c	S/N ^d	z	RA ^e	Dec ^e
0223-040966	116	-4.09	2.37	-1.72	0.26167	02:26:11.94	+00:41:05.83
0223-041044	111	0.17	2.45	0.07	0.16316	02:26:14.20	+00:41:20.83
0223-041192	166	-0.33	2.38	-0.14	0.34956	02:26:15.07	+00:41:56.83
0920-090215	227	11.70	3.58	3.27	0.24135	09:24:21.08	+36:54:56.00
0920-010500	158	-1.00	1.31	-0.77	0.19309	09:24:03.18	+37:03:53.00
0920-010605	81	-1.46	8.72	-0.17	0.37257	09:24:07.19	+37:04:20.00
0920-010669	212	-0.30	1.28	-0.23	0.19207	09:24:01.68	+37:04:39.00
0920-010808	29	0.07	7.05	0.01	0.37228	09:24:01.18	+37:05:16.00
0920-010941	40	2.19	5.45	0.40	0.23047	09:24:02.52	+37:05:60.00
0920-081061	63	1.06	5.18	0.21	0.46431	09:24:36.64	+37:07:13.00
0920-081100	123	-4.49	3.54	-1.27	0.23651	09:24:43.08	+37:07:21.00
0920-081152	131	3.75	3.55	1.05	0.24619	09:24:40.74	+37:07:34.00
0920-081345	81	0.70	5.53	0.13	0.21984	09:24:36.48	+37:08:26.00
0920-131033	183	4.81	1.94	2.49	0.11741	09:23:09.28	+37:06:12.00
0920-020409	31	9.29	4.77	1.95	0.24740	09:23:33.75	+37:10:38.00
0920-020640	160	-2.16	1.34	-1.61	0.46348	09:23:34.92	+37:11:39.00
0920-020803	150	1.13	1.14	0.99	0.32344	09:23:29.73	+37:12:24.00
0920-020840	64	-1.04	4.52	-0.23	0.32215	09:23:29.31	+37:12:35.00
0920-161004	203	-5.02	1.39	-3.61	0.46219	09:22:31.30	+36:47:25.00
0920-181707	36	-20.40	18.92	-1.08	0.46040	09:21:09.64	+36:40:04.00
0920-181881	77	-2.15	3.35	-0.64	0.56594	09:21:11.37	+36:40:32.00
0920-182420	50	-3.47	3.39	-1.02	0.11209	09:21:11.32	+36:42:01.00
0920-191455	30	-2.01	5.67	-0.35	0.44280	09:21:04.23	+36:40:05.00
0920-191730	70	-17.20	26.77	-0.64	0.18903	09:21:03.63	+36:40:48.00
1447-051075	28	5.12	4.18	1.23	0.34856	14:49:51.25	+09:38:44.39
1447-051078	209	-2.01	1.48	-1.36	0.34822	14:49:56.73	+09:38:46.39

Table 2.6: Fluxes for 108 serendipitous sources from the fields of our 27 original targets

Name ^a	Exp. ^b	Flux ^c	Noise ^c	S/N ^d	z	RA ^e	Dec ^e
1447-051337	58	2.67	2.35	1.14	0.43315	14:49:52.40	+09:39:45.39
1447-081793	143	-7.07	3.32	-2.13	0.42981	14:50:06.70	+09:10:32.39
1447-081958	32	8.36	6.19	1.35	0.36382	14:50:09.80	+09:11:07.39
1447-081984	95	2.90	2.45	1.18	0.84100	14:50:11.02	+09:11:15.39
1447-082046	11	-2.81	10.96	-0.26	0.56470	14:50:06.83	+09:11:26.39
1447-082106	26	2.90	18.94	0.15	0.66836	14:50:00.89	+09:11:39.39
1447-082395	13	-195.2	80.00	-2.44	0.30347	14:50:01.63	+09:12:43.39
1447-082457	117	0.75	5.81	0.13	0.31329	14:50:04.47	+09:12:56.39
1447-080176	109	-12.09	4.19	-2.89	0.46485	14:50:05.95	+09:05:09.39
1447-091726	77	3.24	4.00	0.81	0.24389	14:50:07.29	+09:03:33.39
1447-091793	32	-3.44	4.69	-0.73	0.53700	14:50:06.01	+09:03:46.39
1447-091824	123	-6.48	4.63	-1.40	0.22990	14:50:10.60	+09:03:53.39
1447-091887	109	-0.32	1.99	-0.16	0.64745	14:50:08.85	+09:04:11.39
1447-091916	67	-21.51	13.62	-1.58	0.64858	14:50:14.59	+09:04:19.39
1447-092058	125	3.96	1.64	2.42	0.05013	14:50:08.11	+09:04:45.39
1447-040441	95	4.19	2.52	1.66	0.46205	14:49:40.02	+09:28:23.39
1447-040497	50	-0.37	2.95	-0.13	0.40724	14:49:38.33	+09:28:35.39
1447-040507	36	-7.86	4.40	-1.79	0.37707	14:49:37.59	+09:28:39.39
1447-040580	72	-0.51	2.68	-0.19	0.40605	14:49:33.87	+09:29:00.39
1447-040610	83	-4.22	2.69	-1.57	0.40640	14:49:34.62	+09:29:08.39
1447-040728	110	1.50	2.78	0.54	0.51030	14:49:41.98	+09:29:38.39
1447-040853	159	-1.68	1.61	-1.04	0.24749	14:49:40.43	+09:30:08.39
1447-040917	41	-4.40	3.15	-1.40	0.53516	14:49:37.05	+09:30:26.39
2148-070215	150	1.47	3.96	0.37	0.31610	21:51:13.27	-04:48:45.64
2148-070222	150	4.19	3.06	1.37	0.40468	21:51:12.26	-04:48:43.64
2148-071059	37	-7.73	3.32	-2.33	0.28720	21:51:17.88	-04:46:07.64

Table 2.6: Fluxes for 108 serendipitous sources from the fields of our 27 original targets

Name ^a	Exp. ^b	Flux ^c	Noise ^c	S/N ^d	<i>z</i>	RA ^e	Dec ^e
2148-071141	101	2.85	2.13	1.34	0.12729	21:51:17.88	-04:45:54.64
2148-071366	39	3.63	2.92	1.24	0.44267	21:51:16.54	-04:45:11.64
2148-071573	111	0.27	2.04	0.13	0.28803	21:51:20.83	-04:44:37.64
2148-162095	340	4.72	1.53	3.09	0.37174	21:50:12.48	-05:46:22.64

^a CNOC2 catalog name.

^b Exposure time in number of integrations. 300 integrations \simeq 2 hours.

^c In units of milli-Janskys.

^d Signal-to-Noise ratio.

^e Right Ascension and Declination in J2000 coordinates.

Chapter 3

Results and Analysis

3.1 Analysis of the Data

Before star formation rates can be reliably constructed from the SCUBA fluxes we must be assured that the signal from our sources is real. (Recall that the $450\ \mu\text{m}$ data were rejected due to the increased variability of the sky—the noise was not purely Poissonian, as would have been expected.) There are several other tests that were performed to assess the consistency of the data.

3.1.1 The Original Targets

For the pair/field galaxy data the median signal, for all 26 targets (recall pair 70 was excluded), is 0.75 mJy, with a mean of 0.915 mJy. Approximately $\sim 65\%$ of these signals were > 0 mJy. If nothing had been detected but noise we would expect a normal distribution of fluxes, with mean of zero. The mean weighted flux for the 18 randomly selected pairs was 0.59 ± 0.26 mJy (2.23σ). This implies that there is a $\sim 97\%$ probability that positive flux was detected among pairs. The mean flux rises to 0.72 ± 0.25 mJy (2.85σ) if pair 08 is included, and to 0.74 ± 0.23 mJy (3.2σ) when

all 26 targets are included. The mean flux of the field galaxies alone is 0.82 ± 0.57 mJy. (Note that this high value is indicative of the high SFR's among field galaxies chosen.)

One additional statistical test to confirm this is the χ^2 test. Ordinarily one minimizes χ^2 to obtain a function that most closely fits the observed data. For our purposes we performed the opposite. If we had observed no flux at all (i.e. pure noise) we should expect to see a normal distribution of flux counts centered about zero mJy. We then perform a χ^2 test where our fitting function values are all equal to zero, as follows:

$$\chi^2 = \sum_{i=1}^N \left\{ \frac{1}{\sigma_i^2} [y_i - 0]^2 \right\}, \quad (3.1)$$

The quantity we use to derive probabilities is the reduced χ_ν^2 , given by:

$$\chi_\nu^2 = \frac{\chi^2}{\nu}, \quad (3.2)$$

where $\nu = N - 1$ and N is the number of data points.

For all targets (26 since we have excluded pair 70 because of its low number of integrations) a reduced chi-squared value χ_ν^2 of 3.2 was determined. This indicates that there was about a $< 0.1\%$ probability that these fluxes could be drawn from a set of null fluxes. The value of χ_ν^2 rises to 3.76 when only those 18 randomly selected pairs are included. The field galaxies alone give $\chi_\nu^2 = 1.02$, meaning that there is a 40–50% chance they *could* be drawn from a set of null fluxes. When the total χ_ν^2 probability ($< 0.1\%$) is compared to the mean flux for all 26 targets the two statistics demonstrate that there is a very good probability that real flux was detected.

The high probabilities of detection are due to the five sources (all pairs) detected above 2.5σ . Two of these sources (pair 08 and pair 68) were detected above 3σ . These detections result in ensemble averages that heavily favour non-zero flux. More will be said later on about their significance.

Table 3.1: Probabilities of detection associated with each ensemble.

Number in Ensemble	$\chi_\nu^2{}^a$	$P_\chi(\chi_\nu^2; \nu)^b$	z_{mean}	z_{med}	\bar{S}_{850}^c	σ_S^d	σ^e	$P_G(\mu; \sigma)^f$
26—pairs & field gal.	3.21	< 0.1%	0.4057	0.3925	0.74	0.23	3.2	99.8%
7—field galaxies	1.02	40–50%	0.5806	0.5806	0.82	0.57	1.4	83.8%
18—random pairs	3.76	< 0.1%	0.3638	0.3378	0.59	0.26	2.2	97.2%
19—pairs(incl.pair 08)	4.11	< 0.1%	0.3418	0.3638	0.72	0.25	2.8	99.5%

^a Reduced χ_ν^2 value (see equation 3.1).

^b χ_ν^2 probability a given ensemble could be drawn from an ensemble of null fluxes.

^c Mean 850 μm flux density, in mJy.

^d Error in the mean flux density, in mJy.

^e Signal-to-noise ratio of mean flux density.

^f Gaussian probability or confidence level that measurement is positive.

3.1.2 The Serendipitous Sources

When the analysis in section 3.1.1 is repeated for serendipitous sources, we find that the fluxes from these sources are statistically indistinguishable from a distribution of null fluxes. This result is also consistent with the average flux of 0.075 ± 0.261 mJy obtained for them. Compared with the average flux for sky-pointing bolometers of -0.047 ± 0.058 mJy it is impossible to make a distinction. Note here that the different noise values are consistent with the number of integrations that went into calculating each value. There were 8065 individual integrations that were collected from bolometers pointing at serendipitous sources, while the total number of integrations collected from sky-pointing bolometers was 199112. Since

$$\sqrt{\frac{8065}{199112}} \simeq \frac{0.058}{0.261}, \quad (3.3)$$

the noise values are consistent.

Further evidence for the indistinguishability of serendipitous sources from null-fluxes is revealed by looking at a histogram of counts over a range of flux. For a null detection we would expect a Gaussian curve with the number of integrations yielding positive and negative fluxes centered at zero.

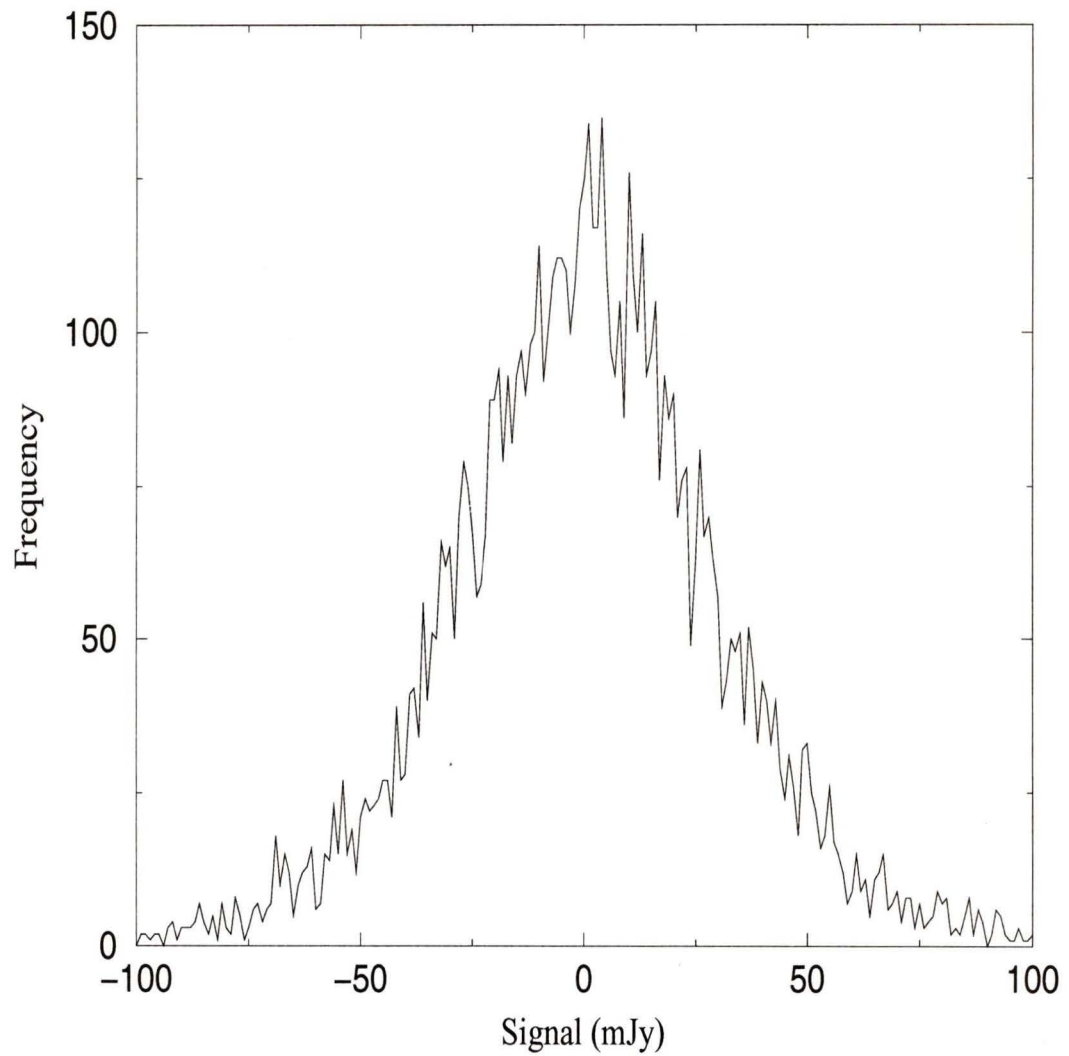


Figure 3.1: A distribution of the frequency of integrations with flux for our serendipitous sources. Note the Gaussian-like distribution of flux about zero. The median of this distribution is also exactly zero.

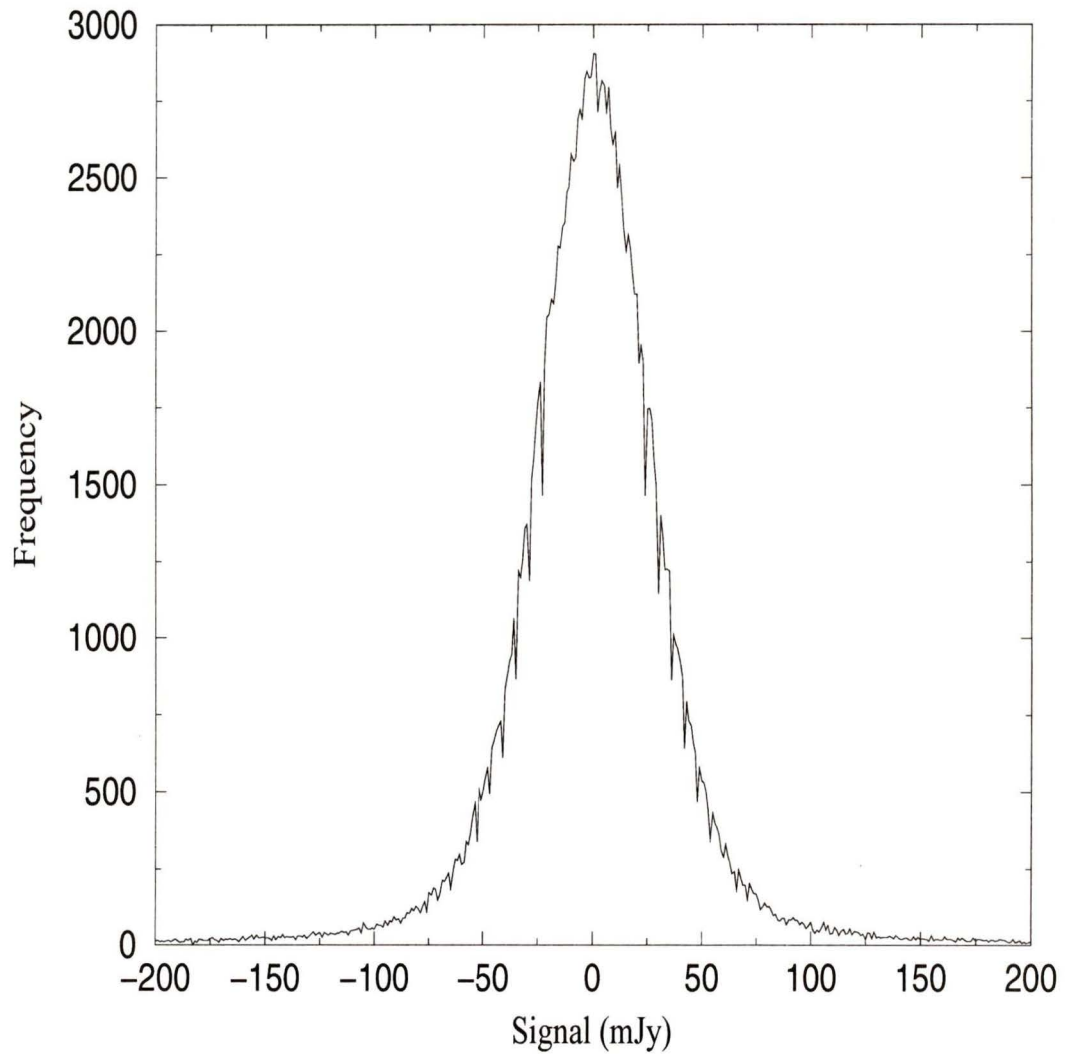


Figure 3.2: A distribution of the frequency of integrations with flux for bolometers pointing only at the sky. Note the near perfect Gaussian structure of this distribution, a fact that is reasonable considering the signals used in this histogram are just sky noise.

We might expect that those serendipitous galaxies with the highest SFR would be most likely to be detected in the sub-mm. However, if we calculate the mean signal and error for only those with $\text{SFR} > 1 M_{\odot} \text{ yr}^{-1}$ (16/97 sources) we find the mean flux is negative. Therefore, even for those galaxies expected to produce the highest S/N's there is nothing significant detected.

Since we cannot say that the serendipitous sources were detected beyond the level of sky noise with any confidence we are forced to conclude their analysis at this point. It obviously would be of little use and quite misleading to construct SFR's from their fluxes.

We can calculate a χ^2_{ν} value for our serendipitous data. The χ^2_{ν} for these galaxies is 1.74, also indicating a $> 99.9\%$ likelihood that they cannot be drawn from a set of null fluxes. This result may seem surprising considering the apparent indistinguishability of the serendipitous signals from sky noise. However, it is possible that the large value obtained for χ^2_{ν} is partly the result of a non-gaussian error distribution. This suggests that the noise associated with some of our signals (especially for those signals with extreme positive or negative values) is not poissonian. Although Figure 2.7 shows the behaviour of noise with exposure time to be roughly poissonian, there is a great deal of scatter. This large amount of scatter could be responsible for skewing the noise values associated with each signal value, such that the noise would result in a poor χ^2_{ν} fit to zero, even though the signal distribution could have a mean of zero.

3.1.3 Expected Flux

Before calculating the SFR's for our targets it is a useful exercise to determine what the expected 850 μm flux would be for a galaxy with a given star formation rate detectable in the FIR. Table 3.2 shows the 850 μm flux expected from a galaxy, at redshift $z = 0.35$ with different SFR's. Note that for 300 integrations (the mean number of integrations for our pairs) the noise is $\simeq 1.4\text{mJy}$. This implies that any galaxy with a SFR of less than $\sim 12 M_{\odot} \text{ yr}^{-1}$ would be too faint at 850 μm to register

Table 3.2: Expected sub-mm flux from a galaxy with a given SFR.

Star Formation Rate ^a	850 μm Flux ^b
1.0	0.12
2.0	0.23
3.0	0.35
4.0	0.46
5.0	0.58
10.0	1.16
12.0	1.39
15.0	1.74
20.0	2.32
25.0	2.89
30.0	3.47
40.0	4.63
50.0	5.79
75.0	8.68
100.0	11.58

^a Units of $M_{\odot} \text{ yr}^{-1}$
^b Units of mJy

a signal greater than the noise (i.e. $> 1\sigma$ detection).

3.2 Construction of Star Formation Rates

In order to arrive at star formation rates from a given flux we must first describe the physical processes involved.

3.2.1 The Grey Body Spectrum

The energy spectrum of dust is a modified blackbody—called a greybody. This characterization is a result of several factors, such as albedo (reflectivity), grain size, and shape, that lead to the deviation from the spectrum of a blackbody. The dust emissivity attenuates the energy content of the final dust spectrum, with respect to wavelength, and is parametrized as $Q \propto \lambda^{-\beta}$, where the value of β depends on the shape and size of the dust grains, as well as frequency of scattered radiation. The bolometric luminosity over the entire FIR range is:

$$L_{FIR} = \int_{8 \mu\text{m}}^{1000 \mu\text{m}} B(\lambda, T) d\lambda \times \lambda^{-\beta}. \quad (3.4)$$

Flux from a greybody is used to describe the redistribution of spectral energy that results when dust absorbs radiation and re-radiates it in the far-infrared part of the spectrum. The absorption cross-section for dust is highly peaked in the ultraviolet, making it very sensitive to the bulk of radiation emitted from young, hot stars. The radiation is absorbed and thermodynamic equilibrium with the radiation field is achieved at dust temperatures in the range 20K – 200K. In most galaxies the peak of the dust spectrum is at $80 \pm 20 \mu\text{m}$ (Kennicutt, 1998b). Because dust absorption is so sensitive to light from the most massive stars, and because these stars are so short-lived, the FIR flux provides a good indicator of the instantaneous rate at which those stars form. Although massive stars, whose peak intensities are in the UV, constitute only a small fraction of those formed (for a Salpeter IMF), they contribute the bulk of the luminosity and therefore contribute the most to the dust emission spectrum. In fact $\sim 99\%$ of the FIR radiation is thermal emission from dust grains, the remainder

coming from line emission at these wavelengths. It should be noted that an active galactic nucleus (AGN) could also be responsible for heating up dust. For an AGN (which has a $10^9 M_\odot$ black hole as its central engine) accreting $\sim 1 M_\odot \text{ yr}^{-1}$, the peak wavelength of emission will be in the UV ($\sim 100 \text{ nm}^1$), and any surrounding dust would be heated up as a consequence. Recent studies of the cosmic infrared background radiation have shown that only $\sim 10 - 20\%$ of infrared background light emanates from these sources (Elbaz et al., 2002). We therefore cannot rule out that a small but significant fraction of dust heating is caused by AGN. However, we will not pursue this heating mechanism any further.

3.2.2 Determination of Dust Temperature and β

Before star formation rates can be calculated, the values of the dust temperature and β must be reliably ascertained. We have used the temperature and β determined by Dunne et al. (2000), from the SCUBA Local Universe Galaxy Survey (SLUGS). Dunne et al. used a sample of 104 galaxies from the IRAS Bright Galaxy Sample and combined observed $850 \mu\text{m}$ fluxes with known $60 \mu\text{m}$ and $100 \mu\text{m}$ fluxes to determine best fit SED's for those galaxies. Values of $T = 35.6 \pm 4.9\text{K}$ and $\beta = 1.3 \pm 0.2$ were determined. These values were used because they represent the only systematic attempt to date to determine these parameters using SCUBA. The error in the T and β values represent one standard deviation from the mean in the set of T, β determined by Dunne et al. (2000). Presently these values are likely the best approximation for temperature and dust emissivity index, but we must still be aware of their shortcomings. First, Dunne et al.'s study focused on the local Universe, with a median redshift of $z \simeq 0.015$, whereas our targets inhabit the moderate redshift Universe ($z = 0.35$). Second, Dunne published a second paper (Dunne and Eales, 2001) in which they present $450 \mu\text{m}$ data to better constrain SED shape, temperature and β . In that paper they describe the need for a two-component temperature model—one

¹See Peacock (1999), for formulae giving peak luminosity of an accretion disk, assuming a black hole as its central engine.

component with $T \simeq 35 - 45\text{K}$, and a colder component with $T \simeq 15 - 25\text{K}$. However, we have not adopted this approach for two reasons. First, although the warm component of dust is thought to be heated by OB stars the source of heating for the cold dust component is less well-known. The cold dust is heated by the general interstellar radiation field (ISRF), but the relative contributions to that radiation from OB stars versus older stars are uncertain. Although several studies indicate that the ISRF makes a significant contribution to the total FIR flux (Bothun et al., 1989; Walterbos and Greenawalt, 1996), the amount that OB stars contribute is a matter of debate. Bothun et al. (1989) state that OB stars may be considered the dominant contributors to FIR flux in galaxies with 60 and 100 μm flux ratios $f_{60}/f_{100} \geq 0.4$. Since we do not have these fluxes for our own galaxies we cannot measure this quantity. Walterbos and Greenawalt (1996) explain that heating of the ISRF by OB stars contributes only 20% of the FIR flux (60 μm) re-emitted by the cold dust component. Thus, flux from a cold dust component will not be dominated by heating from OB stars.

Second, even if a cold dust component were to be included in our SFR models another difficulty exists. The form of the total flux for a two temperature component spectrum is:

$$S_\nu = N_w \nu^\beta B(\nu, T_w) + N_c \nu^\beta B(\nu, T_c), \quad (3.5)$$

where N_w and N_c represent the relative masses of the warm and cold temperature components, T_w and T_c . The N_c/N_w ratio was calculated in Dunne and Eales (2001) by treating this quantity as a free parameter of a spectral fitting function and minimizing χ^2_ν . We have insufficient flux data to repeat this parametrization. Nor does any average N_c/N_w value exist among galaxies. For the SLUGS galaxies used in Dunne and Eales, the N_c/N_w value varied over two orders of magnitude.

Therefore, since the responsibility for ISRF heating is still being debated, and because of insufficient data, we shall use a single temperature spectrum to model the FIR flux.

Another point of caution concerns the sample population used in SLUGS. That

survey makes no distinction between optically confirmed interacting pairs and field galaxies, though it identifies sub-mm interactions. Much more will be said on this topic later. Since we might expect star formation to be enhanced in mergers we should also expect an enhancement of the dust temperature. However, SLUGS does not differentiate between the two types of objects in deriving dust temperature. The most reliable dust temperature for our purposes would be one that is appropriate for interacting pairs, but this is currently not available. Dunne et al.’s study indicates that 10 of their 104 galaxies are “pairs”; however, their definition of a pair is based on physical and velocity separation as observed in the SCUBA mapping image. In some cases the appearance of a companion galaxy could not be confirmed with secondary IRAS images. Furthermore, there are other merging galaxies in their sample which they did not identify as pairs or mergers—e.g. NGC 4418 and Arp 220—while optically selected mergers might also exist in the sample (Dunne, 2003). Calculating the difference between dust temperature for pairs (as identified by Dunne et al.) and non-pairs reveals no significant difference. Until a comprehensive study is conducted comparing dust temperature between interacting and non-interacting galaxies, the dust temperature of Dunne et al. (2000) is the best available.

3.2.3 Physical Principles

The previous section describes the properties of the energy spectrum. We now turn our attention to extracting a star formation rate from that spectrum. Recall from section 1.4.4 the discussion of factors that allow a conversion of FIR flux into star formation rate; the most reasonable value to use was that obtained by Kennicutt (1998a) of $K = 1.72 \times 10^{-10} \text{M}_{\odot} \text{yr}^{-1} \text{L}_{\odot}^{-1}$ (There is no h dependence in this quantity).

The star formation rate is equal to the bolometric FIR luminosity, multiplied by this conversion factor:

$$\text{SFR} = K \times L_{\text{FIR}}. \quad (3.6)$$

For a greybody distribution star formation rate becomes:

$$\text{SFR} = K \times \int_{1 \mu\text{m}}^{1000 \mu\text{m}} G'(\lambda) d\lambda, \quad (3.7)$$

where the integrand is the normalized greybody distribution:

$$G'(\lambda) = k \times G(\lambda), \quad (3.8)$$

and $G(\lambda)$ is the greybody distribution:

$$G(\lambda) = \frac{2hc^2}{\lambda^5} \left(\frac{1}{e^{\frac{hc}{\lambda kT}} - 1} \right) \times \lambda^{-\beta}. \quad (3.9)$$

In practice $G(\lambda)$ is not observed; rather our observations enter into the equations through the normalization constant k that scales our distribution,

$$k = \frac{G_{obs} \left(\frac{850 \mu\text{m}}{1+z} \right)}{G \left(\frac{850 \mu\text{m}}{1+z} \right)}. \quad (3.10)$$

Flux detections are reported in the quantity G_{obs} , where G_{obs} is proportional to flux. (Strictly speaking, when we discuss flux we are referring actually to flux density, since the units of milli-Janskys are measured in $\text{W m}^{-2} \text{Hz}^{-1}$).

What is desired in our equation is not the observed flux measurement but rather the intrinsic luminosity of the source where it is emitted. Therefore G_{obs} must also include the distance travelled by radiation from source to observer:

$$G_{obs} = \frac{4\pi D_L^2}{1+z} S_\nu [\text{mJy}] \times 10^{-29}, \quad (3.11)$$

where S_ν is the measured flux density in milli-Janskys, z is the redshift of the source and D_L is the luminosity–distance given by (e.g. Mattig (1958)):

$$D_L = \frac{2c}{H_0} \left(\frac{\Omega_M z + (\Omega_M - 2) [\sqrt{1 + \Omega_M z} - 1]}{\Omega_M^2} \right), \quad (3.12)$$

where Ω_M is the density parameter of matter of the Universe, c the speed of light and H_0 the Hubble constant. In the many of cases values of $\Omega_M = 0.2$ and $H_0 = 100 \text{ km s}^{-1} \text{ Mpc}^{-1}$ were used to remain consistent with the work of Lin et al. (1999)

and Patton et al. (2000; 2002). In a $\Omega_\Lambda = 0$ Universe this also corresponds to a deceleration parameter of $q_0 = 0.1$. However $\Omega_M = 1.0$ (or $q_0 = 0.5$, if $\Omega_\Lambda = 0$) and $H_0 = 50 \text{ km s}^{-1} \text{ Mpc}^{-1}$ were also used to obtain consistency with other papers in the literature, especially Madau et al. (1996).

3.2.4 Star Formation Rates for Pairs

Star formation rates have been calculated and are presented in Table 3.3. They have been tabulated here for three different sets of cosmological parameters: $H_0 = 100 \text{ km s}^{-1} \text{ Mpc}^{-1}$, $\Omega_M = 0.2$, $\Lambda = 0$; $H_0 = 50 \text{ km s}^{-1} \text{ Mpc}^{-1}$, $\Omega_M = 1.0$, $\Lambda = 0$; and $H_0 = 100 \text{ km s}^{-1} \text{ Mpc}^{-1}$ and $\Omega_M = 0.3$, $\Lambda = 0.7$. The star formation rates in a non-zero Λ cosmology are about $\sim 40\%$ greater than without the cosmological constant. Since a non-zero, positive Λ would be expected to accelerate the expansion of the Universe our galaxies would be further away, and hence be intrinsically more luminous for a given observed flux, than if $\Lambda = 0$. It is therefore reasonable that we obtain higher star formation rates in a $\Lambda > 0$ Universe.

From the SFR's in Table 3.3 two galaxies were observed above the 3σ threshold and three sources were also detected above the 2.5σ threshold. These detections are displayed in Table 3.4.

Code Verification

Our conversion of FIR flux into star formation rate was confirmed in two ways. The first was to take SCUBA fluxes and SFR's from the literature (Scott et al., 2002), run them through our code and see if the same values were obtained. The second method involved modifying our code to determine SFR's at different infrared wavelengths for one particular galaxy with a well known SFR. This method should

Table 3.3: Star formation rates for all 20 pairs and 7 field galaxies using various cosmological models.

CNOC2 Catalog Name	SFR ^a	±	SFR ^b	±	SFR ^c	±	SFR ^d
0223-131533-131534	50.73	16.02	43.239	13.654	59.08	18.65	99.85
0223-030307-030309	2.70	7.83	2.401	6.961	3.07	8.90	2.3
0223-140119-140109	37.64	22.05	33.836	19.823	42.41	24.84	3.1
0223-031099-031118	-11.07	12.35	-9.428	10.519	-12.90	14.39	13
0223-040997-040989	31.50	15.83	26.908	13.520	36.63	18.41	57.7
0920-101993-101995	4.72	1.819	4.520	1.742	5.00	1.9	6.4
0920-010722-010688	1.29	4.44	1.194	4.120	1.41	4.87	0.33
0920-081315-081301	-11.87	8.47	-10.760	7.684	-13.28	9.48	0.42
0920-131238-131230	-30.69	19.90	-26.303	17.060	-35.64	23.11	0.028
0920-020557-020566	20.67	7.36	18.167	6.472	23.65	8.42	8.4
0920-160826-160832	3.36	7.98	2.880	6.837	3.90	9.27	20.2
0920-191850-191890	24.04	27.85	20.207	23.408	28.17	32.64	25.3
1447-051065-051056	9.01	13.09	7.844	11.401	10.37	15.07	4.54
1447-082155-082172	-17.63	12.27	-15.268	10.621	-20.37	14.17	2.1
1447-091998-091999	-17.98	10.82	-15.807	9.514	-20.57	12.38	1.0
1447-040704-040709	42.30	15.86	34.638	12.989	50.05	18.77	1.9
2148-070450-070479	-5.83	3.88	-5.482	3.654	-6.31	4.20	0.3
2148-071349-071332	45.55	11.55	38.765	9.836	53.07	13.46	6.3
2148-162261-162264	-60.15	24.40	-49.333	20.017	-71.13	28.86	23.7
0223-130503	29.13	24.86	-12.022	18.884	34.80	29.70	70
0223-100265	-15.00	23.56	22.964	19.598	-17.86	28.05	113
0223-180416	-13.10	35.75	-10.419	28.427	-15.62	42.64	93.2
0920-162288	10.823	34.42	8.589	27.316	12.91	41.06	46
0920-171094	36.41	38.95	28.580	30.575	43.53	46.57	50.6
2148-141128	33.87	19.98	28.402	16.762	39.72	23.44	203
2148-170710	56.71	92.81	11.294	17.375	17.18	26.43	130
^a $h^{-2} M_{\odot} \text{ yr}^{-1}$, $\Omega_M = 0.2$, $\Omega_{\Lambda} = 0$.							
^b $h^{-2} M_{\odot} \text{ yr}^{-1}$, $\Omega_M = 1.0$, $\Omega_{\Lambda} = 0$.							
^c $h^{-2} M_{\odot} \text{ yr}^{-1}$, $\Omega_M = 0.3$, $\Omega_{\Lambda} = 0.7$.							
^d Optically inferred SFR's. $H_0=100 \text{ km s}^{-1} \text{ Mpc}^{-1}$, $\Omega_M = 0.2$, $\Omega_{\Lambda} = 0$.							

Table 3.4: A table of sources detected above the 2.5σ level.

CNOC2 Catalog Name	Name	SFR ^a	Error ^a	S/N ^b
2148-071349-071332	pair 68	45.55	11.55	3.94σ
0223-131533-131534	pair 08	50.73	16.02	3.17σ
0920-020557-020566	pair 34	20.67	7.34	2.81σ
1447-040704-040709	pair 60	42.30	15.86	2.67σ
0920-101993-101995	pair 24	4.72	1.82	2.59σ

^a Star formation rate in $M_{\odot} \text{ yr}^{-1}$.
^b Signal-to-noise ratio.

reproduce the same SFR given flux values at different wavelengths. In both regards our code produced accurate star formation rates.

Table 3.5 gives the star formation rates estimated using our code for the measured flux of Arp 220 at various far infrared wavelengths. These results are both consistent as a set and concur with the accepted value for the star formation rate of Arp 220 of $\sim 250 M_{\odot} \text{ yr}^{-1}$ (Anantharamaiah et al., 2000; Shioya et al., 2001).

Optical Star Formation Rates

Having calculated the FIR star formation, we discuss the optical/UV SFR's in Table 3.3. These values represent the average of two different estimates. The first is a SFR derived from fitting five colour UBVRI photometry for a given galaxy to a function that describes the spectral energy distribution in that region of the spectrum. That energy is then converted into SFR with an appropriate conversion factor. This works because the restframe UV flux is proportional to SFR— e.g. section 1.4.2. The other method involves measuring the equivalent width of the [O II] emission line

Table 3.5: This table shows the SFR's obtained using our code for the starburst galaxy Arp220. The values are in general agreement with the literature. The following parameters were used: $H_0=50 \text{ km s}^{-1} \text{ Mpc}^{-1}$, $\Omega_M=1.0$, $T=42.2\text{K}$, $\beta=1.2$, $K=1.72 \times 10^{-10} M_\odot \text{ yr}^{-1} L_\odot^{-1}$.

Wavelength(μm)	Flux(mJy)	SFR(M_\odot/yr)	Flux Reference
60	103330 \pm 144	392	(a)
100	113950 \pm 207	355	(a)
350	9740 \pm 340	318	(b)
450	6286 \pm 786	405	(c)
800	825 \pm 56	278	(d)
850	832 \pm 86	336	(e)

(a) Soifer et al. (1989); (b) Benford, D.J. (1999)
(c) Dunne and Eales, (2001); (d) Rigopolou et al. (1996)
(e) Dunne et al. (2000)

at 3727Å, correcting for reddening (Lin et al., 1999) and the known rest frame B luminosity. The average of these two indicators should provide a reliable indicator of the star formation observed in the optical/UV spectrum. Unfortunately errors associated with these estimates are not yet available so only the uncertainty in the FIR estimates can be reported for now. It should however be noted that the measurement errors of the optical/UV SFR's should be lower because signal-to-noise ratios for those measurements are significantly higher than for our 850 μm fluxes. The main source of error in the optical/UV SFR's is uncertainty in the conversion factor (see equation 1.7).

Figures 3.3 and 3.4 show how star formation rate compares for the sub-mm and optical/UV measurements. The field galaxies were specifically selected because of their high optically inferred SFR, which is evident from the plot, while the pairs were selected more or less randomly (with the exception of pair 08). Ignoring for the moment those pair data with negative sub-mm SFR, several of the pairs have relatively high FIR star formation rates compared with their optically inferred rates.

The diagonal line represents the locus of points where optical/UV and sub-mm

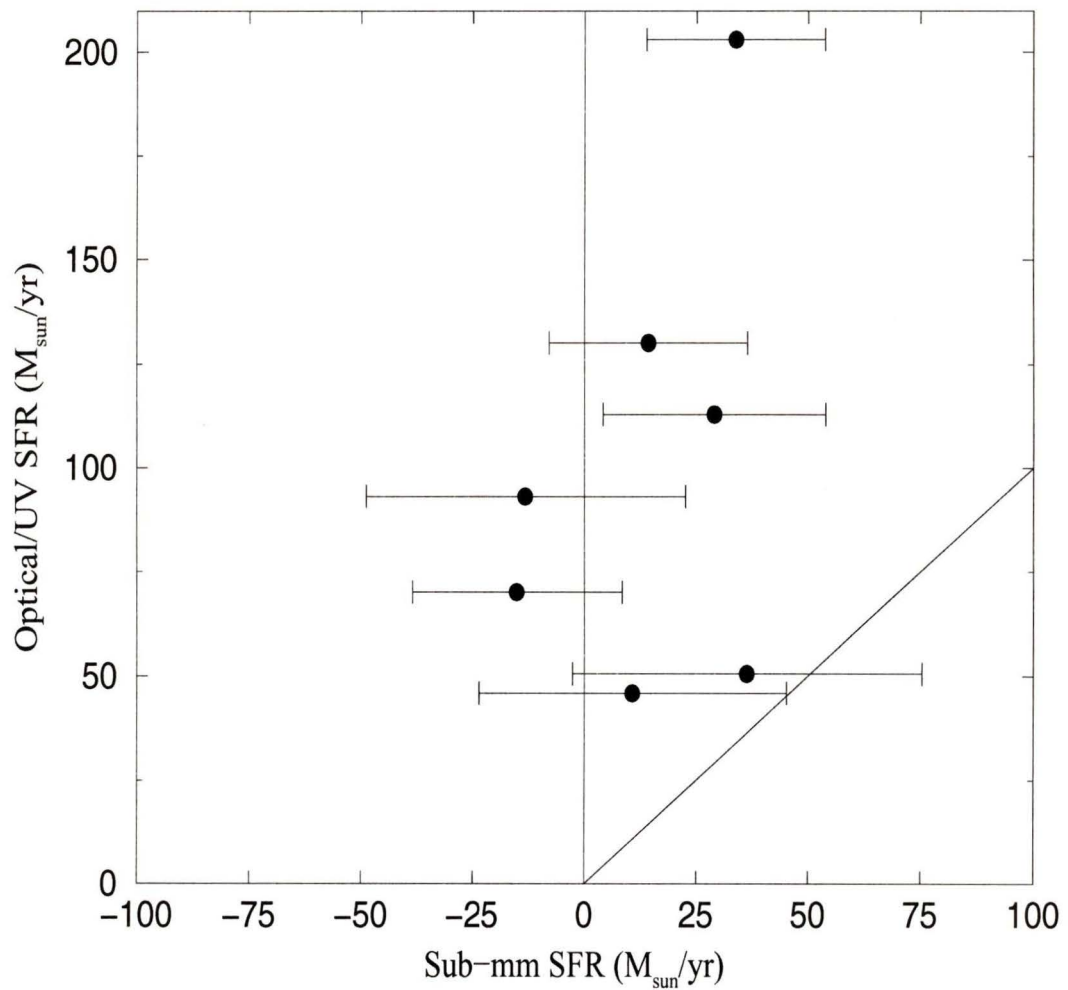


Figure 3.3: Comparison of star formation rates as inferred by FIR and optical/UV indicators for 7 field galaxies. These galaxies were selected from the CNOC2 catalog for their high optically-inferred SFR's. The diagonal line is the so-called "line of parity" where optical/UV SFR equals sub-mm SFR. ($H_0=100 \text{ km s}^{-1} \text{ Mpc}^{-1}$ and $\Omega_M=0.2, \Omega_\Lambda = 0$.)

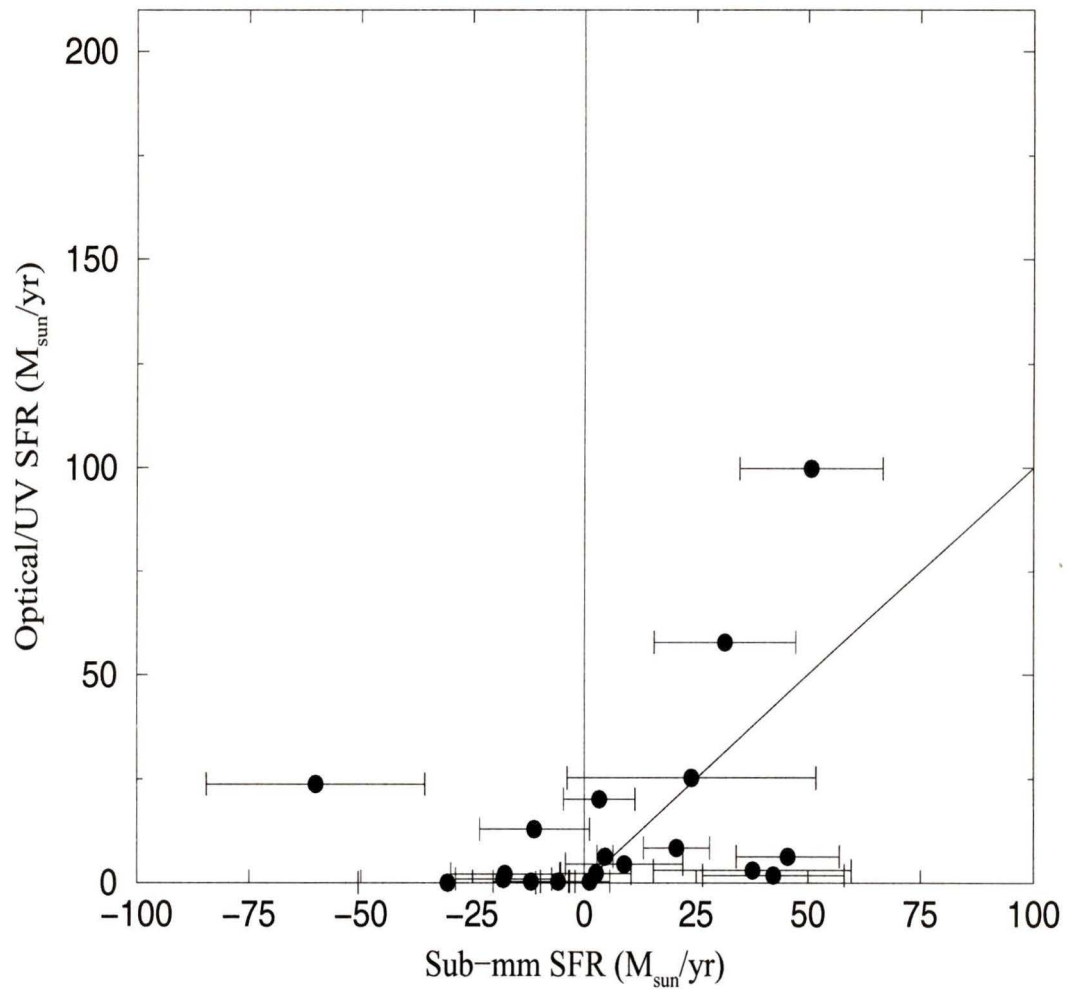


Figure 3.4: Comparison of star formation rates as inferred by FIR and optical/UV indicators for 19 interacting pairs, selected from the CNOC2 catalog. The diagonal line is the so-called “line of parity” where optical/UV SFR equals sub-mm SFR. ($H_0=100 \text{ km s}^{-1} \text{ Mpc}^{-1}$ and $\Omega_M=0.2$, $\Omega_\Lambda = 0$.)

SFR would trace each other; this line shall hereafter be referred to as the line of parity. In our case we would not expect the data to lie on this line since the signal/noise ratios are too low for most data to reliably estimate a FIR star formation rate. It is instructive to point out that ideal dusty galaxies—galaxies whose spectral energy is predominantly emitted in the FIR—should lie near to the positive x-axis, while non-dusty galaxies, those with little dust obscuration, should lie near the positive y-axis (see Figure 4.6). The fluxes for all of our 19 pairs (incl. pair 08 for now) were averaged together and a FIR star formation rate was calculated from them; we find $6.7 \pm 2.3 h^{-2} M_{\odot} \text{ yr}^{-1}$ at a median redshift of 0.3638. This value represents a mean SFR per pair, weighted by the sub-mm flux error. For the 18 pairs that were chosen randomly (i.e. excluding pair 08), the average SFR was $5.5 \pm 2.4 h^{-2} M_{\odot} \text{ yr}^{-1}$, with the same median redshift. For field galaxies the average SFR was $11.8 \pm 8.2 h^{-2} M_{\odot} \text{ yr}^{-1}$, at a median redshift of 0.59. All of these averages use the following cosmological parameters: $\Omega_M = 1.0$ and $\Omega_{\Lambda} = 0$.

It is interesting to note that the ensemble of field galaxies, chosen for their high optically-inferred SFR's, had typical S/N of ~ 0.54 (cf. a maximum S/N of 1.7) but a high average optical/UV SFR. One must ask the question: how can these galaxies, with such high optical/UV SFR's, remain so faint in the sub-mm? One possibility is that they contain relatively little dust, but sufficiently large quantities of gas to fuel high star formation. More will be said on this topic later.

3.2.5 Optical Properties of Detected Galaxies

Before analysing the aggregate star formation properties of the pairs it is instructive to examine the individual properties of those pairs detected with $S/N > 2.5\sigma$.

Table 3.6 shows various optical and physical properties of those pairs detected above the 2.5σ threshold. There appears to be no significant difference in the average colour, luminosity, redshift, projected separation or velocity difference, between the detected pairs and other ensembles of pairs: namely, our 19 pairs and the 72 identified

Table 3.6: The optical and physical properties of pairs detected above 2.5σ . The averages for the entire sample of 72 CNOC2 pairs and our subset of 19 pairs are included.

Name	$B - V$	L_B ^a	z_{med}	r ^b	ΔV	SFR ^c
pair 08	0.850	2.314	0.404	6.2	273	99.85
pair 34	0.410	1.375	0.325	6.9	29	8.4
pair 68	0.926	1.208	0.408	15.5	143	6.3
pair 24	1.130	1.415	0.107	9.3	252	6.4
pair 60	0.399	1.137	0.510	13.6	44	1.9
Average	0.743	1.490	0.351	10.3	148.2	24.6
Average ^d	0.687	1.132	0.296	12.9	151	1.05
Average ^e	0.699	1.343	0.338	10.6	151	9.83

^a Luminosity in units of $10^{10} L_{B,\odot}$.
^b Projected separation in h^{-1} kpc.
^c Optical/UV SFR (Morris, 2003; Lin and CNOC2 Collaboration, 2001) in units of $h^{-2} M_{\odot} \text{ yr}^{-1}$.
^d Average obtained from Lin 2001² among all 72 identified CNOC2 pairs (Patton, 2003).
^e Average among our 18 random pairs.

CNOC2 pairs. There is, however, a major difference in the optical/UV SFR for our pairs compared with the average for CNOC2 pairs. This difference becomes even more significant when the average optical/UV SFR for our pairs is compared to the general CNOC2 population, which has an average optical/UV SFR of $0.69 M_{\odot} \text{ yr}^{-1}$. This difference is troublesome given that any conclusions from this analysis are predicated on the randomness of our pairs as star formers. More will be said on this in the Discussion.

3.2.6 Star Formation Rate Density—Preliminaries

One of the most useful quantities that can be derived from our data is the comoving star formation rate density—a quantity that is thought to evolve significantly between $z = 1$ and the present (Madau et al., 1998; Lilly et al., 1996). Star formation densities have been calculated, as explained in the Introduction (see section 1.6, equation 1.21) for a wide range of redshifts; our star formation rates should produce values consistent with these literature values. However, since we know the overall star formation density (all galaxies) for our redshift range, we could compare ρ_{SFR} in pairs to that of the general population. Furthermore, knowing the fraction by number that pairs represent, we could compare these two numbers and determine if there is an excess of ρ_{SFR} in pairs. Given that interacting pairs might be expected to have an enhanced rate of star formation, due to mergers or galaxy “harassment” (Bushouse, 1987; Kennicutt et al., 1987), we should expect some surplus ρ_{SFR} allocated to pairs.

Before proceeding, let us gather together here some basic data that will be useful in what follows. The SFR density of the Universe (measured in the optical/UV for $0 < z \leq 1$) can be derived from Madau et al. (1998), who parametrized the data of Lilly et al. (1996) as follows:

$$\rho_{\text{SFR}} \simeq (6.3 \pm 2.5) \times 10^{-2} \left(\frac{1+z}{2} \right)^{3.9} h_{50} M_{\odot} \text{ yr}^{-1} \text{ Mpc}^{-3}, \quad (0 < z < 1). \quad (3.13)$$

²This value does not account for dust extinction and so is likely an underestimate

This implies that $\rho_{\text{SFR}} = (1.41 \pm 0.56) \times 10^{-2} h_{50} \text{ M}_{\odot} \text{ yr}^{-1} \text{ Mpc}^{-3}$ at $z = 0.36$. We now rewrite this value for a Hubble constant of $H_0 = 100 \text{ km s}^{-1} \text{ Mpc}^{-1}$:

$$\rho_{\text{SFR}} = (2.82 \pm 1.12) \times 10^{-2} h_{100} \text{ M}_{\odot} \text{ yr}^{-1} \text{ Mpc}^{-3} , \quad (3.14)$$

which is the value we will use from now on for all of our comparisons.

An alternate measurement of SFR at low z is that of Cowie et al. (1999), who found a less steep increase in the UV luminosity density with z . Cowie et al.'s estimate of ρ_{SFR} for $z = 0.36$ is $6.87 \times 10^{-2} h \text{ M}_{\odot} \text{ yr}^{-1} \text{ Mpc}^{-3}$. The issue of which estimate of ρ_{SFR} is best has not yet been settled. For the purposes of this paper we will adopt the estimate of Madau et al. ($(2.82 \pm 1.12) \times 10^{-2} h \text{ M}_{\odot} \text{ yr}^{-1} \text{ Mpc}^{-3}$), though we will compare to Cowie et al. where convenient.

Another quantity of importance is the blue light luminosity density at $z = 0.36$. This has been calculated by Lin et al. (1999) and is given in Table 3.2.6. (Note that the luminosity function calculated in Lin et al. (1999) accounts for absolute restframe magnitudes in the range $-23.5 < M_B < -17.5$.) This table presents results in both physical units ($\text{W Hz}^{-1} \text{ Mpc}^{-3}$) and in more astronomical units ($L_{B,\odot} \text{ Mpc}^{-3}$). Note that the values quoted are quite consistent with the $z = 0$ $\rho_{L,B} = 1.69 \pm 0.26 \times 10^8 h L_{B,\odot} \text{ Mpc}^{-3}$ (see note ³ below), scaled up by a factor of $(1+z)^{2.7}$ (Lilly et al., 1996).

Table 3.7: The restframe B band luminosity density, ρ_L , for the redshift range, $0.25 < z < 0.40$, and different cosmological parameters. Obtained from Lin et al. (1999)

$\Omega_M = 0.2$	$\Omega_M = 1.0$	Units
1.197 ± 0.225	1.318 ± 0.230	$10^{20} h \text{ W Hz}^{-1} \text{ Mpc}^{-3}$
3.52 ± 0.66	3.88 ± 0.67	$10^8 h L_{B,\odot} \text{ Mpc}^{-3} \text{ }^a$
$^a L_{B,\odot} = 3.4 \times 10^{11} \text{ W Hz}^{-1}$ (Lilly et al., 1996)		

First we consider a simple calculation that will not only provide an estimate for

³This value for the blue light luminosity density is taken from Madau et al. (1998) and is an average of several values for $\rho_{L,B}$ quoted therein.

the star formation density but will also illustrate the difficulty inherent in determining the ρ_{SFR} of the Universe for pairs at $z = 0.36$.

The mean SFR of our pairs was $5.5 h^{-2} M_{\odot} \text{ yr}^{-1}$. The mean luminosity of our pairs was $L_B = 1.343 \times 10^{10} h^{-2} L_{B,\odot}$. Calculating the star formation rate per unit blue light luminosity, $\frac{\dot{M}}{L_B}$ gives 4.09 (in units of $M_{\odot} \text{ yr}^{-1} 10^{-10} L_{B,\odot}^{-1}$, which will be the units we use henceforth for this quantity).

To compare with galaxies in the field we take a slightly different approach. We know from Madau et al. (1998) that the star formation rate in a volume of one cubic megaparsec, and at redshift 0.36, will be $2.82 \pm 1.12 \times 10^{-2} h M_{\odot} \text{ yr}^{-1} \text{ Mpc}^{-3}$. Furthermore we know that the restframe B luminosity density for the same co-moving volume element and at the same redshift is $3.88 \pm 0.67 \times 10^8 h L_{B,\odot}$ (Lin et al., 1999). Using $\frac{\dot{M}}{L_B}$ we find the star formation rate per unit luminosity in one cubic megaparsec at redshift 0.36 to be 0.73 ± 0.42 . This suggests that the SFR/L_B is $\sim 6\times$ greater among pairs than for field galaxies. Here we have further evidence that the pairs are atypical star formers. However, if we recalculate using Cowie et al.'s (Cowie et al., 1999) value for ρ_{SFR} per megaparsec cubed, we obtain a value of 1.78 ± 0.89 .

What is remarkable is that if we calculate the SFR/L_B for field galaxies using $\frac{\dot{M}}{L_B}$, where we compute the SFR/L_B for each galaxy with a SFR and then take the average, we get nearly the same value:

$$\left\langle \frac{\dot{M}}{L_B} \right\rangle = 0.747, \quad (3.15)$$

in our standard units of $10^{-10} M_{\odot} \text{ yr}^{-1} L_{B,\odot}^{-1}$. This allows us to say with reasonable confidence that the star formation rate per unit blue luminosity among field galaxies at $z = 0.36$ is 0.74.

Unfortunately neither of these two preceding calculation are definitive. Our pairs already have a high rate of optically inferred SFR ($\sim 10 M_{\odot} \text{ yr}^{-1}$). This last point is perhaps cause for the most concern since the average optical/UV SFR for CNOC2 galaxies is $0.69 M_{\odot} \text{ yr}^{-1}$, while a consistent optical/UV SFR for all 72 pairs (Patton

2003, in preparation) is still not known. Soon, however, more reliable optical/UV SFR's will be known for all CNOC2 galaxies, in particular the 72 identified pairs. This will give us an indication of how much the optical/UV SFR's for pairs diverge from that of the general population.

3.2.7 Star Formation Rate Density—Details

However, we can proceed and recalculate the ρ_{SFR} in a more accurate manner. We shall continue to use the mean pair luminosity and SFR, but now we use the portion of luminosity density contributed by pairs. The luminosity density of pairs is just:

$$\rho_{L,\text{pairs}} = \rho_{L,\text{tot}} \frac{L_c}{L_{fg}}, \quad (3.16)$$

where L_c is the luminosity in companions per galaxy (Patton et al., 2002), and L_{fg} is the mean luminosity of field galaxies. Note that the value for L_c computed by Patton et al. (2002) is calculated for a $\Omega_M = 0.2$ cosmology. When this value is corrected to $\Omega_M = 1.0$ and a factor of 2 is included to account for both companions in the pair, the luminosity density is:

$$\rho_{L,\text{pairs}} = 4.27 \times 10^7 h L_{B,\odot} \text{ Mpc}^{-3}. \quad (3.17)$$

This gives an estimate of the ρ_{SFR} for pairs of $0.0172 M_\odot \text{ yr}^{-1} \text{ Mpc}^{-3}$, or $\sim 60\%$ of the total ρ_{SFR} at that redshift. Again, these are just rough estimates and are susceptible to serious doubts about the extent of the pairs' contribution to luminosity density and the randomness of the pairs sample.

A more precise way of calculating the star formation rate density is with the following product:

$$\rho_{\text{SFR}} = \left\langle \frac{\dot{M}}{L} \right\rangle \rho_L, \quad (3.18)$$

where $\left\langle \frac{\dot{M}}{L} \right\rangle = \frac{1}{N} \sum_{i=1}^N \frac{\dot{M}_i}{L_i}$ is the average of the “reduced” star formation rates (neglecting weights for now), and ρ_L is the luminosity density. (By “reduced” SFR we

mean “divided by the luminosity of that same galaxy”—i.e. the reduced SFR is the amount of SFR per unit luminosity.) Since galaxy luminosity is directly proportional to mass, we are, in effect, scaling each galaxy’s SFR with respect to its mass. This is necessary since more massive galaxies should have greater star formation; without taking this into account, our average would be biased in favour of the most massive galaxies in the sample. Furthermore, it is advantageous to reduce \dot{M} by its luminosity, as opposed to mass, since in this way we can avoid determining a mass-to-light ratio for each galaxy.

However, since we are combining optical and FIR observations the correct formula is:

$$\rho_{\text{total}} = \rho_{\text{opt}} + \rho_{\text{submm}}, \quad (3.19)$$

$$\rho_{\text{total}} = \left(\left\langle \frac{\dot{M}_{\text{opt,pairs}}}{L_{\text{opt,pairs}}} \right\rangle + \left\langle \frac{\dot{M}_{\text{submm,pairs}}}{L_{\text{opt,pairs}}} \right\rangle \right) \rho_{L,\text{opt,pairs}}, \quad (3.20)$$

where $L_{\text{opt}} = L_B$ and $\rho_{L,\text{opt,pairs}}$ is given in equation 3.17.

Since \dot{M}_i values are already known, only the luminosity L for each of the pairs of galaxies remains to be calculated. The absolute B luminosity is calculated as in Patton et al. (2002),

$$\frac{L}{L_{\odot,B}} = 10^{0.4(\mathcal{M} - 5.41)}. \quad (3.21)$$

Equation 3.21 gives the luminosity of a given galaxy, in units of blue light solar luminosities, with absolute magnitude \mathcal{M} . The absolute magnitude is obtained by taking the B magnitude for the galaxy as recorded in the CNOC2 catalog. Note that since \dot{M}_i is the SFR for the whole pair (SCUBA cannot resolve individual companions), the luminosity L_i must also represent the total luminosity for both companions. The total luminosity is then given by $L_i = L_1 + L_2$, where each of the $L_{1,2}$ values is calculated separately for each member of the pair (equation 3.21).

The magnitude \mathcal{M} is then determined by

$$\mathcal{M} = B - 5 \log(D_L) - 25 - k_B - E(z) \quad (3.22)$$

where D_L is the luminosity distance given in equation 3.12 in units of Mpc; k_B is the B -band k -correction, given in the CNOC2 catalog; and $E(z)$ is the luminosity evolution of the galaxy as a function of redshift. For our purposes $E(z)$ can be approximated by $-z$ (Patton et al., 2002).

A note of caution: these values include only errors from our sub-mm fluxes; we have not included the errors from the luminosity density. More will be said on such sources of error in section 4.2.2

3.2.8 Star Formation Rate Density—A Useful Comparison

Section 3.2.7 reveals the complexity in determining ρ_{SFR} . A serious problem with its determination is the calculation of luminosity density from pairs. Furthermore, since the optical/UV SFR of our selected pairs is already $\sim 15\times$ the mean optical/UV SFR for CNOC2 field galaxies, we risk using a biased sample.

There is another method of determining whether or not pairs constitute a separate star forming group among CNOC2 galaxies that avoids many of the complications illustrated in section 3.2.7. Rather than calculating the ρ_{SFR} , which required detailed knowledge of the luminosity density, we calculate the mean star formation rate per unit luminosity:

$$\left\langle \frac{\dot{M}}{L_B} \right\rangle = \frac{1}{N} \sum \left(\frac{\dot{M}}{L_B} \right)_i \quad (3.23)$$

We should note that this quantity is equal to $\frac{\rho_{\text{SFR}}}{\rho_L}$ for a volume of 1 Mpc³, since the units are equivalent to $\frac{\dot{M}}{L_B}$. We can therefore compare the value obtained in equation 3.23 for our pairs to that for normal field galaxies for one Mpc³. The star formation rate per unit luminosity for field galaxies in our units is: 0.73 ± 0.42 . This is a significant result given its remarkable similarity to the value obtained in

equation 3.15. It is worth noting that both the SFR/L_B calculated with CNOC2 galaxies and for the general population (equation 3.15) are not dependent on the cosmological parameters chosen, so long as both the SFR's and L_B 's are calculated with consistency. In calculating the same value for our pairs we apply a weighted mean to equation 3.23. The weights used are proportional to the noise of the sub-mm flux measurements. Weighting by the flux error, rather than the SFR error, will produce the correct result. The SFR errors have been “derived,” meaning each individual flux error has been transformed to an error in SFR. That process will change the value of the SFR error according to other quantities in the calculation (eg. redshift), while leaving the flux/error ratio unchanged. By using the original flux errors we weight the data according to the uncertainty of detection, and not according to the uncertainty of a derived quantity. The results for both weighted and non-weighted SFR/L_B are displayed in Table 3.8.

Another instructive exercise is to perform the same analysis as in Table 3.8 but reducing the number of pairs used in the calculation based on their optical/UV SFR's. By choosing only those pairs with optical/UV SFR's below a certain threshold we can attempt to remove the bias of our sample away from pairs with large optical/UV SFR's. For instance, if we choose only those galaxies with optical/UV SFR's $< 9 M_\odot \text{ yr}^{-1}$ how will it affect the total SFR/L_B ? We can do the same for those galaxies with optical/UV SFR $< 7.5 M_\odot \text{ yr}^{-1}$. Table 3.9 displays the results from such an analysis. We cannot, however, set the threshold in optical/UV SFR any lower than $7.5 M_\odot \text{ yr}^{-1}$ since the sub-mm contribution then becomes dominated by those pairs with negative flux. As mentioned earlier, although these negative fluxes are an artifact of the observation techniques, we cannot simply disregard them.

Table 3.9 reveals that even when the sample of pairs is restricted in optical/UV SFR the star formation rate per unit luminosity is still at least 6–9 times greater than for field galaxies at that redshift. Ideally it would be useful to extend this experiment to a lower threshold of optical/UV SFR. In fact, in order to completely “unbias” the sample of pairs it would be ideal to lower that threshold to $\sim 1 M_\odot \text{ yr}^{-1}$.

Table 3.8: The SFR per unit blue luminosity for weighted, and non-weighted pairs. The contributions from optical/UV and sub-mm have been included in the table. Note that the relevant total of the non-weighted SFR/ L_B includes both optical/UV and sub-mm, while that of the weighted does not. This is because the non-weighted SFR/ L_B is dominated by the optical/UV SFR, which itself is significantly biased to large SFR's.

	Optical/UV	Sub-mm	Relevant Total	Factor Increase ^a
Weighted ^b	7.293	2.908 ± 0.813	$10.20 \pm 0.81^\dagger$	$\sim 15\times$
Non-weighted ^b	9.456	4.132	13.58	$\sim 20\times$

^a The factor increase over the SFR/ L_B for field galaxies at $z = 0.36$.
^b Units in $10^{-10} M_\odot \text{ yr}^{-1} L_{B,\odot}^{-1} a$.
[†] Note that error from the optical/UV SFR is as of yet unavailable.

Table 3.9: The SFR per unit blue luminosity for weighted, and non-weighted pairs. This table includes two sub-samples of our pairs, limited to those pairs with optical/UV SFR's less than a certain threshold.

Total ^a	Threshold ^b	Optical/UV ^c	Sub-mm ^c	Total ^c	Factor Increase ^d
13	< 9.5	2.512	3.838 ± 0.831	$6.35 \pm 0.83^\dagger$ ^w	$\sim 9\times$
13	< 9.5	2.724	6.783	9.507 ^{nw}	$\sim 13\times$
12	< 7.5	1.795	2.323 ± 0.845	$4.118 \pm 0.845^\dagger$ ^w	$\sim 6\times$
12	< 7.5	2.372	6.247	8.646 ^{nw}	$\sim 12\times$

^a The total number of pairs in the sample with a given threshold in optical/UV SFR.
^b The maximum optical/UV of a pair in a particular sample.
^c Units in $10^{-10} M_\odot \text{ yr}^{-1} L_{B,\odot}^{-1} a$.
^d The factor increase over the SFR/ L_B for field galaxies at $z = 0.36$. (SFR/ $L_B=0.74$).
^w Mean is weighted by flux error; ^{nw} Mean is not weighted.
[†] Note that error from the optical/UV SFR is as of yet unavailable.

Unfortunately that is not possible for reasons explained above. Nonetheless, what is interesting is that for the thresholds of optical/UV SFR chosen in Table 3.9 the contribution from the optical/UV SFR decreases along with the threshold. This seems to indicate that as the sample is unbiased (i.e. approaches a mean SFR of $\sim 1 M_{\odot} \text{ yr}^{-1}$, closer to the typical SFR of a field galaxy) the contribution from optical/UV SFR diminishes. Furthermore, even if we use Cowie et al.'s estimate of SFR/L_B for $z = 0.36$ (i.e. $1.78 \pm 0.89 \times 10^{-10} M_{\odot} \text{ yr}^{-1} L_{B,\odot}$) we would still see an increase of a factor of 2.3.

Finally, what is especially interesting from Table 3.9 is that as the threshold of optical/UV SFR is lowered we recover a ratio of $\text{SFR}_{FIR}/\text{SFR}_{opt/UV}$ of ~ 2.5 for the unweighted SFR's. This result is remarkably consistent with values in the literature (Flores et al., 1999; Hopkins et al., 2001; Bell, 2002).

Chapter 4

Discussion

4.1 Lensing Effects on SCUBA surveys

Before examining the significance and implications of the data, it is important to discuss gravitational lensing effects on SCUBA galaxies. It is currently difficult to identify the optical counterparts of SCUBA galaxies due to problems confirming redshifts; however, the possibility that these counterparts are in fact foreground lenses presents another challenge.

Some recent work (Chapman et al., 2002b) has inspired the possibility that a significant portion of the SCUBA population may be influenced by foreground lensing. The evidence lies in two radio detected, bright sub-mm sources whose optical counterparts have redshifts less than unity. To support the claim that some sub-mm sources appearing at low z are actually lensed, the dust temperatures and angular separation of these sources were examined. The centres of the sub-mm sources appeared displaced by 1-2" from the centres of their optical partners. The dust temperatures were $23 \pm 5\text{K}$ and $18 \pm 2\text{K}$. These temperatures were considered too cold when compared to the mean temperature for luminous infrared galaxies at low redshift from the IRAS catalog. This was given as evidence that the sub-mm sources could be lensed high- z

sources. Drawing on examples of lensed SCUBA sources from the literature (Fruyer et al., 2000; Smail et al., 1999; Downes et al., 1999), it appeared not implausible that lensing could be responsible for these detections.

In the cases of the known lensed sources above, the 850 μm and 1.4 GHz fluxes were comparable to those detected in Chapman et al.'s study. Chapman et al. concluded that at most 3-5% of the radio detected sub-mm population (or 2-3% of the bright SCUBA population) could be lensed.

Despite the surprise of this study there are many areas of uncertainty and a definitive account of lensing rates among sub-mm galaxies has yet to be performed. First, the dust temperatures are not as inconsistent as previously thought. As Chapman et al. concede SCUBA will preferentially find colder sources compared to IRAS surveys—making accurate comparisons of dust temperature between the two difficult. (Note that Chapman et al. used IRAS 60 μm data to infer dust temperatures for these two galaxies). Evidence for this effect has already been demonstrated (Chapman et al., 2002a). Additionally, there is considerable scatter in the T_d/L_{FIR} relation—a relation derived from IRAS data.

Furthermore, though not explicitly stated, the SED's used to derive dust temperature probably used a single temperature SED, in spite of the need to use two temperature models introduced by Dunne and Eales (2001). Therefore, the information about dust temperature alone, for these lensing candidates, is insufficiently compelling to confirm Chapman et al.'s hypothesis.

However, if we suppose that some SCUBA galaxies are lensed, and that their apparent optical counterparts are no more than foreground lenses, should this be of concern for the present research? If Chapman et al. are correct, $\sim 2-3\%$ of the bright SCUBA population would be affected. Since our objects are all below this flux threshold there should be a greater number of faint lensing candidates. This implies that the probability of choosing a lensed galaxies in the sub-mm is higher for our faint sources.

At this point there has been insufficient research in this area to warrant a total review of our detections. Neither is the evidence supporting the lensing of sub-mm galaxies conclusive, nor is there sufficient evidence to claim that our targets are lens-free. Although we will not consider the possibility of lensing of our sub-mm flux any further, we cannot altogether rule it out.

4.2 Detections

4.2.1 Confirmation of Detections

Given the many uncertainties, one could be forgiven for asking if anything was actually detected. Here we review the many indicators that lead to the conclusion that actual detections were made.

ORAC Similarity ORAC-DR, the pipeline data reduction tool used at the JCMT, has the reputation for being the most reliable data reduction package for SCUBA data. It is therefore encouraging that the reduction formula finally chosen produced signals most closely resembling those output by ORAC.

Segmentation Technique Further application of the “segmentation” technique (see section 2.2.1) improved our signals by $\sim 6\%$ over the ORAC signals while increasing the signal-to-noise ratios of the most prominent sources. (Recall that the segmentation divided the signals for each integration into groups of ten, and calculated a separate mean and error for each. This permitted the deweighting of data corrupted by weather disturbances on a timescale consistent with that of atmospheric variability.)

Ensemble Flux Both the mean and median flux for the ensemble of targets was greater than zero. In addition 65% of the individual signals were > 0 . The

mean flux of the ensemble of pairs was 0.59 ± 0.26 mJy, indicating that the flux is a 2.2σ measurement (97% confidence).

Poissonian Noise A further test of the data's reliability was the Poissonian behaviour of the noise for the $850 \mu\text{m}$ detector. This was indicated by the near $-\frac{1}{2}$ slope on a log-log plot of noise versus integration time; this in turn reveals that the noise was consistent with random photons hitting the detector. That the noise is physically real was also indicated by noise levels among serendipitous sources and sky-pointing bolometers: The noise for these data also decreased as the inverse square of integration time.

χ^2 test A χ^2_ν test was performed to determine how closely our data fit a zero-flux function. For randomly selected pairs the χ^2_ν value was 3.76, meaning there was much less than a 0.1% chance that their fluxes could have been drawn from a set of null fluxes. The value of χ^2_ν for all 26 targets was 3.20 implying a chance that they could be drawn from null fluxes of much less than 0.1%.

Individual Detections Finally, individual sources were detected above the 3σ level (pair 68 was nearly 4σ). Also encouraging was a small sample of detections with $2.5\sigma \leq S/N \leq 3\sigma$. These three pairs provide evidence that detectable sub-mm pairs exist; with slightly more integrations these pairs would have graduated to the 3σ detection regime.

At this point it is perhaps worthwhile examining why a 3σ observation is considered a "detection." In optical astronomy, this threshold would never be considered sufficient for confirming a detection; nevertheless we must keep in mind the spectral region being observed, the nature of our sources, and the difficulty of the observations.

First, the sub-mm part of the sky is highly susceptible to atmospheric variability and opacity, a fact that results in a great deal more noise. The nodding that the our instrument performs is intended to compensate for this sky noise, but under especially noisy conditions, negative fluxes can result.

Second, the dustiest, and hence FIR brightest, galaxies such as ULIRG's are found at redshifts $z \geq 1$; similarly the sub-mm luminosity density is much larger at $z \simeq 1$. It must also be remembered that our sources were selected from among optically confirmed pairs in the CNOC2 catalog, not from a sub-mm survey. So although SLUGS achieved signal-to-noise ratios of ~ 8 , SLUGS galaxies were 25 times closer in luminosity distance, and selected from among the brightest IRAS galaxies. Achieving signal-to-noise ratios of 8 or more for CNOC2 galaxies is simply unrealistic.

We felt that a threshold of 3σ was acceptably high given that it implies a detection with 99.7% confidence. However a 2.5σ limit would still mean confidence at the 98.7% level, and 2.5σ sources are used later in some of the discussion. In other words we can be 99.7% confident that the fluxes from the two 3σ sources are truly positive. How confident can we then be about the star formation rates calculated from these fluxes? Recall that the SFR for pair 08 was $50.7 \pm 16.0 h^{-2} M_{\odot} \text{ yr}^{-1}$ and for pair 68, $45.6 \pm 11.6 h^{-2} M_{\odot} \text{ yr}^{-1}$ ($\Omega_M = 0.2$ and $\Omega_{\Lambda} = 0$), where the uncertainty quoted is $\pm 1\sigma$. From this it can be inferred that, at the 95.4% (2σ) confidence level, both of these star formation rates are $> 20 M_{\odot} \text{ yr}^{-1}$. Such a star formation rate, a factor of $\gtrsim 20\times$ the value for our own Milky Way galaxy, would still be significant.

4.2.2 Other Sources of Error

The final star formation values that we quote have left out several sources of error. This was done intentionally so that the errors in the final values reflect only the error of detection. The inclusion of the errors listed below would have increased the final uncertainty by $\sim 2 - 3\times$, making the final values appear as if nothing had been detected. Although such errors would have been statistically valid the significance of the detections would be lost on the reader.

The first errors that were omitted were the uncertainties in T and β . Recall that these values were calculated by Dunne et al. (2000) by taking the standard deviation

in T and β for their 104 sources. We have omitted this uncertainty since it would have a systematic effect for all of our final values.

Second, there is no error yet available for the optical SFR's. Had there been these would have been included, but given better observing conditions in the optical measurement error of these values would have been small compared to our sub-mm measurements. In any event most of the error in the optical SFR estimates would come from empirical uncertainty in the calibration of [O II] line fluxes with SFR.

4.3 Significance of Detections

With a strong case made that the 3σ signals represent actual detections of objects their significance can now be postulated. First the detection rate is considered. Throughout this thesis it has been claimed that two detections were made: pair 08 and pair 68. For the purposes of statistical analysis the most randomized sample of pairs is desired so that it reflects the parent population (CNO2) as much as possible. Pair 08 was specifically chosen as a SCUBA target because of its prodigious optical SFR and thus was not chosen randomly. In order to maintain as much randomness as possible we have discarded pair 08 from this analysis. The presence of the other three “near” detections, though not above the 3σ threshold, is an encouraging sign that other detections among the pairs could have emerged given more observing time. These objects will be used in this section as well.

4.3.1 Inferring sub-mm flux from SFR's

The motivating question in determining the significance of our pair detections is: What is the likelihood that pairs, given their SCUBA detection rate, are drawn from the CNO2 population? Put another way, we are asking what is the probability that they constitute their own, separate star forming population. To answer this question

quantitatively we examine the probabilities of achieving the same detection rate as for pairs in the CNOC2 population. Thus we can ask: Is the CNOC2 ensemble really the parent population from which pairs are drawn?

To test this hypothesis we begin with the assumption that star formation rate, as measured in the optical or UV bands, traces exactly the star formation rate as inferred by FIR measurements. This is equivalent to saying the observed optical/UV SFR equals the observed FIR SFR. This assumption is certainly open to debate and its validity will be discussed shortly. However, for the moment this simple relation is assumed.

$$\dot{M}_{sub-mm} = \dot{M}_{opt/UV} \quad (4.1)$$

Given the situation described above we can work backwards. Instead of measuring sub-mm fluxes and determining a star formation rate, we begin with an optical/UV SFR and calculate the necessary sub-mm flux to infer the that SFR. The CNOC2 catalog, which has optical star formation rates calculated for 5404 galaxies, was used (Lin and CNOC2 Collaboration, 2001).

Given ~ 5400 opt/UV SFR's and their redshifts, $850 \mu\text{m}$ fluxes were constructed. These fluxes were then divided by 1.4mJy , the level of noise consistent with 300 integrations of observing (300 integrations was the median integration time for our pair observing). This produced signal-to-noise ratios expected for each CNOC2 galaxy as if they had each been observed for 300 integrations using SCUBA.

If the pair sample is truly derived from the CNOC2 population then there should be the same rate of detections among them as we found for the pairs. For this analysis we use the 4 pairs detected at $> 2.5\sigma$, rather than the 1 pair detected $> 3\sigma$,

$$\text{pairs } \frac{4}{18} \simeq \frac{1200}{5400} \text{ all CNOC's.} \quad (4.2)$$

According to this calculation there should have been ~ 1200 galaxies having inferred signal-to-noise ratios greater than 2.5σ using the method described above; instead, only two (out of ~ 5400) were found above that threshold using optical/UV SFR's.

(See Figure 4.1.) This is the first evidence that pairs are not drawn from the general CNOC2 population.

For interest's sake, we can repeat this calculation using the serendipitous sources, for which 97 have optical/UV SFR's. This ensemble is just a small sample of the CNOC2 population so it will not provide a complete picture, but it is informative nonetheless. Only one of the 97 galaxies would have been detected at the 2.5σ level, given the above assumption, see Figure 4.2. (Indeed, that even one could have been detected is surprising, since only 2 would have been detected for the "parent" population of 5400 CNOC2 galaxies.) This can only be attributed to chance.

The preceding calculation is not conclusive since a different relationship between observed optical/UV SFR and FIR can be chosen. For instance, if sub-mm SFR were greater than that inferred by optical/UV the amount of sub-mm flux needed to account for the SFR would increase, and this would also increase the signal-to-noise ratio and provide more inferred 2.5σ "detections." (Note that noise remains constant at 1.4 mJy for 300 integrations, independently of source flux.)

By increasing the observed FIR SFR with respect to opt/UV SFR we are physically changing the expected environment of these galaxies. With a relation of one-to-one, half the bolometric optical/UV energy emitted from massive, young stars escapes and is detected in the UV, while the other half of the energy is absorbed by dust and re-emitted in the far infrared, where we observe it with instruments like SCUBA (assuming negligible line emission). When the observed FIR SFR dominates the bolometric luminosity, the majority of the spectral energy is absorbed by dust, and only a small fraction is detected as optical or UV radiation. The following relation can be used:

$$\dot{M}_{\text{submm},\star} = \eta \times \dot{M}_{\text{opt/UV},\star}, \quad (4.3)$$

where η is a constant of proportionality.

One can then ask: what value of η is needed in order that the same detection rate is inferred among CNOC2 galaxies as with our pairs. This can be determined by

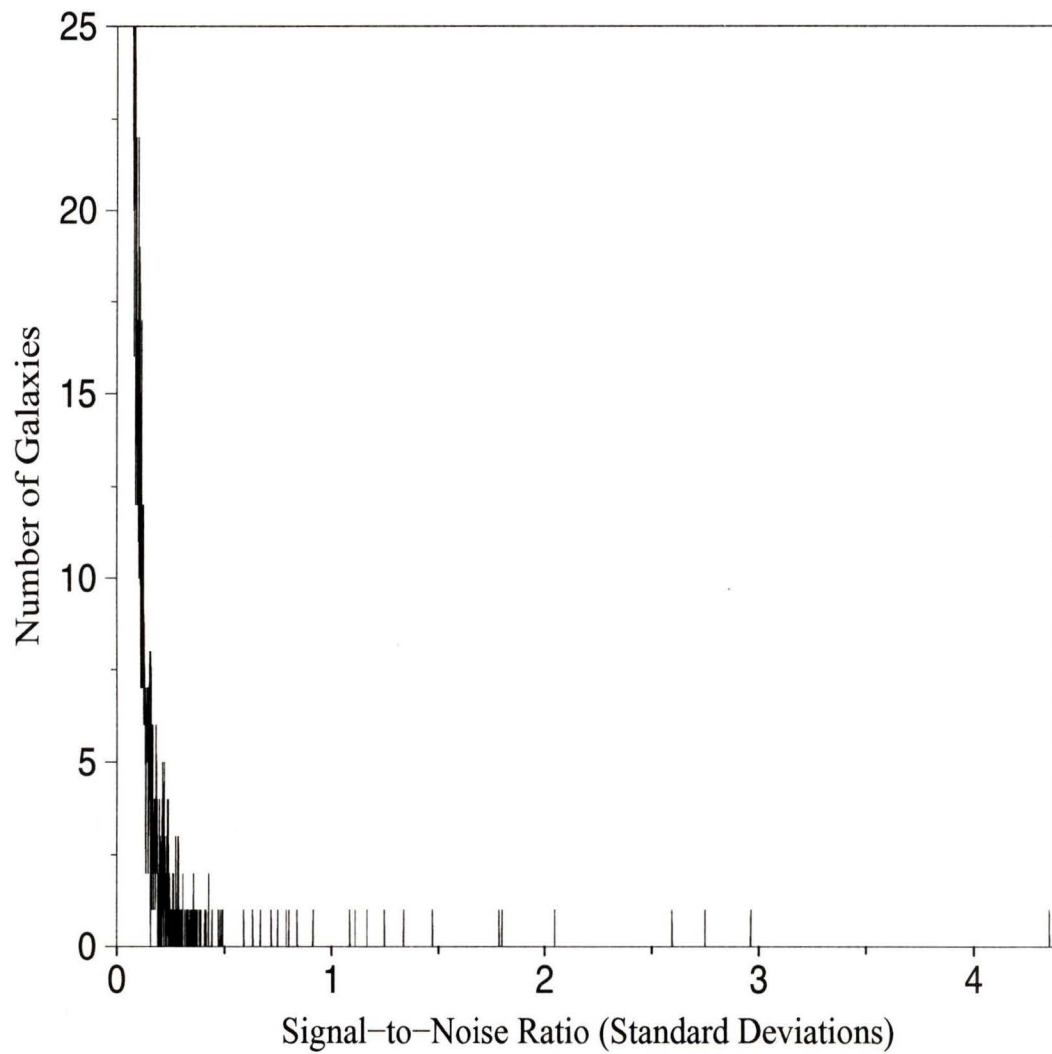


Figure 4.1: Inferred S/N ratios of $850\ \mu\text{m}$ flux for 5404 CNOC2 galaxies assuming that optical/UV SFR traces sub-mm SFR (i.e. $\eta=1$). The mean S/N is 0.059.

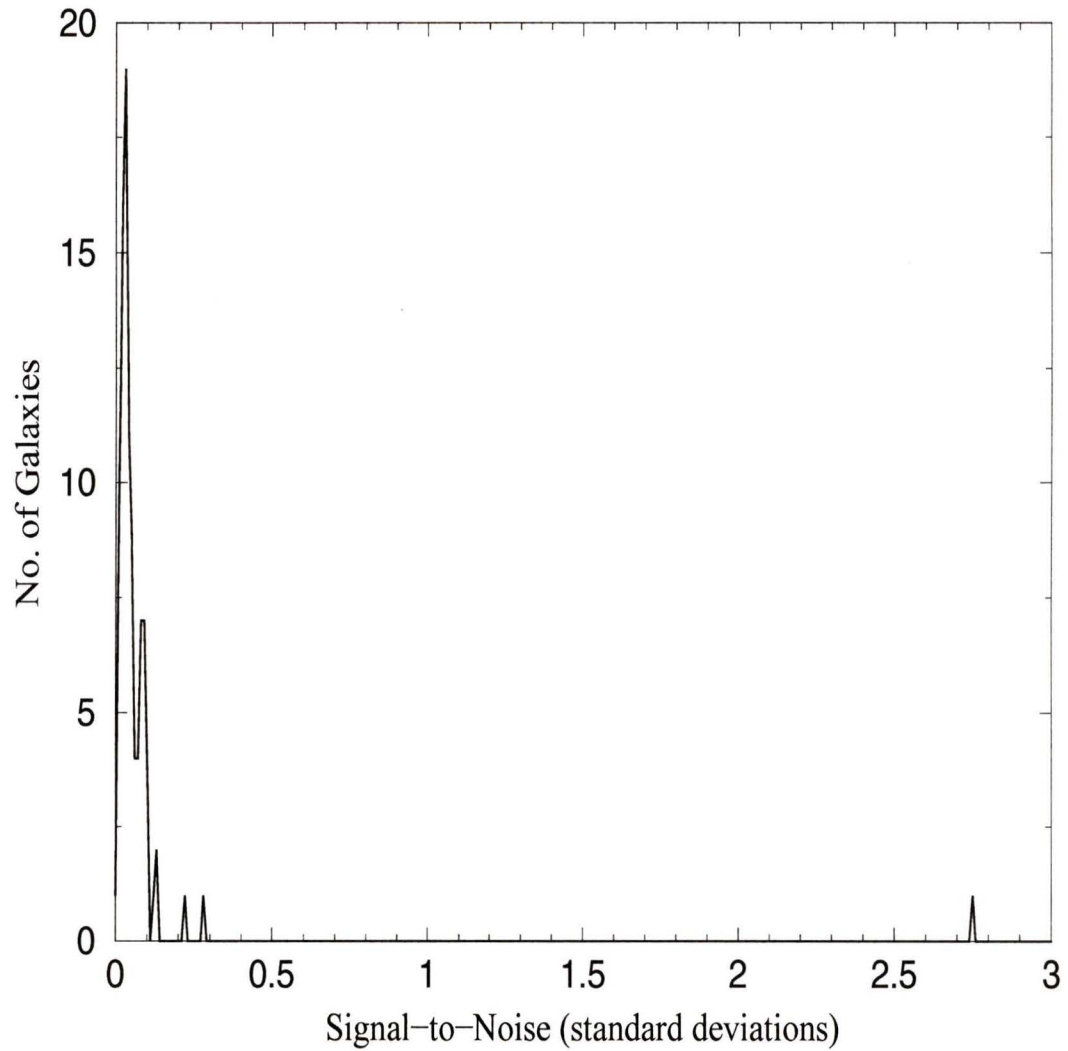


Figure 4.2: Inferred S/N ratios of $850\ \mu\text{m}$ flux for 97 serendipitous galaxies assuming that optical/UV SFR traces sub-mm SFR (i.e. $\eta=1$, where η is defined in equation 4.3).

computing the inferred signal-to-noise for CNOC2 galaxies while varying η until at least 1200 CNOC2 galaxies (out of 5400) are found above the 2.5σ limit. This value is $\eta \simeq 33$, implying that 97% of star formation accounted for by the dust emission while only 3% is accounted for by optical/UV emission.

If we consider all sources detected above 2σ (5/18 pairs) we might expect ~ 1500 inferred detections. The required value of η is $\simeq 30$. This implies that optical/UV emission accounts for only one part in ~ 30 of observed star formation. Using the model for total SFR shown in section 1.4.7 we can measure η as a function of τ , the absorption. Figure 4.3 shows this relation and a value of $\eta \simeq 30$ corresponds roughly to an absorption of $\tau \simeq 1.38$. In both of these cases a very dusty scenario is required.

A value of η as high as ~ 30 is most probably unreasonable since we do not expect the average galaxy at moderate redshift to be so utterly enshrouded in dust. Due to the unlikely nature of this dusty regime we are furnished with further evidence that the typical CNOC2 galaxy could not contain enough dust to be detected at the 2.5σ or 2σ level (as the pairs are).

The possibilities have still not been exhausted, for there is another, more definitive, analysis that can be done.

First begin with a rough calculation. Suppose, again, that the CNOC2 population is the parent population for our pairs. Given a distribution of signal-to-noise as in figure 4.1 which has a mean S/N of 0.059, the probability of observing a signal-to-noise ratio of 2.5 is then calculated by using the binomial distribution:

$$P(x, \mu) = \frac{\mu^x}{x!} e^{-\mu}, \quad (4.4)$$

Given a probability of 4/18 of making a 2.5σ detection we compute equation 4.4 as:

$$\frac{4}{18} = \frac{\mu^{2.5} e^{-\mu}}{2.5!}. \quad (4.5)$$

Solving for the mean yields $\mu = 1.874$. This implies that in order to make the correct number of 2.5σ detections the parent population must have a mean inferred signal-to-

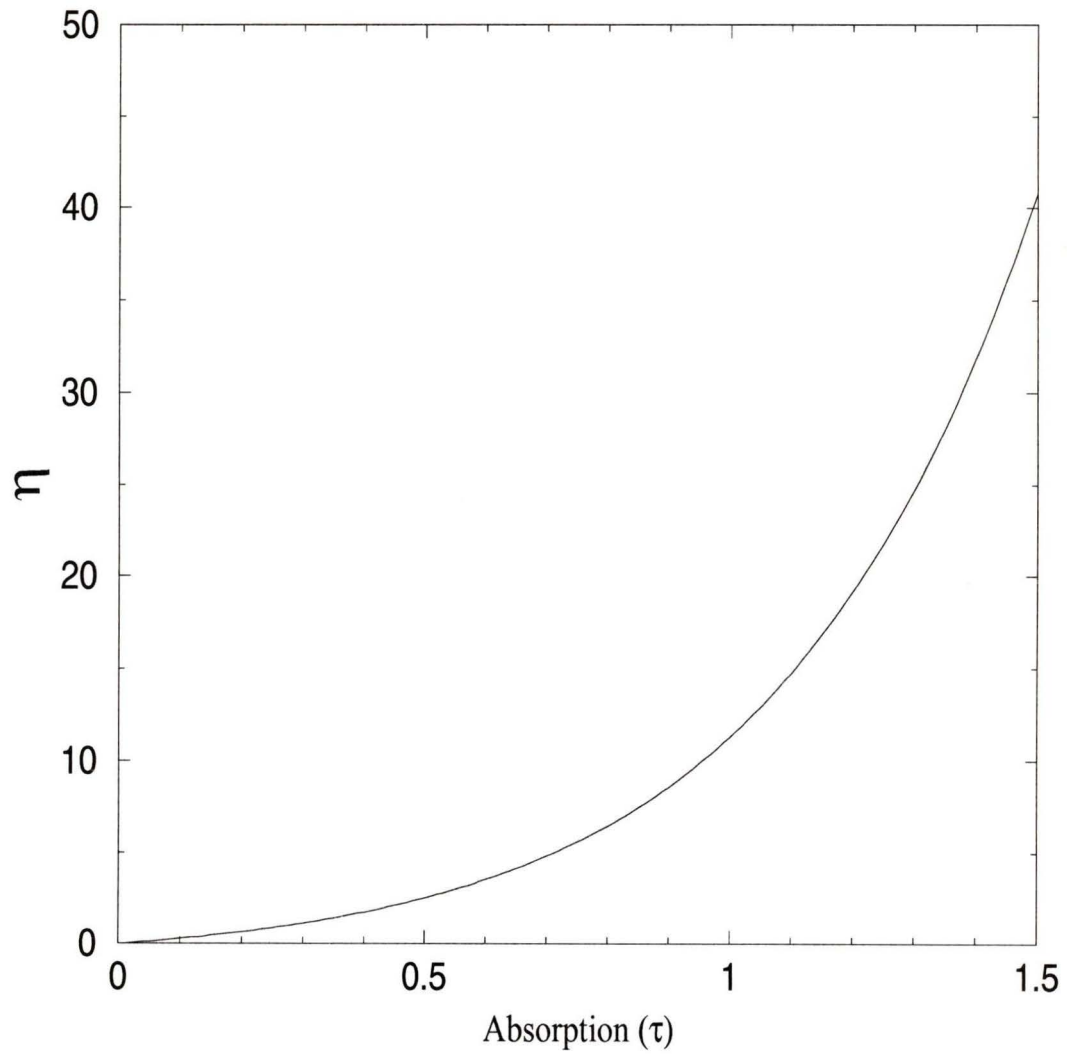


Figure 4.3: The quantity η as a function of absorption. This plot was generated using the SFR's from the absorption and re-emission model of section 1.4.7.

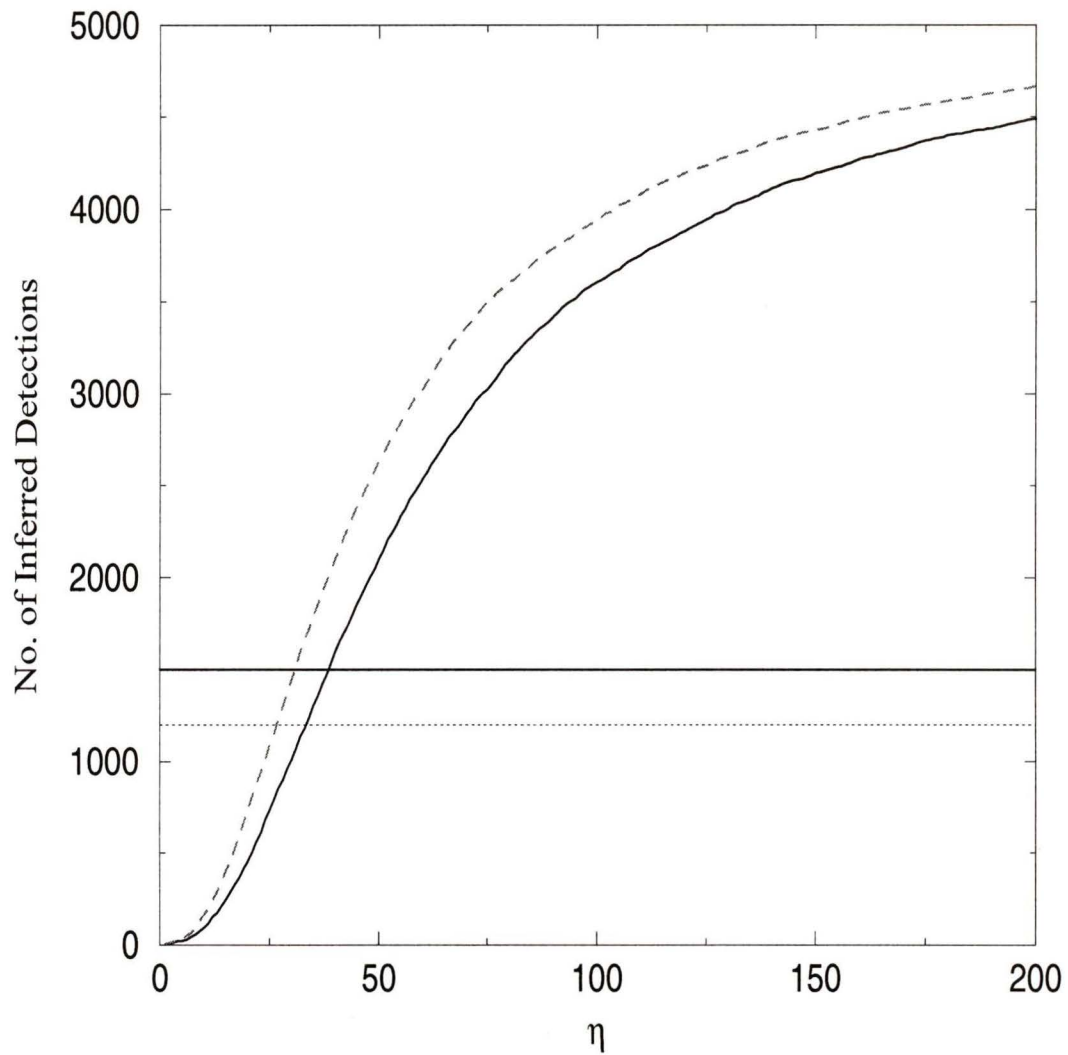


Figure 4.4: The number of inferred detections at 2.5σ (solid line) and 2.0σ (dashed line) out of ~ 5400 CNOC2 galaxies for varying η (η is defined in equation 4.3). The thick (upper) horizontal solid line is plotted at 1500 detections; the number necessary for 2σ detections. The thin (lower) horizontal solid line is plotted at 1200; representing the number of necessary 2.5σ detections.

noise ratio of 1.87. Now it can be determined what value of η would give a distribution with mean 1.87. By iterating over η , it was determined that a value of $\eta \simeq 32$ would be necessary to achieve a distribution that would infer the correct number of 2.5σ detections. In other words, in order that the CNOC2 population have the same rate of detections as the pairs $\sim 96\%$ of young, stellar spectral energy would have to be absorbed by dust. Note that this value of η agrees with the earlier estimate of $\eta \simeq 33$.

Performing the same calculation for 2σ detections (inferring 1500/5400) we find that a mean of $\mu = 1.238$ would be necessary. The value of η required to give such a mean would be $\eta \simeq 21$. For both of these detection thresholds (2.5σ and 2σ) the η necessary to obtain the correct number of inferred detections implies a very dusty scenario.

The preceding calculations can be done for the 7 field galaxies. Although no detections were made and the χ^2_ν analysis showed no definite significance of detection, we can perform a similar calculation. The highest signal-to-noise ratio for field galaxies was $S/N \simeq 1.7$; therefore we can determine the maximum value of η for which there are no inferred S/N greater than 1.7. This value is $\eta \simeq 0.39$, suggesting FIR emission accounts for as little as 28% of SFR. (A value of $\eta \simeq 0.39$ corresponds to a value of τ_V of 0.13. See Figure 4.3). This value represents a lower limit since the S/N of $\simeq 1.7$ would only increase with further integration time.

We have inferred the number of 2.5σ and 2σ detections from the CNOC2 population and calculated the probability that the pairs could be derived from such a group. The statistics paint a picture that suggests pairs are very unlikely to have the CNOC2 population as a statistical parent population as far as SFR's are concerned. Only if the amount of dust is very high in CNOC2 galaxies could such a scenario be envisioned. Thus there remain two possibilities to explain this discovery: either the pairs constitute a sample of star formers distinct from the CNOC2 population, or the amount of dust obscuration is excessively high among the CNOC2 galaxies.

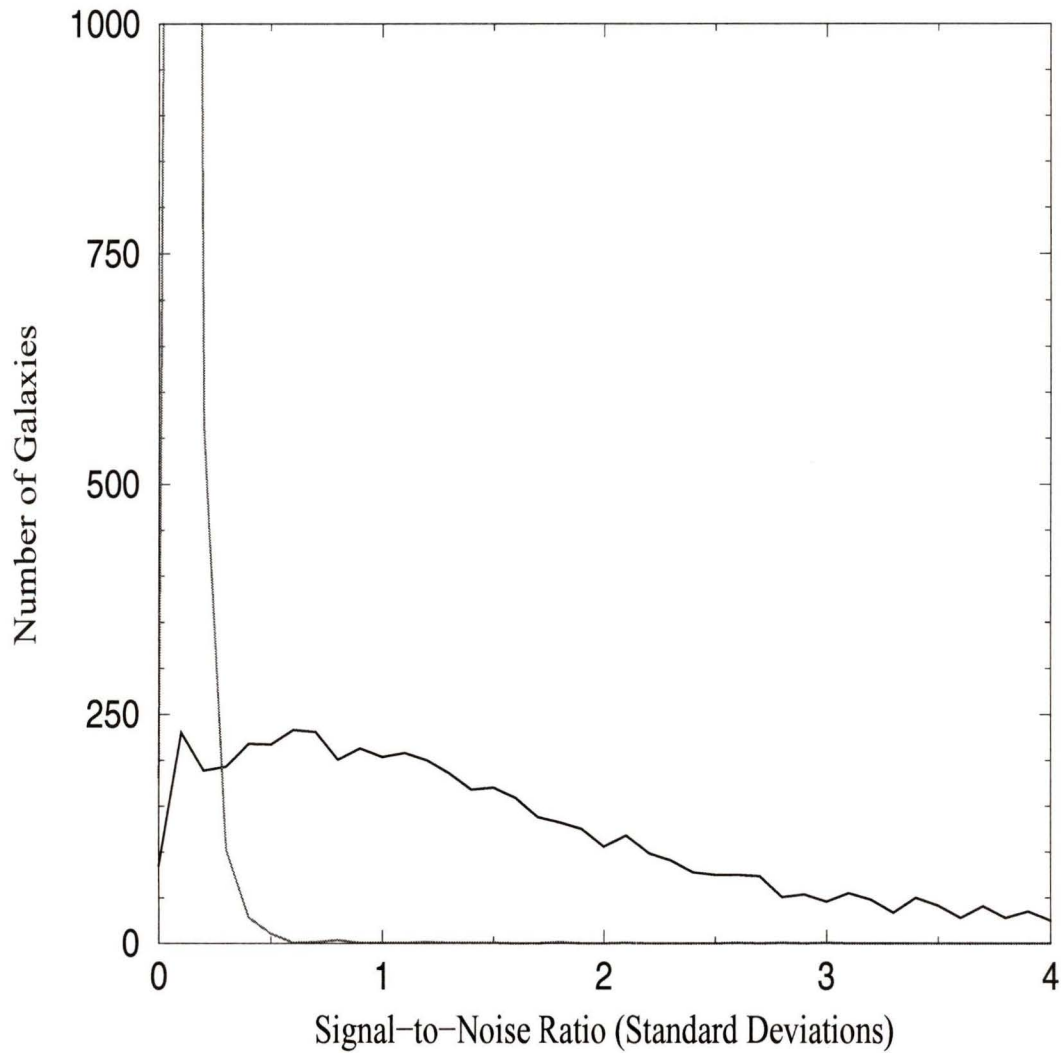


Figure 4.5: Comparison of two inferred-flux distributions. The tall one is identical to figure 4.1, having $\eta = 1$. The distribution to the right has $\eta \simeq 32$ and has a mean of ~ 1.874 and median of 1.24, the value necessary in order to make the same rate of 2.5σ detections as for pairs

4.3.2 Monte Carlo Tests

Another way to determine the significance of detection is by performing a Monte Carlo test. Recall that the weighted mean SFR for pairs was $5.5h^{-2} M_{\odot} \text{ yr}^{-1}$. Knowing optical/UV SFR's for ~ 5400 CNOC2 galaxies we can ask: what is the probability of drawing a sample of 18 pairs (36 individual galaxies) from that population and obtaining mean SFR's greater than $5.5h^{-2} M_{\odot} \text{ yr}^{-1}$? Using a random number generator, 36 optical/UV SFR's were chosen at random from a total of 5404 SFR's, and an average was calculated for each group. Out of 10000 trials, groups of galaxies with an average SFR greater than $5.5h^{-2} M_{\odot} \text{ yr}^{-1}$ occurred once. We can then say at the 99.80% confidence level that our pairs could not be randomly drawn from the general CNOC2 population.

We can repeat this test by multiplying the optical/UV SFR's from the CNOC2 survey by a factor of ~ 3 (see section 1.4.6). In this way the SFR's should approximate those values expected from FIR surveys. Even when the Monte Carlo simulation is performed this way, we can still say at the $\sim 95\%$ confidence level that our pairs cannot be randomly drawn from the general CNOC2 population.

4.4 Dust Obscuration

It has been demonstrated that not only have real fluxes been detected but that statistically these detections are very unlikely. This makes the discovery of such sources in the sub-mm very surprising. The possible explanations for this discovery have been reduced to two: distinct star forming behaviour or high dust absorption.

The dust absorption necessary to produce the rate of detections we observed is very high. Put more quantitatively, the amount of star formation inferred by FIR flux would have to be greater than that inferred by optical/UV by $\sim 30\times$ (for 2.5σ sources, 97% confidence). One explanation for this is that nearly all of the UV radiation is

being absorbed dust. This section is concerned with determining whether or not such a scenario is reasonable.

We began with an assumption that star formation (as inferred by FIR indicators) traces optical/UV SFR. That is, if one were to measure a SFR in the UV it would agree with that measured in FIR. However, just by examining Figure 3.3 carefully another picture is observed. One notes that none of the field galaxies, chosen for their high optical/UV SFR's, were detected in the sub-mm ($S/N_{\text{field galaxy}} < 1.7$); even their submillimeter-inferred SFR are all small compared to their optical/UV SFR's. If the assumption just made were true, we would expect much higher sub-mm fluxes and hence SFR. According to Table 3.2 the field galaxies should have had $850 \mu\text{m}$ fluxes $S_{850 \mu\text{m}} \gtrsim 6 \text{ mJy}$ (implying signal-to-noise ratios of $S/N > 3.6$). But instead, we found that the significance of detection was low for field galaxies (from the χ^2_ν test), and that the η value describing the relation between optical/UV and FIR SFR could be as small as 0.39, meaning that the highest optical/UV star formers have the least amount of dust absorption.

Most significant, though not obvious, is the locus of pairs. One of our 3σ detections and all of our $> 2.5\sigma$ detections lie near the x-axis, indicating low optical/UV SFR and high sub-mm SFR. One might be tempted to scoff at the claim that our sub-mm SFR's were "high," considering that the field galaxies have optical/UV star formation rates of $> 50 M_\odot \text{ yr}^{-1}$. However, according to table 3.4 4/5 pairs detected $> 2.5\sigma$ had SFR's $> 20 M_\odot \text{ yr}^{-1}$, well in excess of the Milky Way galaxy. Furthermore, one must be cautious in drawing comparisons with the field galaxies since they were selected from among the highest star formers in the CNOC2 population (top 0.5%), while the pairs were chosen at random. One interpretation of Figures 3.3 and 3.4 is that star formation in the CNOC2 population is dichotomized between those galaxies occupying a region of high optical/UV, low sub-mm SFR and those consisting of high sub-mm, low optical/UV SFR. Since our field galaxies were found mostly in the former region it is possible to claim that most optically-selected field galaxies might preferentially be found there, while pairs are found in the latter region.

This scenario is the very opposite of our original assumption, that the two measures of SFR should trace each other along the line of star formation parity. It would also make it difficult to find a relation between optical/UV SFR and sub-mm since a line of best fit would be needed for each regime. In this event the value of η (see equation 4.3) would be very large for the dusty regime and very small for the dustless regime. (See Figure 4.6 for an illustration of this scenario.)

One of the advantages of this interpretation is that it explains how the field galaxies could have such high SFR's while not being detected in the FIR according to the literature. The value of η is most certainly > 1 which implies there ought to be more star formation inferred in the FIR than optical/UV. Our field galaxies have SFR's $50 - 200 M_{\odot} \text{ yr}^{-1}$ and therefore should have had inferred FIR SFR's greater than this range by a factor of $\sim 3\times$. That they were not detected at sub-mm wavelengths suggests they are likely dust-poor while still maintaining high SFR's measured in the optical.

Physically, this interpretation could mean that the typical star formation region in a field galaxy contains less dust, on average, than such a region in pairs. If this were the case it might be expected that interacting pairs have higher dust masses (scaled by total mass) than field galaxies.

But, a simple calculation of the quantity $R = M_d/L_B$ using Dunne et al.'s data for dust mass and L_B suggests this is not the case, at least not for sub-mm selected galaxies in the local Universe. The mean R for SLUGS field galaxies is $1.843 \times 10^{-3} M_{\odot}/L_{\odot}$, while for SLUGS pairs its is $1.614 \times 10^{-3} M_{\odot}/L_{\odot}$. Note, however, that SLUGS pairs are only those determined with SCUBA images having sky separations of < 4 arcmin. There are other pairs in the sample that were not identified by SCUBA (as has already been noted).

Dust mass is given by:

$$M_d = \frac{S_{850} D_L^2}{\kappa_d(\nu) B(\nu, T_d) (1+z)}, \quad (4.6)$$

where $B(\nu, T_d)$ is the blackbody spectrum at rest wavelength ν , D_L the luminosity distance, and $\kappa_d(\nu)$ is the mass absorption coefficient. (Note that equation 4.6 is valid for all z). Although there is little agreement on the value of $\kappa_d(\nu)$ at $850 \mu\text{m}$ we have taken the same value used by Dunne et al. (2000), $\kappa_d(\nu) = 0.077 \text{ m}^2 \text{ kg}^{-1}$, which is intermediate between the values of Draine and Lee (1984) and Hughes et al. (1993). Since the dust mass is directly proportional to S_{850} , the $850 \mu\text{m}$ flux, it is impossible to calculate meaningful dust masses for individual pairs and field galaxies given the low signal-to-noise ratios. However we can calculate the mean dust mass.

The weighted mean dust mass and R value for pairs are $\bar{M}_d = 9.42 \pm 4.18 \times 10^6 M_\odot$ and $\bar{R} = 7.43 \pm 4.54 \times 10^{-4} M_\odot/L_\odot$. The respective values for field galaxies are $\bar{M}_d = 7.06 \pm 4.43 \times 10^7 M_\odot$ and $\bar{R} = 4.99 \pm 3.84 \times 10^{-3} M_\odot/L_\odot$. Thus, even accounting for the large uncertainty in R values, the field galaxies have larger scaled dust masses than the pairs.

In spite of the fact that the scenario illustrated in Figure 4.6 explains the behaviour of the field galaxies, recent studies have shown that there does in fact exist a relation between optical/UV SFR and FIR SFR. In other words there exists a mean value of η .

A recent study (Kewley et al., 2002) compared SFR's from both the far-infrared and $\text{H}\alpha$ (6563\AA) and found a value of η close to 3.

However, other studies (Charlot et al., 2002) have observed different results, using data from the Stromlo-APM redshift survey. Charlot et al. (2002) determined that FIR estimates of SFR still exceeded $\text{H}\alpha$ and $[\text{O II}]$ estimates by a factor of $\sim 3\times$, even after a mean attenuation of $A_{\text{H}\alpha} = 1$ was applied.¹ Furthermore, Glazebrook et al. (1999) reported that:

$$\frac{L(2800\text{\AA})}{L(\text{H}\alpha)} = 3.1 \pm 0.4 \quad (4.7)$$

which implies that $\text{H}\alpha$ SFR is $\sim 3\times$ greater than $L(2800\text{\AA})$ SFR. This in turn implies that FIR SFR is as great as $\sim 9\times$ greater than UV continuum SFR.

¹Recall that $[\text{O II}]$ estimates of SFR are calibrated via $\text{H}\alpha$.

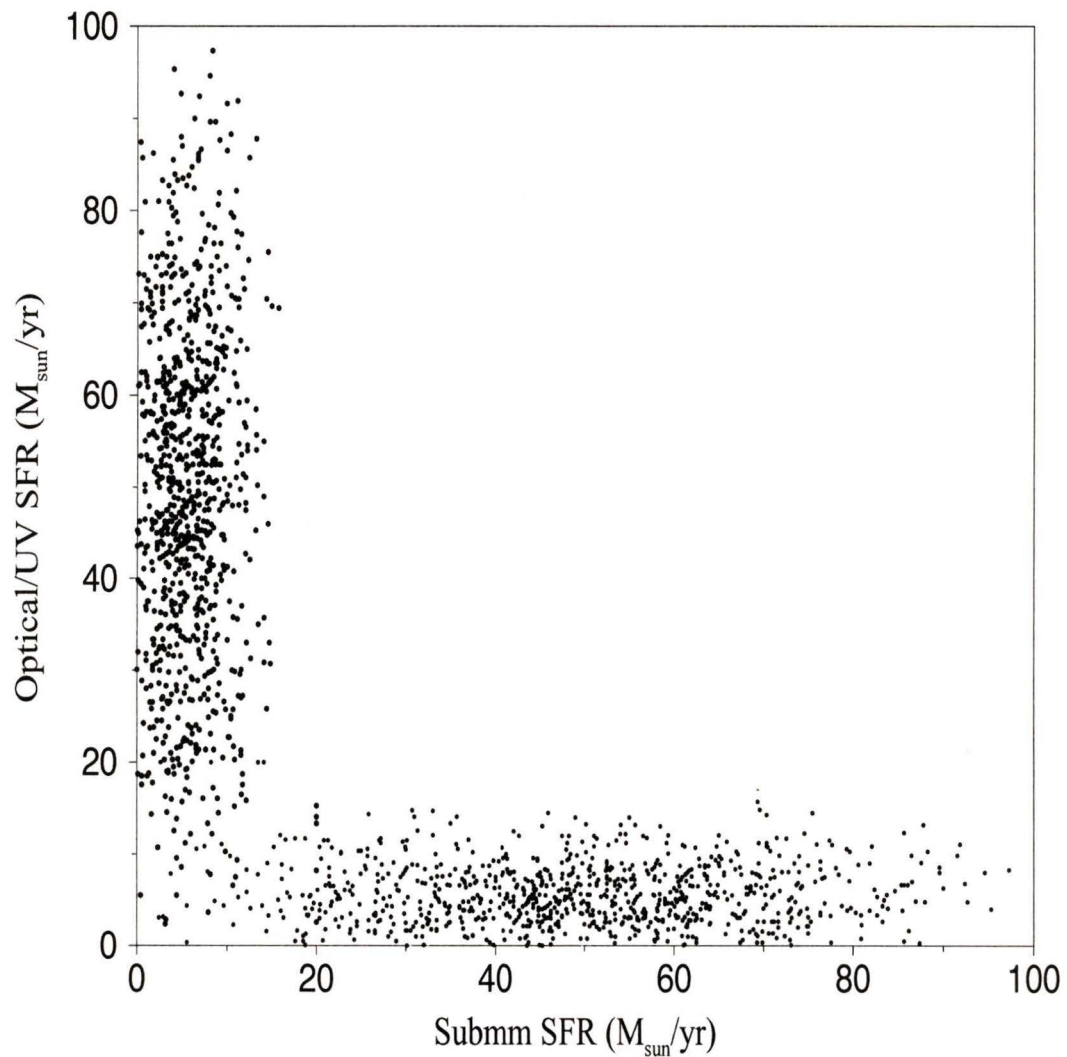


Figure 4.6: This plot shows a hypothetical division between star forming behaviour. At the left are galaxies with little dust; most star formation is observed at optical/UV wavelengths. Those objects along the bottom are those heavily dust enshrouded galaxies for which most SFR is inferred by FIR flux. This plot is intended as an illustration of the most extreme case of the two regime star formation model.

There has yet to be agreement upon the precise correlation between these three measures of SFR ($H\alpha$, UV and FIR continuum). Nonetheless, it appears that some form of linear correlation exists between these indicators (with a value η of a few) and that the two-SFR regime, illustrated in figure 4.6, is not generally representative of real star formation in most galaxies. The most likely explanation for the apparent dichotomy of optical/UV and sub-mm SFR in Figures 3.4 and 3.3 is a selection effect. Since the optical/UV data were obtained with observations in those wavebands and the FIR data was obtained from sub-mm measurements, both sets of observations were more likely to detect the brightest sources in their respective wavelengths. It should therefore come as no surprise that the highest optical/UV star formers have very little dust. If they did possess a lot of dust they would not have been observed to have such high optical/UV SFR's.

Given that optical/UV indicators of SFR underestimate FIR star formation by factors of only a few, it seems very unlikely they could be as high as $\sim 20 - 30\times$, as required by the possible explanation at the beginning of this section. On the other hand, if FIR SFR represents $\sim 3\times$ optical/UV SFR (as the literature suggests) then only $35 - 40/5400 \simeq 1/150$ of CNOC2 galaxies should have been detected in the sub-mm within the range of confidence of $2\sigma - 2.5\sigma$, and not the $5/18$ we detected. Since a reasonable value of η from the literature cannot infer the correct rate of detections among pairs, and since the only value of η that *can* infer the proper rate is unreasonably large, we must conclude that pairs constitute an entirely separate population of galaxies in terms of their star forming behaviour.

4.5 Significance of the Star Formation Rate

We have shown in this thesis that the pairs likely constitute a unique group of star forming galaxies compared to the general CNOC2 population. This uniqueness is based on statistical analysis that shows that our sub-mm measurements are not consistent with what we would expect to see from the CNOC2 population. The only

way that our observations could be consistent with what we know of the CNOC2 SFR's is if dust absorption is very high, as high as $\eta \sim 30$. Since the literature shows that there is likely a linear relationship between FIR and optical/UV SFR, and that the two indicators agree to within a factor of a few (not ~ 30) there is little support for the existence of large amounts of dust absorption at moderate redshift.

To what extent, then, are the pairs distinguished by their star formation behaviour from the general CNOC2 population?

The most difficult challenge in answering this question is the apparent bias of the pair sample. As shown in Table 3.6 the mean optical/UV SFR for our pairs is $\sim 15\times$ greater than the average SFR of the CNOC2 population. This implies that a representative sample, in terms of SFR, was not chosen, whether intentionally or inadvertently. Nonetheless, the significance of the sub-mm detections, demonstrated in the previous two sections, is still manifested in the ρ_{SFR} . When the SFR per unit blue luminosity is calculated and weighted to reflect the significance of sub-mm detections, the SFR/L_B still exceeds the expected value of the field galaxies by $15\times$ (and at least $6\times$ when only those 12 pairs with optical/UV $\text{SFR} < 7.5 M_{\odot} \text{ yr}^{-1}$ are considered). Even using the larger estimate of Cowie et al. (1999) for the SFR/L_B at $z = 0.36$ there will be an increase of at least a factor of ~ 2 . This fact is rather astonishing given that when weighted, the optical/UV contribution to SFR/L_B decreases. Furthermore, these pairs were originally optically selected and are thus less likely to be candidates for high sub-mm SFR.

Since the sample is not altogether representative of the general CNOC2 population in terms of optical/UV SFR we cannot make any further generalizations or conclusions. However, we can claim with reasonable confidence that interacting pairs among the CNOC2 population at moderate redshift do constitute a separate population of star formers. The excess of star formation among pairs at this redshift may be as high as $15\times$, with the most conservative estimate being $2\times$. A sample of pairs with SFR's more consistent with the general population is needed to explore this question further. Further comparison will be possible once more definitive optical/UV SFR's

are published, but for the present this is a tantalizing result worthy of further study.

Chapter 5

Conclusions

5.1 Summary

We began with a sample of 27 optically-selected targets from the CNOC2 survey. Twenty of these were interacting pairs as defined by Patton et al. (2002), while the other seven were isolated field galaxies chosen for their high optically-inferred star formation rates. These targets were observed at $850\ \mu\text{m}$ and $450\ \mu\text{m}$ with SCUBA at the JCMT between December 1999 and March 2002. Each target was given an average of 300 integrations of exposure time, which corresponds to approximately two hours of integration. The raw data were processed to give bolometer signals. These signals were then reduced according to an algorithm made up of SURF commands that ensured the simplest, most reliable fluxes. A further reduction step was included to try to account for sky variability on the timescale of atmospheric effects. This technique not only increased our average signal-to-noise ratio but also revealed two sources with $S/N > 3\sigma$. This is considered a reliable threshold with which to judge a detection for these faint sources. In addition to these two detections, three other detections ($2.5\sigma < S/N < 3\sigma$) were observed. None of the field galaxies was detected in the sub-mm above a S/N ratio of 1.7.

The physicality of the 850 μm data was reasonably confirmed by analysing the noise for a Poissonian noise dependence. The 450 μm fluxes regrettably had to be discarded, due to their non-Poissonian noise. The short wavelength fluxes were likely distorted by greater sky variability and reduced atmospheric transmission. The likelihood that the signals from pairs constituted actual positive flux was confirmed by performing a χ^2_ν fit to a normal distribution about zero flux. By showing that there was an $> 99.9\%$ probability that our pairs' signals were not be drawn from such a population we showed that they were not the result of random noise fluctuations. The χ^2_ν value for field galaxies produced a 40–50% probability that they could be drawn from such a population.

A corollary goal of this research was to capture other serendipitous CNOC2 galaxies within the field of view of our targets. These serendipitous galaxies would then provide a random sample of sub-mm observations from the same survey with which to compare the pairs. Discovering these galaxies proved especially difficult given that the field of view rotates in a non-uniform manner, and that 70% of the array area is dead space. The serendipitous data were corrected for deviations in the beam shape in RA at large declinations, and for excessively noisy bolometers. After an exhaustive attempt to detect these sources it was determined that their signals were indistinguishable from random sky noise.

Given the likelihood that actual sub-mm flux was detected for our pairs, star formation rates were constructed. The construction of SFR's uses a relationship between the bolometric far-infrared luminosity (between 8–1000 μm) and SFR, and converts to units of $M_\odot \text{ yr}^{-1}$. These conversions have been calibrated in the literature both experimentally, and also using isochrone synthesis models; various conversions agree to within a factor of ~ 3 . The FIR luminosity of our sources was calculated by extrapolating a grey-body SED from our 850 μm fluxes. (A grey-body is a black-body modified with a frequency-dependent emissivity.) The dust temperature T_d and emissivity index β of our sources were taken from the SCUBA Local Universe Galaxy Survey (Dunne et al., 2000) simply because they represent the most complete and

systematic attempt to date to measure these quantities at the same observed wavelengths that we used. Although these values were the best available there is room for some skepticism given that our sources are all interacting pairs, for which dust temperature could be enhanced due to physical processes associated with collisions. Our star formation code was confirmed both by verifying SFR's from the literature and by predicting the SFR of Arp 220 at different FIR wavelengths.

Having calculated FIR star formation rates we revealed several methods for analysing the star formation behaviour of our sample. The first method used simple arguments to show that the ρ_{SFR} of pairs could constitute $\sim 60\%$ of the global ρ_{SFR} at moderate redshift. This calculation was shown to be somewhat misleading since it did not remove the bias of high optical/UV SFR's among our pairs. The second method for determining ρ_{SFR} was more detailed, but involved knowledge of quantities we cannot, for now, determine reliably, like the luminosity density in pairs. The third, and perhaps most reliable, way of measuring the star formation behaviour of pairs was to calculate the star formation rate per unit blue luminosity. This method avoids assumptions about the contribution of pairs to luminosity density. By weighting this average by the noise in the sub-mm flux measurements we can de-weight the bias of the optical/UV SFR's. The final result then mostly reflects the significance of detections in the sub-mm. This calculation showed that even when the optical/UV SFR's were de-weighted, the SFR/L_B of pairs still exceeded that of the CNOC2 field galaxy population by at least a factor of ~ 6 .

Note that the values for SFR/L_B do not reflect the total uncertainty inherent in this value. Errors in T , β , ρ_L , as well as optical flux error, have been omitted to show only the experimental error in sub-mm flux.

Since only one of our randomly-chosen pairs was detected with $> 3\sigma$ significance, it is possible that this detection was accidental and not indicative of a greater population of faint sub-mm galaxies at moderate redshift. A plausible explanation for accidental discovery is gravitational lensing of a high redshift galaxy by a source at moderate redshift. Based on a recent study (Chapman et al., 2002b) $\sim 3\%$ of SCUBA

sources brighter than 5 mJy are possible lensing candidates. There does exist, then, the possibility that one of our sources is a lensed galaxy. Nevertheless, we did observe 3 pairs with $> 2.5\sigma$ significance. It would therefore be very unlikely that more than than 1 out of 4 detections at $> 2.5\sigma$ could be lensed.

Given, then, that at least one of our 18 pairs was reliably detected ($> 3\sigma$, and three at $> 2.5\sigma$), it is possible to make inferences about the parent population. By relating the amount of star formation observed in the FIR to the optical/UV SFR we determined the probability that our pairs could be drawn from a parent population of CNOC2 galaxies. Optical/UV SFRs, available for ~ 5400 CNOC2 galaxies, were converted to $850 \mu\text{m}$ fluxes and then S/N ratios, given the same amount of median noise as for our observations. The likelihood of making the same rate of detections, at $850 \mu\text{m}$, was extremely small, as was the statistical probability that the CNOC2 population could be the parent population for our pairs. To confirm this another way we adjusted the factor by which FIR SFR exceeds that observed in the optical/UV. Only by increasing that factor to $\gtrsim 30$ could the same rate of detections be achieved. Since this amount of dust obscuration is much too large, given current estimates in the literature, this is the first good indication that our pairs constitute a separate class of star formers among their population. Further evidence for this was revealed by Monte Carlo tests which confirmed at the 99.8% level that the average SFR's obtained for pairs could not be obtained randomly.

Ideally we would have made further generalizations about the star formation behaviour in the Universe; however our sample of pairs appears to be insufficiently random so as to be representative of the optical/UV SFR's from the CNOC2 survey. In spite of this defect we can still claim with a reasonable degree of confidence that an excess of star formation does exist in pairs over field galaxies at moderate redshift. The evidence lies in the flux-error-weighted SFR per unit luminosity, which still shows at most a factor of ~ 15 excess over the SFR/L_B for the average CNOC2 field galaxy. Further work, with a totally random sample and more definitive optical/UV SFR's, is needed to determine the real excess in SFR and the extent to which that excess

originates with merger/interaction activity.

5.2 Future Work

There is reasonably good evidence suggesting the unique star formation behaviour of interacting pairs in the CNOC2 population. The cause of this uniqueness has not been ascertained, but the usual inducement effects of collisions cannot be ruled out. The difficulty in determining the cause of this behaviour is manifold. First a sufficiently large and random group of interacting pairs is required, followed by a similar group of isolated field galaxies—selected in the same waveband. These two sets of observations must then be compared with another two, equally consistent, sets of observations but at a different redshift. Finally, to determine ρ_{SFR} , both the absolute magnitudes, number fraction of pairs and luminosity densities of the two redshift groups must be known. These heavy demands make it very difficult to trace the cause of enhanced star formation in mergers in a consistent and accurate manner. This research has attempted to illustrate that collisional enhancement could account for the unique star forming behaviour of CNOC2 pairs with the best available data that exist. Until more observations are done in these areas only an upper limit on the fractional enhancement of ρ_{SFR} may be reported. The ultimate explanation must wait.

Several new instruments will come online in the future that will hopefully resolve these outstanding issues.

The Immediate Future: SIRTf The Space Infrared Telescope Facility, or SIRTf, is the last of NASA's "great observatory" space telescope projects. It is now scheduled to be launched in August 2003. SIRTf's infrared cameras will allow simultaneous imaging at wavelengths between $3.6 \mu\text{m}$ and $8 \mu\text{m}$ in an area of sky of 5.1×5.1 arcmin. Another multi-band photometer will allow imaging and spectroscopy at $24 \mu\text{m}$, $70 \mu\text{m}$ and $160 \mu\text{m}$. SIRTf's observations will expand

our knowledge of the nature of ULIRG's and starburst galaxies by mapping their structure and measuring the SED of dust.

The Near Future: SCUBA2 Work is currently under way to construct the next generation of SCUBA instruments for the JCMT. The SCUBA2 instrument, scheduled to come online by 2006, will supercede its progenitor in several important ways. First, it will have a field of view of 8×8 arcmin—16 times the area of SCUBA. Second, technological advancements will allow for an increase in the number of array pixels by 2 orders of magnitude. Whereas SCUBA has 37 and 91 pixels for the long and short wavelengths, respectively, SCUBA2 will consist of a total of 6400 pixels and will sample the sky in a manner similar to a CCD. Third, the array pixels will be closely packed, eliminating most of the deadspace that makes up 70% of the current array. SCUBA2 technology will also eliminate the need for sky-chopping, allowing for more accurate calibration and fewer image artefacts. Finally, SCUBA2 will have 2 times the sensitivity for observing point-source objects and allow for faster acquisition of signal. Note, however, that the angular resolution on the sky will remain the same ($\sim 13''$), since this is set by the telescope diameter. In addition to these major improvements, SCUBA2 will retain the ability to observe simultaneously at $450 \mu\text{m}$ and $850 \mu\text{m}$.

SCUBA2 will allow for larger areas of the sky to be mapped faster; this is an advance that will improve our knowledge of populations of galaxies that emit their bulk of their radiation in the FIR (i.e. ULIRG's). Using the improved mapping techniques, larger and more statistically valid samples of objects will be observed, thereby increasing our knowledge of such properties as dust mass, SFR, luminosity function and evolution, and perhaps even merger processes and evolution.

The Far Future: ALMA By the end of this decade (2009-2010) the Atacama Large Millimeter Array (ALMA) will come online. This will be an array of 64–12 m-diameter antennae situated at an elevation of 5000 m in the Chilean Andes.

(Canada is a partner in the project). Although intended for observations at radio wavelengths as well, ALMA receivers will detect in all atmospheric windows from 10 mm to 350 μm . Given the size of the array, the number of detector dishes (antennae), and the use of interferometry, ALMA will achieve resolution as small as 10 milli-arcseconds; it will also be able to map large areas of the sky. ALMA's very high resolution will allow future surveys to confirm the existence of interacting galaxies by resolving individual companions at sub-mm wavelengths, even at high redshift. The multiple detection bands will allow measurements of the cold "tail" of the dust SED and allow for a determination of the extent of cold dust components in galaxies. The wide bandwidths (matched to the width of the atmospheric windows) will allow spectroscopic measurements that should finally allow precise redshift measurements of sub-mm galaxies. This will significantly decrease, if not eliminate, the difficulties in matching galaxies from FIR and optical surveys, and reveal the extent to which sub-mm galaxies are lensed by optically-selected foreground galaxies. Although still 7 years from operation, ALMA will provide the most definitive and comprehensive observations at sub-mm wavelengths.

Bibliography

- Anantharamaiah, K. R., Viallefond, F., Mohan, N. R., Goss, W. M., and Zhao, J. H.: 2000, *Astrophys. J.* **537**, 613
- Archibald, E. N., Wagg, J. W., and Jenness, T.: 2000, *Calculating Sky Opacities: a re-analysis for SCUBA data*, Technical Report SCD System Note 2.2, James Clerk Maxwell Telescope
- Barton, E., Geller, M., and Kenyon, S. J.: 2000, *Astrophys. J.* **530**, 660
- Bell, E. F.: 2002, *Astrophys. J.* **577**, 150
- Benford, D. J.: 1999, *Ph.D. thesis*, California Institute of Technology, Advisor: Phillips, T.G.
- Blain, A. W. and Phillips, T. G.: 2002, *Mon. Not. Royal. Astron. Soc.* **333**, 222
- Blain, A. W., Smail, I., Ivison, R. J., Kneib, J. P., and Frayer, D. T.: 2002, *Physics Reports*, **369**, 111
- Blain, A. W., Smail, I. and Ivison, R. J., and Kneib, J. P.: 1999, *Mon. Not. Royal. Astron. Soc.* **302**, 632
- Bothun, G. D., Lonsdale, C. J., and Rice, W.: 1989, *Astrophys. J.* **341**, 129
- Bruzual, G. and Charlot, S.: 1993, *Astrophys. J.* **405**, 538
- Bushouse, H. A.: 1987, *Astrophys. J.* **320**, 29
- Calzetti, D., Armus, L., Bohlin, R. C., Kinney, A. L., Koornneef, J., and Storchi-Bergmann, T.: 2000, *Astrophys. J.* **533**, 682
- Cardelli, J. A., Clayton, G. C., and Mathis, J. S.: 1989, *Astrophys. J.* **345**, 245
- Cardiel, N., Elbaz, D., Schiavon, R. P., Willmer, C. N. A., Koo, D. C., Phillips, A. C., and Gallego, J.: 2003, *Astrophys. J.* **584**, 76

- Carilli, C. L. and Yun, M. S.: 1999, *Astrophys. J. Letters*, **513**, L13
- Chapman, S. C., Lewis, G. F., Scott, D., Borys, C., and Richards, E.: 2002a, *Astrophys. J.* **570**, 557
- Chapman, S. C., Scott, D., Steidel, C. C., Borys, C., Halpern, M., Morris, S. L., Adelberger, K. L., Dickinson, M., Giavalisco, M., and Pettini, M.: 2000, *Mon. Not. Royal. Astron. Soc.* **319**, 318
- Chapman, S. C., Smail, I., Ivison, R. J., and Blain, A. W.: 2002b, *Mon. Not. Royal. Astron. Soc.* **335**, L17
- Charlot, S., Kauffman, G., Longhetti, M., Tresse, L., White, S. D. M., and Maddox, S. J.: 2002, *Mon. Not. Royal. Astron. Soc.* **330**, 876
- Chini, R., Krügel, E., Kreysa, E., and Gemünd, H. P.: 1989, *Astron. & Astrophys.* **216**, L5
- Clements, D. L.: 1999, *Astrophysics and Space Science* **266**, 233
- Condon, J. J.: 1992, *Ann. Rev. Astron. & Astrophys.* **30**, 575
- Cowie, L. L., Hu, E. M., Songaila, A., and Egami, E.: 1997, *Astrophys. J. Letters*, **481**, L9
- Cowie, L. L., Songaila, A., and Barger, A. J.: 1999, *Astron. J.* **118**, 603
- Crampton, D. Le Fèvre, O., Lilly, S. J., and Hammer, F.: 1995, *Astrophys. J.* **455**, 96
- da Costa, L. N., Willmer, C. N. A., Pellegrini, P. S., Chaves, O. L., Rit e, C., Maia, M. A. G., Geller, M. J., Latham, D. W., Kurtz, M. J., Huchra, J. P., Ramella, M., Fairall, A. P., Smith, C., and L ipari, S.: 1998, *Astron. J.* **116**, 1
- Dey, A., Graham, J. R., Ivison, R. J., Smail, I., Wright, G. S., and Liu, M. C.: 1999, *Astrophys. J.* **519**, 610
- Downes, D., Neri, R., Greve, A., Guilloteau, S., Casoli, F., Hughes, D., Lutz, D., Menten, K. M., Wilner, D. J., Andreani, P., Bertoldi, F., Carilli, C. L., Dunlop, J., Genzel, R., Gueth, F., Ivison, R. J., Mann, R. G., Mellier, Y., Oliver, S., Peacock, J., Rigopoulou, D., Rowan-Robinson, M., Schilke, P., Serjeant, S., Tacconi, L. J., and Wright, M.: 1999, *Astron. & Astrophys.* **347**, 809
- Downes, D. and Solomon, P. M.: 1998, *Astrophys. J.* **507**, 615

- Draine, B. T. and Lee, H. M.: 1984, *Astrophys. J.* **285**, 89
- Dunne, L.: 2003, Private Communication
- Dunne, L. and Eales, S.: 2001, *Mon. Not. Royal. Astron. Soc.* **327**, 697
- Dunne, L. and Eales, S.: 2002, *Astrophysics and Space Science* **281**, 321
- Dunne, L., Eales, S., Edmunds, M., Ivison, R., Alexander, P., and Clements, D. L.: 2000, *Mon. Not. Royal. Astron. Soc.* **315**, 115
- Eales, S., Lilly, S., Gear, W., Dunne, L., Bond, J. R., Hammer, F., Le Fèvre, O., and Crampton, D.: 1999, *Astrophys. J.* **515**, 518
- Economou, F. and Jenness, T.: 1998, ORAC-DR is copyright © 1998-2001 PPARC (the UK Particle Physics and Astronomy Research Council.)
- Elbaz, D., Césarsky, C. J., Chaniel, P., Aussel, H., Franceschini, A., Fadda, D., and Chary, R. R.: 2002, *Astron. & Astrophys.* **384**, 848
- Flores, H., Hammer, F., Thuan, T. X., Césarky, C., Desert, F. X., Omont, A., Lilly, S. J., Eales, S., Crampton, D., and Le Fèvre, O.: 1999, *Astrophys. J.* **517**, 148
- Frayer, D. T., Ivison, R. J., Scoville, N. Z., Evans, A. S., Yun, M. S., Smail, I., Barger, A. J., Blain, A. W., and Kneib, J. P.: 1999, *Astrophys. J. Letters*, **524**, L13
- Frayer, D. T., Scoville, N. Z., Yun, M., Evans, A. S., Smail, I., Blain, A. W., and Kneib, J. P.: 1998, *Astrophys. J. Letters*, **506**, L7
- Frayer, D. T., Smail, I., Ivison, R. J., and Scoville, N. Z.: 2000, *Astron. J.* **120**, 1668
- Glazebrook, K., Blake, C., Economou, F., Lilly, S., and Colless, M.: 1999, *Mon. Not. Royal. Astron. Soc.* **306**, 843
- Graham, D. P., Carico, K. M., Neugebauer, G., Soifer, B. T., and Wilson, T. D.: 1990, *Astrophys. J.* **354**, 5
- Hildebrand, R. H.: 1983, *Royal Astron. Soc. Quart. Journal*, **24**, 267
- Hopkins, A. M., Connolly, A. J., Haarsma, D. B., and Cram, L. E.: 2001, *Astrophys. J.* **122**, 288
- Hughes, D. H., Robson, E. I., Dunlop, J. S., and Gear, W. K.: 1993, *Mon. Not. Royal. Astron. Soc.* **263**, 607
- Inoue, A. K.: 2002, *Astrophys. J.* **570**, 97
- Jenness, T. and Lightfoot, J. F.: 2000, *SURF: SCUBA User Reduction Facility*,

- User's Manual*, Starlink Project, CLRC, Starlink User Note 216
- Keel, W. C.: 1993, *Astron. J.* **106**, 1771
- Keel, W. C. and van Soest, E. T. M.: 1992, *Astron. & Astrophys. Supp.* **94**, 553
- Kennicutt, R.: 1998a, *Astrophys. J.* **498**, 541
- Kennicutt, R. C.: 1998b, *Ann. Rev. Astron. & Astrophys.* **36**, 189
- Kennicutt, R. C., Keel, W. C., van der Hulst, J. M., Hummel, E., and Roettiger, K. A.: 1987, *Astron. J.* **93**, 5
- Kennicutt, R. C., Schweizer, F., and Barnes, J. E.: 1998, *Galaxies: Interactions and Induced Star Formation*, Saas-Fee Advanced Course 26, Springer-Verlag, Berlin Heidelberg, Swiss Society for Astrophysics and Astronomy: Lecture Notes 1996
- Kennicutt, R. C., Tamblyn, P., and Congdon, C. E.: 1994, *Astrophys. J.* **435**, 22
- Kewley, L. J., Geller, M. J., Jansen, R. A., and Dopita, M. A.: 2002, *Astron. J.* **124**, 3135
- Larson, R. B.: 2002, in J. M. De Buizer and N. S. van der Blik (eds.), *Astron. Soc. Pacific, Conf. Series*, Vol. 287, p. 65, Astron. Soc. Pacific
- Larson, R. B. and Tinsley, B. M.: 1978, *Astrophys. J.* **219**, 46
- Leitherer, C. and Heckman, T. M.: 1995, *Astrophys. J. Supp.* **96**, 9
- Lilly, S. J., Le Fèvre, O., Crampton, D., Hammer, F., and Tresse, L.: 1995, *Astrophys. J.* **455**, 50
- Lilly, S. J., Le Fèvre, O., Hammer, F., and Crampton, D.: 1996, *Astrophys. J. Letters*, **460**, L1
- Lin, H. and CNOC2 Collaboration: 2001, in *American Astronomical Society Meeting*, Vol. 198
- Lin, H., Yee, H. K. C., Carlberg, R. G., Morris, S. L., Sawicki, M., Wirth, G. D., and Shepherd, C. W.: 1999, *Astrophys. J.* **518**, 533
- Madau, P., Ferguson, H. C., Dickinson, M. E., Giavalisco, M., Steidel, C. C., and Fruchter, A.: 1996, *Mon. Not. Royal. Astron. Soc.* **183**, 1388
- Madau, P., Pozzetti, L., and Dickinson, M.: 1998, *Astrophys. J.* **498**, 106
- Mathis, J. S.: 1990, *Ann. Rev. Astron. & Astrophys.* **28**, 37
- Mattig, W.: 1958, *Astronomische Nachrichten* **284**, 109

- Morris, S. L.: 2003, In preparation
- Nikola, T., Genzel, R., Herrmann, F., Madden, S. C., Poglitsch, A., Geis, N., Townes, C. H., and Stacey, G. J.: 1998, *Astrophys. J.* **504**, 749
- Oliveira, F. J. and Coulson, I. M.: 2002, *Estimated Variance for SCUBA Skydip Measurements*, Technical Report SCD System Note 6.0, James Clerk Maxwell Telescope
- Patton, D. R.: 2003, In preparation
- Patton, D. R., Carlberg, R. G., Marzke, R. O., Pritchett, C. J., da Costa, L. N., and Pellegrini, P. S.: 2000, *Astrophys. J.* **536**, 153
- Patton, D. R., Pritchett, C. J., Carlberg, R. G., Marzke, R. O., Yee, H. K. C., Hall, P. B., Lin, H., Morris, S. L., Sawicki, M., Shepherd, C. W., and Wirth, G. D.: 2002, *Astrophys. J.* **565**, 208
- Patton, D. R., Pritchett, C. J., Yee, H. K. C., Ellingson, E., and Carlberg, R. G.: 1997, *Astrophys. J.* **475**, 29
- Peacock, J. A.: 1999, *Cosmological Physics*, p. 449, Cambridge University Press
- Pritchett, C. J.: 1994, *Pub. Astron. Soc. Pacific*, **106**, 1052
- Rand, R. J.: 1994, *Astron. & Astrophys.* **285**, 833
- Regan, M. W., Thornley, M. D., Helfer, T. T., Sheth, K., Wong, T., Vogel, S. N., Blitz, L., and Bock, D. C. J.: 2001, *Astrophys. J.* **561**, 218
- Rigopolou, D., Lawrence, A., and Rowan-Robinson, M.: 1996, *Mon. Not. Royal. Astron. Soc.* **278**, 1049
- Salpeter, E. E.: 1955, *Astrophys. J.* **121**, 161
- Sanders, D. B., Soifer, B. T., Elias, J. H., Madore, B. F., Matthews, K., Neugebauer, G., and Scoville, N. Z.: 1988, *Astrophys. J.* **325**, 74
- Schmidt, M.: 1959, *Astrophys. J.* **129**, 243
- Scott, S. E., Fox, M. J., Dunlop, J. S., Serjeant, S., Peacock, J. A., Ivison, R. J., Oliver, S., Mann, R. G., Lawrence, A., Efstathiou, A., Rowan-Robinson, M., Hughes, D. H., Archibald, E. N., Blain, A., and Longair, M.: 2002, *Mon. Not. Royal. Astron. Soc.* **331**, 817
- Scoville, N. Z. and Young, J. S.: 1983, *Astrophys. J.* **265**, 148

- Shioya, Y., Taniguchi, Y., and Trentham, N.: 2001, *Mon. Not. Royal. Astron. Soc.* **321**, 11
- Smail, I., Ivison, R. J., Owen, F. N., Blain, A. W., and Kneib, J. P.: 2000, *Astrophys. J.* **528**, 612
- Smail, I. and Ivison, R. J., Kneib, J. P., Cowie, L. L., Blain, A. W., Barger, A. J., Owen, F. N., and Morrison, G.: 1999, *Mon. Not. Royal. Astron. Soc.* **308**, 1061
- Sodroski, T. J., Bennett, C., Boggess, N., Dwek, E., Franz, B. A., Hauser, M. G., Kelsali, T., Moseley, S. H., Odegard, N., Silverberg, R. F., and Weiland, J. L.: 1994, *Astrophys. J.* **428**, 638
- Soifer, B. T., Boehmer, L., Neugebauer, G., and Sanders, D. B.: 1989, *Astron. J.* **98**, 766
- Soifer, B. T., Houck, J. R., and Neugebauer, G.: 1987, *Ann. Rev. Astron. & Astrophys.* **25**, 187
- Soifer, B. T., Rowan-Robinson, M., Houck, J. R., de Jong, T., Neugebauer, G., Aumann, H. H., Beichman, C. A., Boggess, N., Clegg, P. E., Emerson, J. P., Gillett, F. C., Habing, H. J., Hauser, M. G., Low, F. J., Miley, G., and Young, E.: 1984, *Astrophys. J. Letters*, **278**, L71
- Songaila, A., Cowie, L. L., and Lilly, S. J.: 1990, *Astrophys. J.* **348**, 371
- Steidel, C. C., Adelberger, K. L., Giavalisco, M., and Pettini, M.: 1999, *Astrophys. J.* **519**, 1
- Thronson, H. and Telesco, C.: 1986, *Astrophys. J. Letters*, **309**, L79
- Treyer, M. A., Ellis, R. S., Milliard, B., Donas, J., and Bridges, T. J.: 1998, *Mon. Not. Royal. Astron. Soc.* **300**, 303
- Walterbos, R. A. M. and Greenawalt, B.: 1996, *Astrophys. J.* **460**, 696
- Wilson, C. D., Scoville, N., Madden, S. C., and Charmandaris, V.: 2000, *Astrophys. J.* **542**, 120
- Wilson, G., Cowie, L. L., Barger, A. J., and Burke, D. J.: 2002, *Astron. J.* **124**, 1258
- Yee, H. K. C., Ellingson, E., and Carlberg, R. G.: 1996, *Astrophys. J. Supp.* **102**, 269
- Yee, H. K. C., Morris, S. L., Lin, H., Carlberg, R. G., Hall, P. B., Sawicki, M., Patton,

-
- D. R., Wirth, G. D., Ellingson, E., and Shepherd, C. W.: 2000, *Astrophys. J. Supp.* **129**, 475
- Yun, M. S., Ho, P. T. P., and Lo, K. Y.: 1993, *Astrophys. J. Letters*, **411**, L17

Appendix A

Parametrization of Dust Extinction in Optical, UV and Infrared

The following functional parametrization of the dust extinction law is excerpted from Cardelli, et al. (1989). It describes the functions $a(x)$ and $b(x)$ from bands in the near-infrared to the ultraviolet using a parameter x , where $x = 1/\lambda$ [μm].

A.1 The Infrared

$$0.3\mu\text{m}^{-1} \leq x \leq 1.1\mu\text{m}^{-1} :$$

$$\begin{aligned} a(x) &= 0.574x^{1.61} \\ b(x) &= -0.527x^{1.61} \end{aligned} \tag{A.1}$$

A.2 Optical/NIR

$$1.1\mu\text{m}^{-1} \leq x \leq 3.3\mu\text{m}^{-1} \text{ and } y = (x - 1.82):$$

$$a(x) = 1 + 0.17699y - 0.50477y^2 - 0.02427y^3 + 0.72085y^4 + 0.01979y^5 - 0.77530y^6 + 0.32999y^7 \quad (\text{A.2})$$

$$b(x) = 1.41338y + 2.28305y^2 + 1.09233y^3 - 5.38434y^4 - 0.62251y^5 + 5.30260y^6 - 2.09002y^7$$

A.3 UV and Far UV

$$\begin{aligned} a(x) &= 1.752 - 0.316x - 0.104/[(x - 4.67)^2 + 0.341] + F_a(x) \\ b(x) &= -3.090 + 1.825x + 1.206/[(x - 4.62)^2 + 0.263] + F_b(x) \end{aligned} \quad (\text{A.3})$$

where,

$$\begin{aligned} F_a &= -0.04473(x - 5.9)^2 - 0.009779(x - 5.9)^3 \\ F_b &= 0.2130(x - 5.9)^2 + 0.1207(x - 5.9)^3 \end{aligned} \quad (\text{A.4})$$

for $8\mu\text{m}^{-1} \leq x \leq 5.9\mu\text{m}^{-1}$ and $F_a = F_b = 0$ for $x < 5.9\mu\text{m}^{-1}$.

VITA

Surname: Klopp

Given Name: Aaron

Place of Birth: Toronto, Ontario, Canada

Educational Institutions Attended:

Queen's University	1997 – 2001
University of Victoria	2001 – 2003

Degrees Awarded:

B.Sc.(Honours), Queen's University	2001
------------------------------------	------

Honours and Awards:

University of Victoria Fellowship	2001-2003
Dean's Honour List, Queen's University	2001

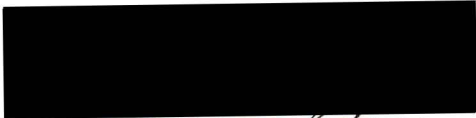
University of Victoria Partial Copyright License

I hereby grant the right to lend my thesis to users of the University of Victoria Library, and to make single copies only for such users or in response to a request from the Library of any other university, or similar institution, on its behalf or for one of its users. I further agree that permission for extensive copying of this thesis for scholarly purposes may be granted by me or a member of the University designated by me. It is understood that copying or publication of this thesis for financial gain shall not be allowed without my written permission.

Title of Thesis:

Submillimeter Star Formation Rates in Interacting Pairs

Author:


Aaron Klopp
June 16, 2003